OPTIMUM DESIGN OF A SANDWICH PLATE WITH EGG-CRATE SHAPED CORE FOR MAXIMUM STRENGTH UNDER THREE-POINT BENDING

by
Coşkun Yalkılıç
B.S., Mechatronics, Sabanci University, 2013

Submitted to the Institute for Graduate Studies in
Science and Engineering in partial fulfillment of
the requirements for the degree of
Master of Science

Graduate Program in Mechanical Engineering
Boğaziçi University
2019

ACKNOWLEDGEMENTS

I would first like to thank my thesis advisor Prof. Fazıl Önder Sönmez for their guidance and invaluable contribution throughout my thesis study. Their guidance helped me in all the time of research and writing of this thesis.

I would like to thank to the research assistant Fatih Öz for his great support throughout the study. Without his passionate participation, the experimental part of this study could not have been successfully conducted. I should also thank to the composites laboratory technician Hakan Moldur for his endless help during the manufacturing part of this study.

Finally, I must express my deepest gratitude to my parents for providing me with endless support and everlasting encouragement throughout my years of study and through the process of researching and writing this thesis. This accomplishment would not have been achieved without them. Thank you.

ABSTRACT

OPTIMUM DESIGN OF A SANDWICH PLATE WITH EGG-CRATE SHAPED CORE FOR MAXIMUM STRENGTH UNDER THREE-POINT BENDING

This thesis study aims to maximize the bending strength of a sandwich composite plate with an egg-crate shaped core under three-point bending loading. The material is chosen as epoxy-reinforced with non-crimp E-glass fabric and the layup configuration is quasi-isotropic for both core and face sheets. The mechanical response of the composite material is determined by conducting tension tests on specimens with quasi-isotropic $[0/45/-45/90]_s$, cross-ply $[0/90]_{2s}$, and angle-ply symmetric $[45/-45]_s$ layup sequences. Acoustic emission (AE) monitoring is used to detect the damage events, identify the damage mechanisms, and ascertain the load levels at which different laminae fail. By making use of a progressive failure model and the tension test data, the mechanical properties of a ply are determined.

A finite element model is developed in ABAQUS environment to simulate the behavior of the composite sandwich plate under three-point bending. The first-ply failure load level is determined based on Tsai-Hill failure criterion using the secant algorithm. The model is validated by comparing its predictions with the results obtained by three-point bending tests. A two-variable shape optimization study is performed using Nelder-Mead method for the core structure to maximize the overall bending strength of the composite sandwich plate. The optimum core structure is manufactured by using a 3D-printed polylactic acid (PLA) mold. The face sheets and the core structure are manufactured using vacuum infusion process (VIP). The comparison between the test results and the finite element model shows that the finite element model sufficiently predicts the first-ply failure load level and the failure region.

ÖZET

ÜÇ NOKTALI BÜKME YÜKÜ ALTINDA AZAMİ MUKAVEMET İÇİN YUMURTA KAFESİ ŞEKLİNDE ÇEKİRDEK YAPISINA SAHİP BİR SANDVİÇ PLAKANIN EN İYİ TASARIMI

Bu tez çalışmasının amacı, yumurta kafesi şeklinde çekirdek yapısına sahip bir kompozit sandviç plakanın üç noktalı bükme yükü altında bükülme mukavemetinin azami hadde çıkarılmasıdır. Çekirdek ve yüz plakaları için malzeme olarak epoksiyle desteklenmiş kırpılmamış cam elyaf kumaş, dizilim olarak yarı-izotropik dizilim seçilmiştir. Kompozit malzemenin mekanik özelliklerinin belirlenmesi için yarı izotropik $[0/45/-45/90]_s$, çapraz kat $[0/90]_{2s}$ ve açılı kat simetrik $[45/-45]_s$ dizilimli numunelerle çekme testleri gerçekleştirilmiştir. Farklı kompozit malzeme katmanlarındaki hasarlanmaların saptanması, tanımlanması ve kırılma yük seviyelerinin belirlenmesi için akustik emisyon izleme yöntemi kullanılmıştır. İlerleyen hasarlanma modeli ve çekme test sonuçları kullanılarak bir katmanın mekanik özellikleri belirlenmiştir.

Kompozit sandviç plakanın üç noktalı bükme altındaki davranışının benzetimini yapma amacıyla ABAQUS ortamında bir sonlu elemanlar modeli kurulmuştur. İlk katman kırılma yük seviyesi Tsai-Hill kriterine dayanan sekant algoritmasıyla belirlenmiştir. Model, algoritma öngörüleriyle üç noktalı bükme test sonuçları karşılaştırılarak doğrulanmıştır. Kompozit sandviç plakanın bükülme mukavemetini azami hadde çıkarmak amacıyla çekirdek yapısına Nelder-Mead metodu kullanılarak iki değişkenli şekil eniyilemesi uygulanmıştır. En iyi çekirdek yapısı, üç boyutlu yazıcıyla üretilen polilaktik asit (PLA) kalıp kullanılarak imal edilmiştir. Yüz plakaları ve çekirdek yapısı vakum infüzyon tekniğiyle üretilmiştir. Test sonuçları ve sonlu elemanlar modeli arasındaki karşılaştırma sonlu elemanlar modelinin ilk kırılma yük seviyesini ve kırılma bölgesini yeterli doğrulukta tespit ettiğini göstermiştir.

TABLE OF CONTENTS

LIST OF FIGURES

LIST OF TABLES

LIST OF SYMBOLS

S	Shear strength
S_ε	Ultimate shear strain
X	Strength in first principal direction
X_t	Tensile strength in fiber direction
X_c	Compressive strength in fiber direction
X_{ε_t}	Ultimate tensile strain in fiber direction
X_{ε_c}	Ultimate compressive strain in fiber direction
Y	Strength in second principal direction
Y_t	Tensile strength in transverse direction
Y_c	Compressive strength in transverse direction
Y_{ε_t}	Ultimate tensile strain in transverse direction
Y_{ε_c}	Ultimate compressive strain in transverse direction
Z	Strength in third principal direction
σ_i	Stress component in direction i
ε_i	Strain component in direction i
τ_{ij}	Shear stress component in plane ij
γ_{ij}	Shear strain component in plane ij

LIST OF ACRONYMS/ABBREVIATIONS

2D	Two Dimensional
3D	Three Dimensional
AE	Acoustic Emission
ASTM	American Society for Testing and Materials
CFRP	Carbon Fiber Reinforced Polymer
dB	Decibel
FE	Finite Element
GFRP	Glass Fiber Reinforced Polymer
kHz	Kilo Hertz
kN	Kilo Newton
MPa	Mega Pascal
N	Newton
NLGEOM	Non-linear Geometry
PLA	Polylactic Acid
VIP	Vacuum Infusion Process

1. INTRODUCTION

Composite materials are composed of at least two materials combined to give the resultant product superior characteristics than those of the individual constituents. The final material properties are significantly affected by the properties of the individual constituent materials. Composite materials used in advanced structural applications are developed by reinforcing a matrix material with continuous high-strength fibers. Not only the type of the constituent materials but also their volumetric fractions affect the resulting material properties [1]. A properly tailored combination generally gives a composite material low weight, high strength, and high stiffness-to-weight ratio. Other design requirements such as impact resistance, high corrosion resistance, and effective noise and vibration properties may be satisfied by composite materials depending on the requirements of a particular application [2].

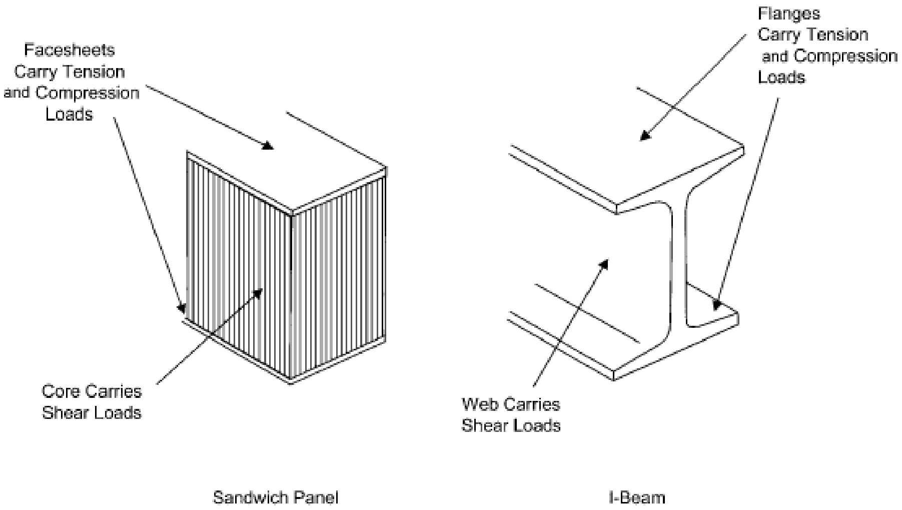

Figure 1.1. Analogy between sandwich panel and I-beam [3].

Composite sandwich structures are widely used in commercial and aerospace industries thanks to their lightweight construction, high flexural stiffness and strength-to-weight ratio. The sandwich structures consist of two thin and strong face sheets separated by a relatively thick lightweight core. The basic idea in a sandwich structural design is that the faces bear the bending loads, while the core supports the shear loads, analogous to an I-beam (Figure 1.1). The main purpose in using the core is merely to increase the second moment of area by providing separation between the faces. The core does not contribute significantly to the bending strength and stiffness of the structure; however, it is expected to have sufficiently high shear and compressive strength to resist shear and crushing loads [4]. Commonly used face materials are glass, carbon, or aramid-reinforced composites and metal. Core materials range from open and closed cell foams, balsa wood to metallic and nonmetallic honeycomb cores. Although the cost of honeycomb cores is generally higher than foam cores, they provide better performance. Foam cores are preferred in commercial applications for their low cost and easy workability, while honeycombs are used in aerospace applications for their good mechanical properties [3].

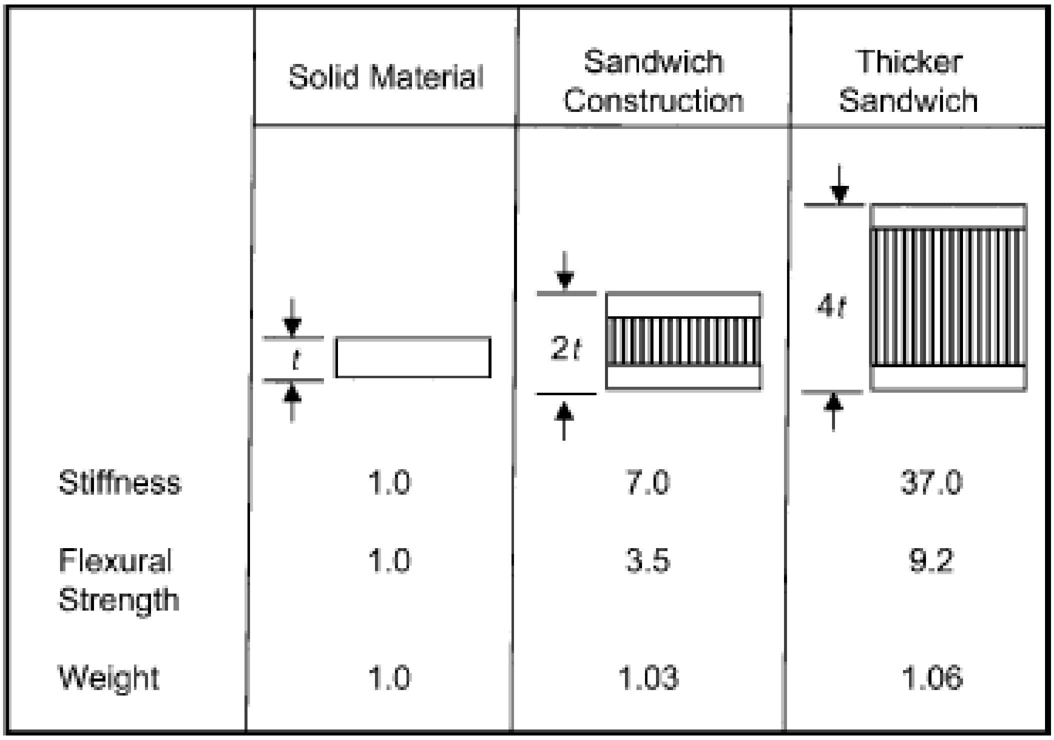

	Solid Material	Sandwich Construction	Thicker Sandwich
Stiffness	1.0	7.0	37.0
Flexural Strength	1.0	3.5	9.2
Weight	1.0	1.03	1.06

Figure 1.2. Efficiency of sandwich structures [3].

Sandwich structures have high structural efficiency in terms of flexural stiffness or strength-to-weight ratio (Figure 1.2). The moment of inertia exponentially increases as the distance between the faces is increased. The stiffness of the overall structure can be improved as far as thirty-seven times by increasing the core thickness to three times the total face thickness with only a six percent weight increase [3]. These superior mechanical characteristics make sandwich structures an efficient design solution for engineering applications in areas including aerospace, maritime, rail transportation, and automotive [5].

1.1. Composite Sandwich Core Materials

Composite sandwich plates have a thick, light-weight core structure between two stiff and strong face sheets made of composite materials. The overall mechanical response of a composite sandwich plate depends on the materials used, thickness, stacking sequence of the faces, and core topology design. Since the faces are simply flat panels regardless of the material used, composite sandwich structures can be classified based on the core material. The most widely used materials are foam, cellular core structures like honeycomb, and truss cores [6].

Foams are one of the most widely used core materials. Most commercial foams are generally made from polymers. Polyurethane, polyvinylchloride (PVC), and polymethacrylimide (PMI) are the most commonly used foam polymers [7]. Despite their low cost, foam cores have low stiffness and strength properties compared to honeycombs. Delamination and buckling are commonly observed failure mechanisms due to local stiffness nonconformity and lack of reinforcements bonding the faces and the core [8].

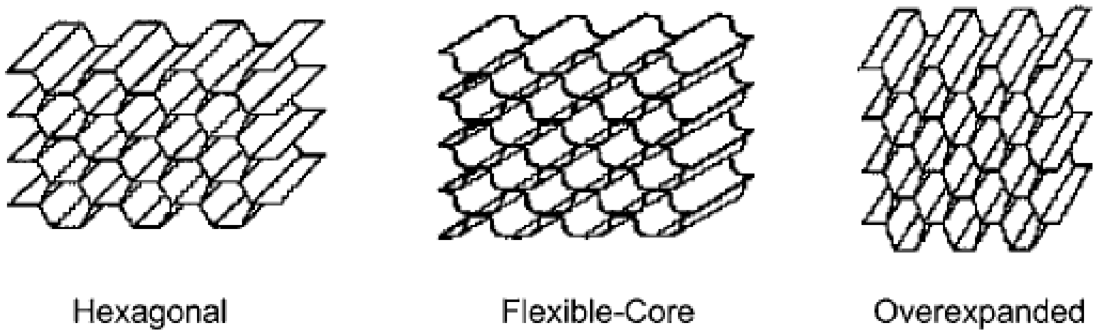

Figure 1.3. Types of honeycomb core cell structures [3].

Honeycomb core is an array of prismatic cells that nest together and form a planar structure, like a bee’s honeycomb. Hexagonal, flexible-core and over-expanded forms are the most common cell configurations (Figure 1.3). The honeycomb core terminology is shown in Figure 1.4. The direction “L” is the ribbon direction and it is stronger than the width (node bond) or “W” direction. The thickness is denoted by “t”, and the cell size is the dimension between the cell walls.

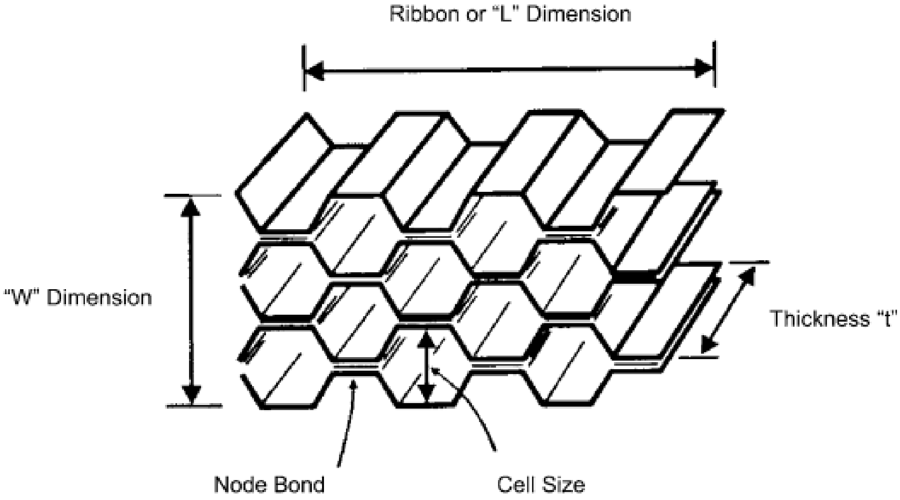

Figure 1.4. Honeycomb core terminology [9].

The main drawback of hexagonal configuration is its low formability. Anti-clastic curvature effects are observed due to very high values of Poisson’s ratio. When a composite sandwich structure with a hexagonal honeycomb core is subjected to bending, it forms opposite curvature in the perpendicular direction like a saddle shape (Figure 1.5). The formability of flexible core is the highest thanks to their compound contours preventing buckling at the cell walls. Although over-expanded core offers better formability than hexagonal core, it is not as good as flexible core. Over-expanded configuration increases the shear properties in the “W” direction but decreases the shear properties in the “L” direction. Honeycomb core provides superior strength and stiffness properties compared to other core materials however, it is expensive and difficult to fabricate into complex assemblies [3].

Although honeycomb core structures are more desirable in complex applications compared to truss core structures, truss cores have additional potential for multi-functional applications thanks to their open-cell structure. For example, sandwich structures with solid faces and truss cores can function as insulation elements while carrying loads at the same time. The space between the faces can be used for storage of a fluid or pressurized gas in other applications. However, honeycomb-core sandwich structures do not provide simultaneous functioning for multiple purposes [11, 12]. The open cell topology helps the designers to achieve the intended stiffness and strength properties by adjusting the topology (Figure 1.6). Additionally, while the truss cores may be preferred for the hollow space provided between the faces for noise and thermal insulation purposes in some applications [13], they may also be preferred as impact energy absorbers for automotive, naval and aircraft applications [14].

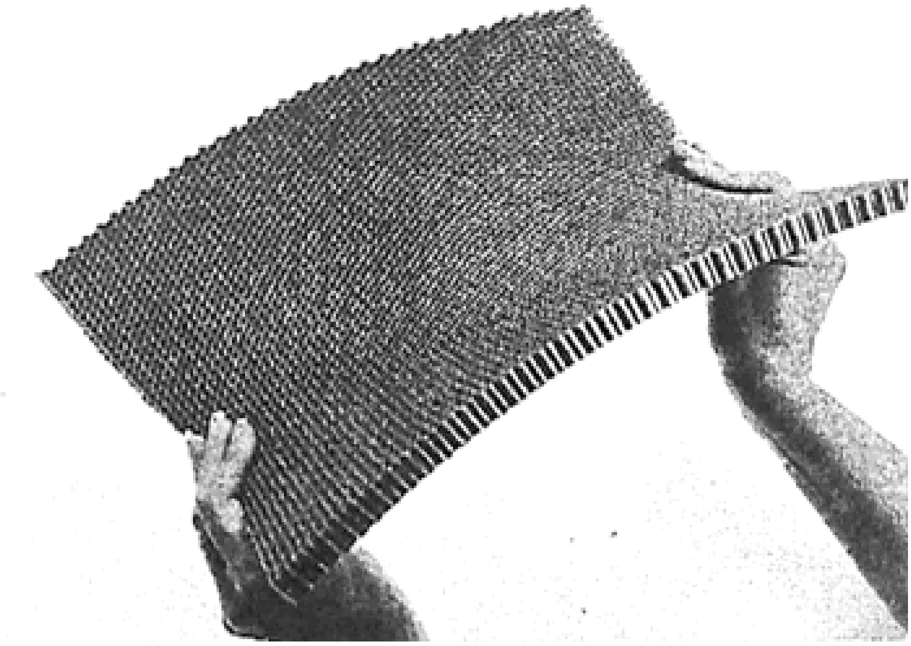

Figure 1.5. Anti-clastic curvature of a honeycomb [10].

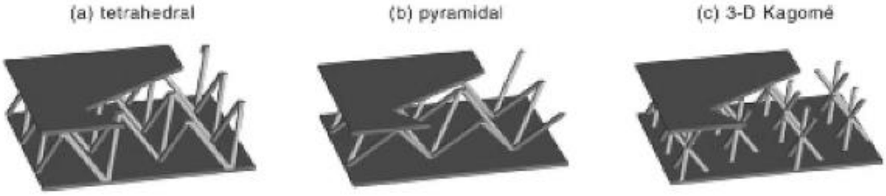

Figure 1.6. Examples of truss core structure [13].

The selection of the core material depends on the cost, mechanical performance, and requirements of the design. In general, the core material must be capable of transferring the shear load between faces and resist local crushing. In addition to mechanical requirements, other requirements such as high thermal insulation and corrosion resistance may play an important role for selecting the core material depending on the application.

1.2. Literature Review

Composite sandwich structures have attracted the attention of researchers in various fields such as civil transportation, marine, aerospace and civil engineering applications. In the previous studies, the composite sandwich structures have been optimized to achieve various design goals such as minimum weight and minimum cost while still meeting certain design constraints including maximum allowable deflection, allowable stiffness and strength requirements. In the literature, both experimental and computational studies have been conducted to observe the behavior of the composite sandwich structures and obtain the desired mechanical properties. Computationally found optimum designs were manufactured and tested to verify proposed methodologies. In this section, previous studies related to the optimization of sandwich structures and studies on sandwich structures with egg-box core will be briefly discussed.

1.2.1. Literature on Optimization of Sandwich Plates

Liu *et al*. [15] optimized a steel truss-core sandwich plate for minimum weight under various types of loading including shear, bending and compression. A two dimensional single-layer sandwich model was developed. This model was combined with a homogenization method replacing 3D truss cores with 2D effective solid cores. The number of truss elements in a unit cell, the width of the unit cell and the thickness of the sandwich plate were selected as the design variables. The optimization problem was solved using a sequential programming algorithm. The constraints were imposed on yielding and buckling for the core and the face sheets. The results of the optimization study demonstrated that 4-rod unit cell with solid truss members and pyramidal unit cell with hollow truss members were in good agreement with the best cell topologies.

Qiao *et al*. [16] used multi-objective optimization and homogenization technique to maximize the effective transverse shear stiffness of composite honeycomb cores. The design variables were selected as the thickness and width of the flat and angled walls of the honeycomb. The effective shear stiffness of the honeycomb cores was predicted using a two-scale homogenization technique. Equal weighting factors were assigned to each transverse shear stiffness component to optimize the overall shear stiffness of the honeycomb cores with sinusoidal, hexagonal and tubular shapes. The optimization problem was solved using a sequential quadratic programming algorithm. The proposed methodology for the optimization was found useful to maximize transverse shear properties of composite honeycomb structures.

Sun *et al.* [17] proposed a two-stage variable fidelity method to obtain optimum crashworthiness design for aluminum cellular honeycomb structures. In the first stage, a correction response surface (RS) was developed from the ratio or difference between high-fidelity and low-fidelity analyses at a number of sample points. In the second stage, a radial basis function (RBF) was used to approximate the high-fidelity response, combined with the RS model from the first stage. The design variables were selected as the yield strength of the material and the wall thickness of the honeycomb. The honeycomb structure was optimized to maximize specific energy absorption using the particle swarm optimization (PSO) algorithm. The study reported that the multi-fidelity optimization better improved the crashworthiness of the honeycomb structure than the single-fidelity method without bringing additional computational cost.

Poirier *et al.* [18] performed multi-objective optimization for steel sandwich structures with prismatic V-cores subjected to quasi-static loading. Nonlinear finite element analyses were conducted for the sandwich panels. In order to verify the model, the results of the model were compared with a reference sandwich panel with known deflection and stress values. Various parameters such as thicknesses of the face sheets, number of prismatic cores, core plate elements and weld locations were considered as optimization parameters. The peak Von-Mises stress was imposed as the design constraint to prevent the resulting sandwich panels from plastic yielding. The optimization problem was solved using a non-dominated sorting genetic algorithm. The methodology was presented with two case studies. In the first study, minimum deflection was intended for a rectangular steel sandwich panel in which the face sheets were bonded to the core section with double welds, whereas the second study was performed for a square steel sandwich panel in which face sheets were bonded to the core section with a single weld. The study revealed that the proposed methodology was successful to obtain laser-welded steel sandwich panels with high mechanical performance as well as minimum weight.

Xie *et al*. [19] proposed an optimization procedure for the design of an integrated thermal protection system (ITPS) with minimum weight. The two-stage optimization process was performed on a corrugated sandwich panel under simultaneous thermal and mechanical loads. Geometric dimensions of the unit cell were selected as the design variables. In the first stage, the temperature distribution was obtained. Then, the optimal height of the core was determined based on thermal performance. In the second stage, the other parameters of the unit cell were optimized by keeping the core height fixed. The study achieved a 37% weight reduction by size optimization considering both thermal and mechanical loads.

1.2.2. Literature on Sandwich Plates with Egg-Box Cores

Deshpande and Fleck [20] developed an analytical model to predict the collapsing response of the egg-box structure with travelling plastic hinge mechanism under compressive loading. The material used in that study was leaded gun-metal with high ductility. Collapse mechanism maps including collapse modes of elastic buckling, travelling plastic hinge and material tearing were constructed. The authors suggested that these maps could be used to maximize the energy absorption per unit mass at a given value of collapse stress. The analytical model was compared with the finite element model and the experimental results. It was concluded that the travelling hinge model matched well with the measurements. The analytical investigation found out that the egg-box material was a better energy absorber due to the travelling plastic hinges as well as strain hardening observed during deformation whereas metallic foams deformed by stationary hinges resulting in less energy absorption.

Zupan *et al*. [21] measured the plastic collapse response of aluminum egg-box panels subjected to out-of-plane compression and drop-weight test under unconstrained, bonded and constrained boundary conditions. The collapse strength was examined for egg-box panels made of aluminum alloy Al 1050 H111. It was reported that the collapse strength and energy absorption depended highly on the level of in-plane constraint and the collapse was governed by either plastic buckling or by travelling plastic hinge mechanism. Additionally, a 3D finite element shell model was developed to simulate the experimental case. Drop-weight tests were conducted and measurements were taken using accelerometer-fitted dropped mass. Drop-weight tests showed that the strain rate strongly affects the plastic collapse strength of the aluminum alloy rather than the velocity of the weight. A direct comparison between the egg-box structure and metallic foams resulted that egg-box structures are favorable candidates for energy absorption.

Akisanya and Fleck [22] conducted experiments and finite element analyses on thin-walled conical metallic frusta to determine quasi-static plastic collapse mechanism for combined shear and out-of-plane compression. The shear collapse of the frusta was studied for the cone angles of 30° and 45°. The study revealed that geometric imperfection had a small effect on the shear collapse load while the collapse load was highly dependent on the magnitude of imperfection. The initiation of necking in the wall of the frustum limited the energy absorption, however loading beyond the onset of buckling led to excessive stretching and tearing from the frustum's conical section. The shear strength and out-of-plane collapse strength were reported to increase linearly with increasing relative density.

Chung *et al.* [23] conducted an experimental study on composite egg-box panels to explore their deformation behavior and energy absorption capacity. The specimens were manufactured using silicon rubber molds with vacuum bag degassing molding. The materials used in that study were carbon/epoxy plain weave fabric and glass/epoxy 4-harness satin weave. The effects of different materials, thicknesses and lay-up sequences were examined. The study revealed that the compressive behavior of the composite egg-box panels could be improved by adjusting the lay-up sequence to modify the stress distribution within the material. It was seen that the highest energy absorption was obtained for the CFRP egg-box panels while GFRP panels with symmetric lay-up configuration had the minimum cost.

Yoo *et al.* [24] performed compressive tests on foam-filled composite egg-box sandwich structures to evaluate their energy absorbing capabilities. In that study, materials used for the foam-filled core structures were CFRP $[0]_{nT}$, CFRP $[45]_{nT}$ $(n = 3, 4)$ and GFRP $[0/90]_s$, $[\pm 45]_s$. The face plates with GFRP $[0/90]_s$ lay-up sequence were bonded to the top and bottom surfaces of the egg-box cores using adhesive bonding to obtain a sandwich structure. Self-expanding polyurethane (PU) foams were sprayed into the cores to fill the cavity. The tests for the unfilled panels showed stress peaks at relatively low strain levels while the foam-filled sandwich structures did not show an initial peak and showed a similar plateau response. This difference was attributed to the premature buckling of the foam-filled egg-box sandwich structures. The study concluded that the unfilled cores were preferred where the peak load was not critical, while the foam-filled cores had better performance where the peak load and the energy absorbing capacity were both considered.

Nowpada *et al*. [25] investigated the quasi-static behavior of aluminum egg-box panels with a novel shape. The unit cells were specifically shaped to increase the energy absorption capability. The egg-box panel consists of finite number of rows positioned alternately upright and upside down. In order to understand the collapse mechanism and factors affecting the energy absorption, compressive tests were conducted on an unconstrained single unit cell and a unit cell positioned within a panel naturally constrained by the flanges of the neighboring unit cells. The study found out that the energy absorbed by the naturally constrained unit cell is 80% higher than the unconstrained unit cell. This difference was attributed to the restriction of flattening of the unit cell and gradual deformation of the structure. During the deformation of the constrained unit cell, formation of plastic hinges and progressive folding throughout the thickness of the structure led to a large energy absorption. In another study conducted by the same authors [26], the egg-box panel was proposed as a candidate structure to be used in front and sides of commercial vehicles to decrease the impact load transfer to the pedestrians during a crash. The crashworthiness of the egg-box was compared with metallic foams, thin-walled tubes and honeycomb structures. As a result, the egg-box structure came forward with its stable kinetic energy dissipation rate and higher energy absorption capability due to reversed plasticity and cost-effectiveness.

Haldar *et al*. [27] investigated the compressive properties of egg-box sandwich structures by performing quasi-static compression tests and impact tests. The tests were simulated using finite element analysis for both loading conditions. The materials used in this study were carbon-fiber-reinforced epoxy and glass-fiber-reinforced epoxy manufactured by compression molding. The identified failure modes were core-web flattening, local crushing of the cell and delamination in the cell walls, followed by debonding between core and faces. The study showed that the compressive strength increased as the web thickness increased however, failure consistently occurred due to delamination and local crushing at inclined faces of the unit cells. The rate of loading was observed to affect the response of glass fiber reinforced epoxy slightly more than carbon fiber reinforced epoxy.

Cai *et al*. [28] investigated the feasibility of manufacturing a double-curved panel from an initially flat sandwich plate. In that study, the material of the face sheets was 4343 aluminum alloy and the core material was 3668 aluminum alloy. Analytical models were developed to predict skin buckling and the limiting bending radius for the wrinkling. The fracture limit curve and related analytical formulations to predict the core cell fracture were given. The results of multi-point forming experiments and finite element analyses showed that the dominant failure modes were skin wrinkling, skin dimpling and core cell fracture. In that study, sandwich panels were formed with good quality using multi-point forming method. It was concluded that multi-point forming was a useful method to manufacture double-curved sandwich panels.

In a study conducted by Liang *et al*. [29], global buckling was classified as one of the major failure modes affecting the formability of egg-box sandwich plates. In that study, aluminum alloy 5050-0 and 5083 were selected as the face and the core material, respectively. An analytical model based on the elastic and perfectly plastic material model was developed to approximately predict global buckling of the sandwich plate. The investigation on the effect of geometric parameters on forming concluded that the sandwich plates with thick skins were better formed compared to those with thin ones. In addition, an important correlation was observed that the limit forming radius greatly decreased as the size of the unit cell decreases. The type and the location of defects in multi-point forming process were observed to be in good agreement with the numerical results. The experimental study also proved that egg-box sandwich plates could be successfully manufactured without any forming defects.

From the literature review, it was observed that shape optimization aiming to maximize the flexural strength of the egg-box composite sandwich structures has received little attention of the researchers. The egg-box type sandwich plates have attracted attentions mainly due to their high-energy absorption capacity. In this study, a two-variable shape optimization study is performed using Nelder-Mead method for the core structure to maximize the overall bending strength of the composite sandwich plate. The design variables are selected as contact length and base angle of the unit cell. A finite element model is developed in ABAQUS environment to simulate the behavior of the composite sandwich plate under three-point bending. The first-ply failure load level is determined based on Tsai-Hill failure criterion using the secant algorithm. The model is validated by comparing its predictions with the results obtained by three-point bending tests. The optimum core structure is manufactured by using a 3D-printed polylactid acid (PLA) mold. The face sheets and core structure are manufactured using vacuum infusion process (VIP). The comparison between the test results and the finite element model shows that the finite element model sufficiently predicts the first-ply failure load level and failure region.

1.3. Objective of the Study

The objective of this thesis study is to maximize the bending strength of a sandwich composite structure with an egg-crate shaped core under three-point bending loading. The core topology of the sandwich plate is the same as the one in the previous study [30]. The previously developed finite element model is used, but simplified to reduce the computational burden in optimization studies. As in the previous study, Classical Lamination Theory (CLT) and micromechanics are applied to the tension test results to evaluate the mechanical properties that are used as inputs in the finite element model.

The bending strength is maximized by optimizing the shape of the core. Two design parameters, contact length and base angle of the unit cell, are considered as optimization variables. Nelder-Mead search algorithm is used to find the optimum values of these variables. The strength of the plate is taken as the load level resulting in Tsai-Hill index value being equal to 1.0. Since the size of the plate and support locations vary with the number and size of the unit cells, the strength of the sandwich plate is normalized by a factor derived based on the classical beam theory. Specimens with the optimum core geometry are manufactured using a 3D-printed PLA mold. The face sheets and core structure are both manufactured from E-glass non-crimped fiber-reinforced epoxy resin via vacuum infusion process (VIP).

Tensile tests are performed with quasi-isotropic $[0/45/-45/90]_s$, cross-ply $[0/90]_{2s}$ and angle-ply symmetric $[45/-45]_{2s}$ lay-ups to obtain the material properties of unidirectional laminates and identify the damage mechanisms. Acoustic Emission (AE) monitoring is used to detect the damage events. Failure load levels in the test specimens are determined by considering the load-displacement curves and changes in the values of different AE parameters during loading.

The motivation of this study is to optimize the core shape to maximize the bending strength of the overall composite sandwich plate. The optimized core structure may be an attractive candidate for the designers where the application requires high bending strength in all directions. Unlike honeycomb cores, the angulated side faces and large contact areas of the core structure improve the shear resistance of the sandwich plate. The empty space within the core structure can be filled with foam to meet some other design considerations depending on the application.

2. THEORETICAL FRAMEWORK

2.1. Failure Mechanisms

Initiation of failure in composite laminates is not a single event. Failure initiation is a series of events whereby individual failure mechanisms develop and interact in a way dependent on the relative orientation of plies within a laminate, the type of loading, and the state of damage in the laminate [31]. The development of failure in a typical composite laminate is displayed in Figure 2.1. The fundamental failure mechanisms in tensional loading are matrix cracking, debonding, delamination and fiber breaking, while kinking is a common damage type observed in compressive loading.

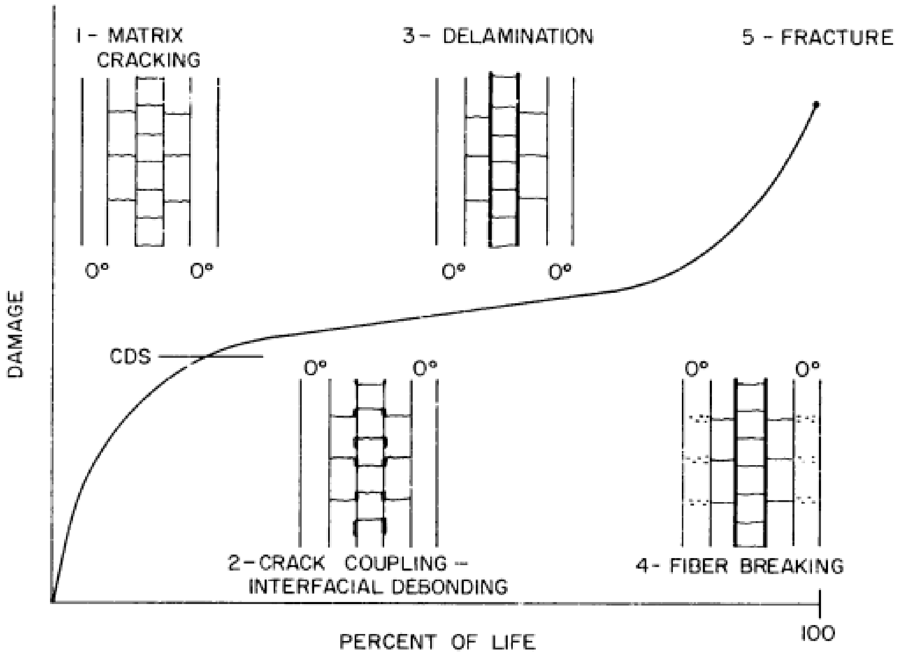

Figure 2.1. Development of damage in composite laminates [31].

Fibers are load-carrying components of composite laminates. Therefore, fiber breakage is a critical damage mechanism leading to the ultimate fracture of the composite laminate during tensile loading. The progression of fiber breakage can be divided into three stages. In the first stage, single fibers break at various locations of the composite laminate at low stress levels. Secondly, the fiber break clusters grow in the vicinity of existing single fiber breaks such as doublets, triplets and so on as the tension load increases. At the final stage, the size of the fiber break cluster reaches to a critical level and the composite laminate eventually fractures (Figure 2.2) [32].

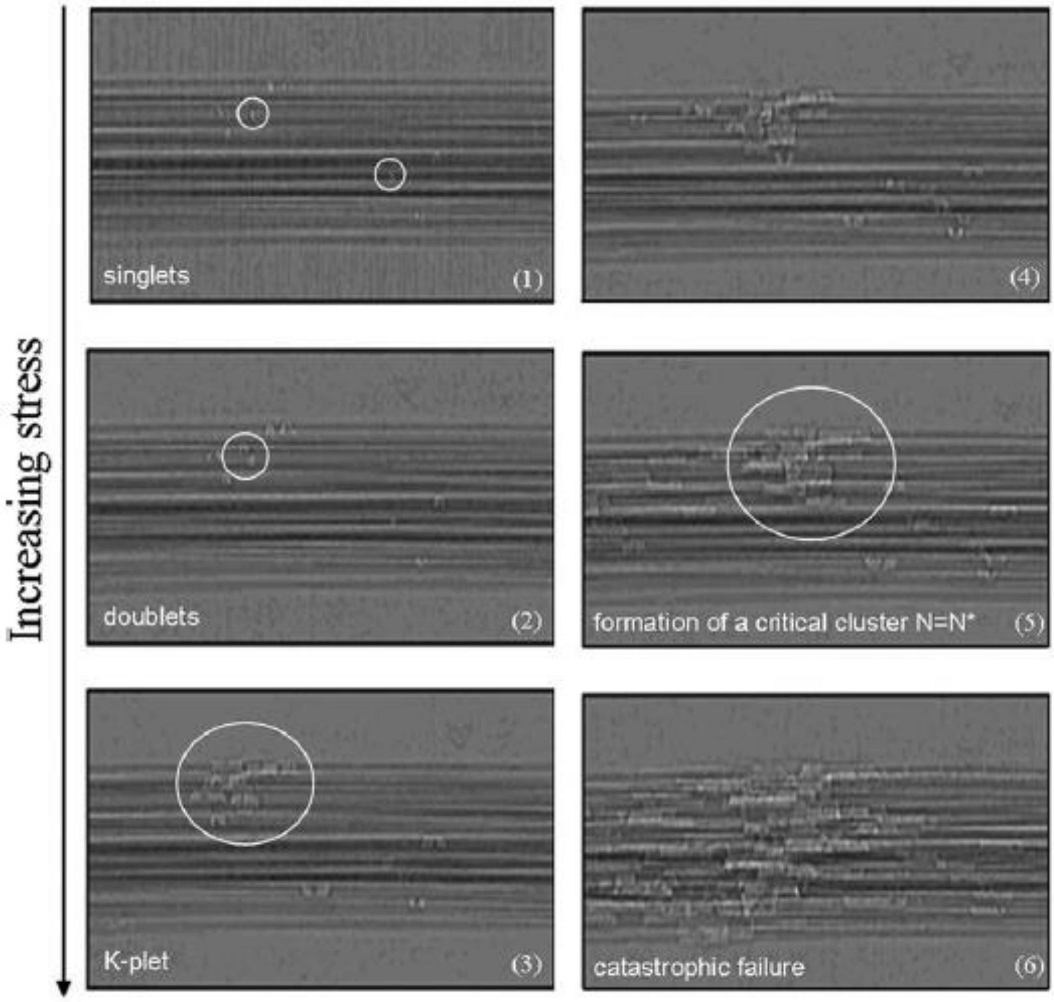

Figure 2.2. The evolution of damage in the form of fiber breaks [32].

The interface between fiber and matrix is prone to cracking due to the inherent stress concentration and residual stresses from manufacturing processes. The stress concentration areas at the interface lead to micro-cracks under loading due to dissimilar elastic properties of the fiber and matrix. These micro-cracks run circumferentially around fibers and result in debonding at the fiber-matrix interface (Figure 2.3a). After these cracks grow to a certain length, they propagate into the matrix and coalesce with each other (Figure 2.3b). The coalescence of the individual debondings gives rise to a transverse crack and failure of the lamina at macroscopic level [33].

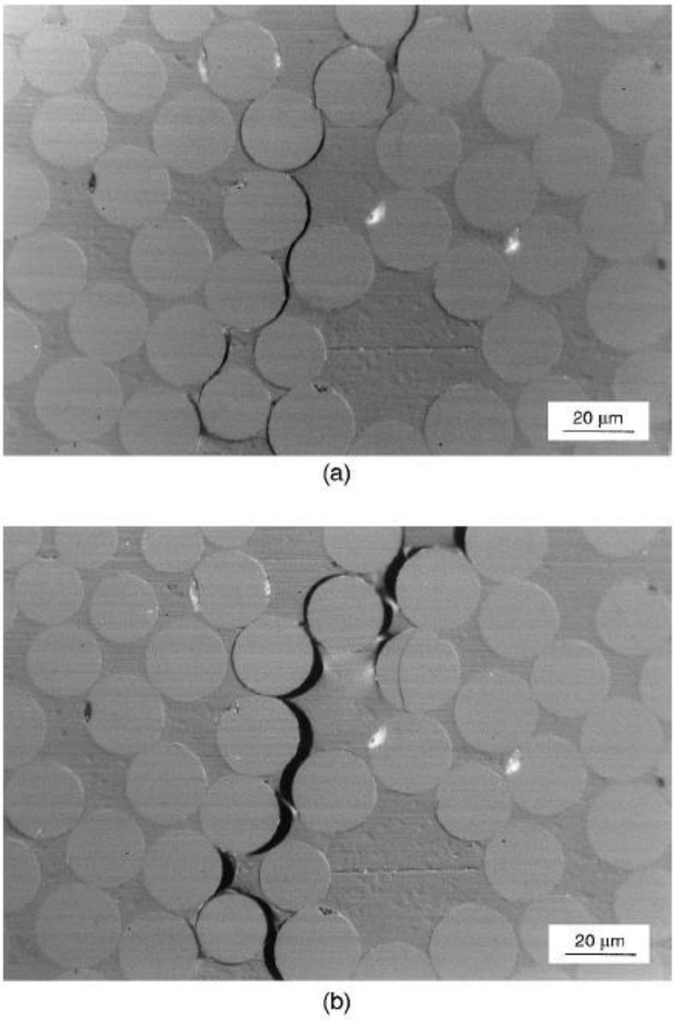

Figure 2.3. (a) Fiber-matrix debonding and (b) transverse matrix crack [34].

Transverse cracking is a frequently observed intralaminar failure mechanism in composite laminates due to lower failure strain levels of transversely loaded laminae compared to laminae with fibers oriented in different directions. As debondings merge with each other, transverse cracks run through the thickness of the lamina and terminate at the lamina boundary. Particularly, the number of transverse cracks increases rapidly in the plies where fibers are oriented perpendicular to the loading axis. At low stress levels, transverse cracks are subcritical; however, increasing number of transverse cracks reduces stiffness and induces fiber breakage in the adjacent plies or local delamination which can lead to buckling failure in compression [34].

Terminated transverse cracks at the lamina boundaries generate local stress concentrations and these stress concentrations lead to delamination between plies of laminate (Figure 2.4). Delaminations generally result from excessive out-of-plane or interlaminar stresses being developed at the interfaces between adjacent laminae resulting from sources such as transverse loads, impact loads, notches, and manufacturing defects. Delamination significantly degrades initial load sharing among the laminae with perfectly bonded lamina-lamina interfaces. The disrupted load sharing promotes damage progression and leads to premature failure [35]. The general analytical assessment of delamination requires a fracture mechanics approach to analyze the progression of damage. Delaminations are mostly classified in three modes: mode I (opening), mode II (shear), and mixed mode, which is a combination of mode I and mode II [36].

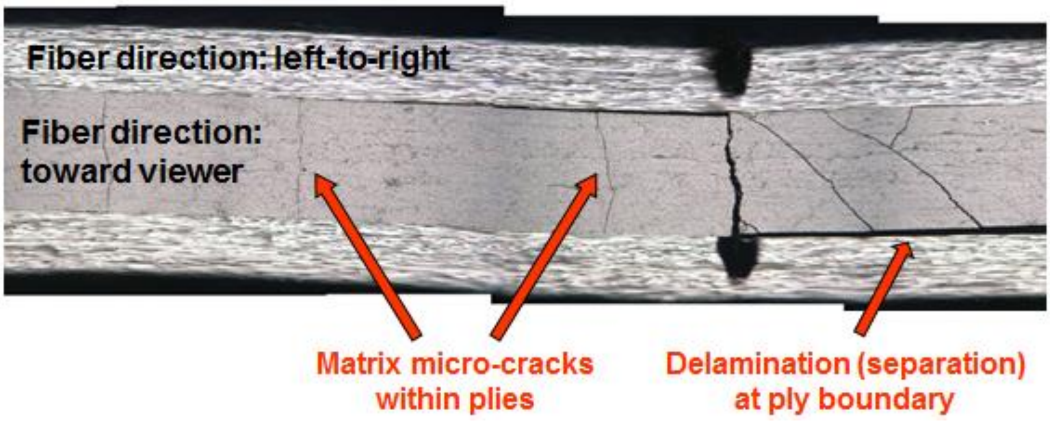

Figure 2.4. Delamination at the boundary between plies [37].

In the case of compressive loading, kinking is a fundamental damage mechanism. Local shear deformation in the matrix is observed under compressive loading due to the fiber waviness and misalignment in composite laminate. The shear deformation leads to the formation of bands and flow of the matrix results in bending of the fibers. When the bending stresses reach values comparable to tensile strength of the fiber, the fibers start to break and form kink bands (Figure 2.5) [38].

The catastrophic failure of a composite laminate rarely occurs with first-ply failure. Instead, the structure ultimately fails due to the progression and accumulation of local failures as the load increases. Failure of a ply causes a reduction in the overall laminate stiffness and strength. Therefore, the stresses on remaining plies are redistributed and they keep carrying the load. The progression of failure continues for the remaining plies until no ply can bear the load.

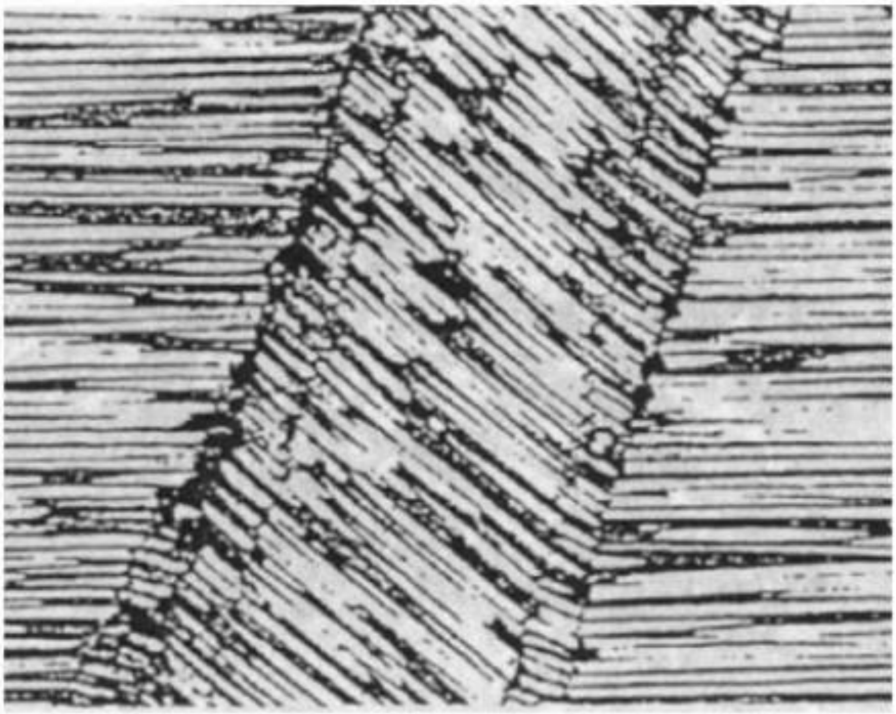

Figure 2.5. Kink band formation [39].

2.2. Failure Criteria

For isotropic materials, failure is simply predicted by comparing applied stress to the strength of the material or some other allowable stress. The material strength properties are the same in all directions and there is no principal material direction. However, strength properties and failure types vary with direction of loading for orthotropic composite lamina. The tensile and compressive strengths in the principal material directions generally are not the same and the failure type can vary from fiber breakage when in tension to fiber buckling and delamination when in compression. Therefore, development of failure criteria is required to analyze the design problems in the case of multi-axial loading or multi-directional laminates [40].

A failure criterion for orthotropic lamina generally involves the extension of an isotropic failure criterion to account for orthotropy. A failure criterion simply defines a stress or strain limit above which failure occurs. Alternatively, failure envelopes are developed to account for multi-axial stress states. The failure envelopes are not derived from micro-mechanical failure modes such as crack growth, delamination and fiber breakage which take place within the composite laminate during the loading. Instead, the strength data of orthotropic composite lamina in different directions is curve-fitted to simply use in a design stage. These lamina strength values are obtained from unidirectional tension tests applied for unidirectional lamina [40].

A failure criterion is applied on ply-by-ply basis in a composite laminate. The determination of the stress or strain state of each lamina is required to apply the desired failure criterion. Classical Lamination Theory (CLT) can be utilized to perform the stress and strain calculations for each lamina. Analytically, a laminate may be assumed to have failed when the failure criterion for any of its lamina is exceeded. However, when one ply fails, load redistribution usually takes place among the remaining plies and the first-ply failure does not necessarily mean total failure of the laminate.

The failure criteria for composite laminate can be grouped under two groups as [41]

- Limit or non-interactive failure criteria: Failure is predicted by comparing each lamina stress or strain with corresponding ultimate stress or strain. No interaction among different stress components is considered. Non-interactive failure criteria include maximum stress and maximum strain theories.

- Interactive failure criteria: The stress or strain components interact with each other in a single compact equation where the failure is formulated. Total failure is predicted without referencing to particular failure modes. Tsai-Hill and Tsai-Wu are interactive failure criteria.

- Partially interactive or failure-mode-based failure criteria: Separate criteria are defined for fiber and matrix or interface failures. This group of criteria includes Hashin-Rotem and Puck theories.

2.2.1. Maximum Stress Criterion

In the maximum stress criterion, if at least one of the stresses in the principal coordinates is greater than or equal to the respective strength, the lamina is considered to have failed [40]. That is, for tensile stresses,

$$\sigma_1 \geq X_t \qquad \sigma_2 \geq Y_t$$

for compressive stresses, $\sigma_1 \leq X_c \qquad \sigma_2 \leq Y_c$

and for the shear stress, $|\tau_{12}| \geq S$

where X_t, Y_t, X_c, Y_c and S are tensile strength in fiber direction, tensile strength in transverse direction, compressive strength in fiber direction, compressive strength in transverse direction and shear strength, respectively. It should be noted that there is no interaction between modes of failure in this criterion. Namely, there are five sub-criterion and five failure mechanisms.

In addition, the stresses in the body coordinates must be transformed to the stresses in the principal coordinates before applying this criterion.

2.2.2. Maximum Strain Criterion

The maximum strain criterion is logically similar to the maximum stress criterion. As the name implies, strains are in consideration rather than stresses. If at least one of the strains in the principal coordinates is greater than or equal to the ultimate relative strain, the lamina is considered to have failed [40]. For tensile strains,

$$\varepsilon_1 \geq X_{\varepsilon_t} \qquad \varepsilon_2 \geq Y_{\varepsilon_t}$$

for compressive strains, $\varepsilon_1 \leq X_{\varepsilon_c} \qquad \varepsilon_2 \leq Y_{\varepsilon_c}$

and for the shear strain, $|\gamma_{12}| \geq S_\varepsilon$

where X_{ε_t}, Y_{ε_t}, X_{ε_c}, Y_{ε_c} and S_ε are ultimate tensile strain in fiber direction, ultimate tensile strain in transverse direction, ultimate compressive strain in fiber direction, ultimate compressive strain in transverse direction and ultimate shear strain, respectively. Although this criterion is classified as non-interactive, Poisson's effect allows interaction of stress components to some extent.

As with maximum stress criterion, the strains in the principal material coordinates must be found by transformation in order to use this criterion.

2.2.3. Tsai-Hill Criterion

Tsai-Hill failure criterion is an extension of Von-Mises distortional energy yield criterion for isotropic materials as applied to anisotropic materials [42]. Total strain energy in a body consists of two parts, namely, distortion energy and dilation energy. Distortion energy causes change in shape while, dilation energy causes the change in volume. Von-Mises criterion assumes that the material fails when the maximum distortion energy of the body exceeds the distortion energy at yielding of the same material in tension.

According to this criterion, the lamina is assumed to have failed when the stress state is such that

$$(G+H)\sigma_1^2 + (F+H)\sigma_2^2 + (F+G)\sigma_3^2 - 2H\sigma_1\sigma_2 - 2G\sigma_1\sigma_3 - 2F\sigma_2\sigma_3 + 2L\tau_{23}^2 + 2M\tau_{13}^2 + 2N\tau_{12}^2 = 1$$

where G, H, F, L, M and N are the material strength values. This equation defines a failure envelope and any stress state which lies within this envelope is safe and the one which lies on or outside the envelope is considered as failure.

The material strength values correspond to failure stresses in one dimensional loading. If only τ_{12} acts on the body, then failure occurs at S, shear strength.

$$2N = \frac{1}{S^2}$$

Similarly, if only σ_1 acts on the body, $G + H = \frac{1}{X^2}$

if only σ_2 acts on the body, $F + H = \frac{1}{Y^2}$

and if the strength in the out-of-plane third dimension is designated by Z, and if only σ_3 acts, then

$$F + G = \frac{1}{Z^2}$$

If the three equations above combined, each failure strength parameters can be derived as

$$2F = \frac{1}{Y^2} + \frac{1}{Z^2} - \frac{1}{X^2}$$

$$2G = \frac{1}{X^2} + \frac{1}{Z^2} - \frac{1}{Y^2}$$

$$2H = \frac{1}{X^2} + \frac{1}{Y^2} - \frac{1}{Z^2}$$

For plane stress condition in the 1-2 plane of a unidirectional lamina with fibers in the 1-direction, $\sigma_3 = \tau_{13} = \tau_{23} = 0$. Also, it is clear that the strengths in 2-direction and 3-direction is equal. Thus, Tsai-Hill criterion reduces as

$$\frac{\sigma_1^2}{X^2} - \frac{\sigma_1 \sigma_2}{X^2} + \frac{\sigma_2^2}{Y^2} + \frac{\tau_{12}^2}{S^2} = 1$$

The appropriate values of X_t or X_c and Y_t or Y_c must be substituted depending on the signs of σ_1 and σ_2. As a result, a different surface is generated in each section of 3D stress space σ_1, σ_2 and τ_{12}. Since S has only one value, the surface is symmetrical about the plane $\tau_{12} = 0$.

The scope of this study is bounded by the bending strength maximization of a sandwich plate with egg-crate shaped core by shape optimization. Since the ultimate failure of the plate and progression of damage is not analyzed with the finite element model, the first-ply failure is sufficient for the purpose of strength maximization. In this respect, Tsai-Hill failure criterion is kept as the failure evaluation basis in the same way with the previous study [30]. The sandwich plate is assumed to have failed when Tsai-Hill criterion for any location throughout the whole structure is equal to 1.0.

3. MANUFACTURING OF THE SANDWICH SPECIMENS

Sandwich structures can be made of different materials like metals, composites, or polymers having various geometric shapes. Therefore, different manufacturing methods need to be used depending on the geometry and the material. Generally, sandwich composites have isotropic metal sheets or laminated composite sheets as face sheets. However, most of the composite sandwich applications use isotropic materials for the core section. In this study, both the core and face sheets are laminated composites. The face sheets and core section are manufactured separately by vacuum infusion process (VIP). This manufacturing method is explained in detail in the following section.

3.1. Vacuum Infusion Process (VIP)

Vacuum infusion process (VIP) is a widely-used technique to manufacture large-scale composite parts. This technique uses vacuum-induced pressure to drive liquid resin into laminate. The dry reinforcements such as fiberglass or carbon fiber are laid into the mold and an initial vacuum is applied before the resin is driven into the laminate. The resin is sucked into the laminate only after ensuring the level of vacuum by the proper sealing and appropriate setup of the resin and vacuum lines. This process results in a stronger and lighter product with more uniform resin distribution compared to an open mold process [43].

First, the surface of the mold is covered by a mold release wax to provide easy removal of the manufactured part. In addition, wax coating prevents possible damage onto the mold during the forced extraction of the final part and ensures reusability of the mold. Layers of dry reinforcements are laid onto the leak-proof mold after the application of the wax. A peel-ply layer is placed onto the dry reinforcements to separate the materials that will be removed later after the manufacturing. Onto the peel ply, an infusion mesh is laid to increase the flow rate of the resin by providing low resistance conduit for the resin. Two spiral tubes are wrapped in peel ply and one tube extends at one end of the reinforcements as resin feed line and the other tube extends at the other end as vacuum line. Finally, the vacuum bag is placed over at the top and proper sealing is applied across the perimeter of the reinforcement by sealant tapes. The overall setup for the vacuum infusion process is shown in Figure 3.1 [44].

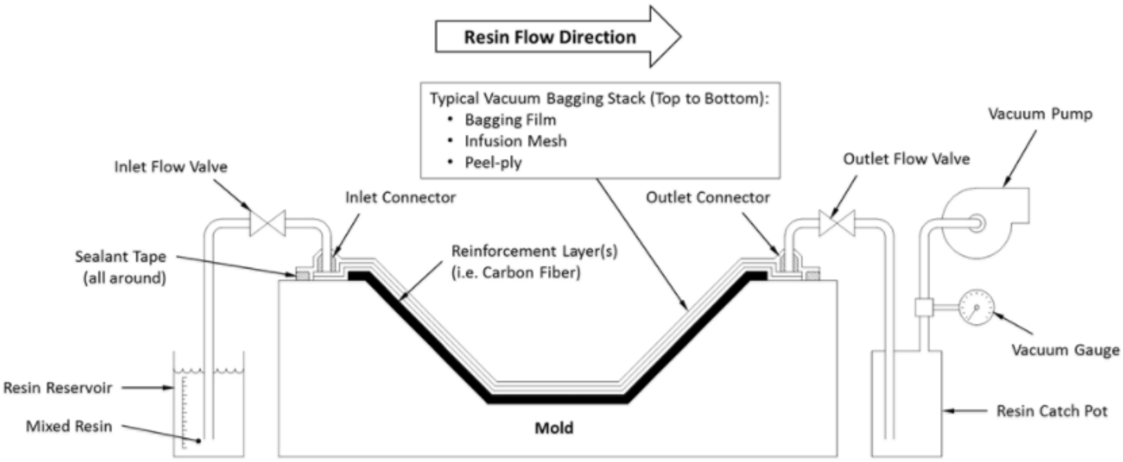

Figure 3.1. Vacuum infusion setup [44].

Before suction of the resin into the laminate, the air trapped between the bag and the mold is evacuated by a vacuum pump. The level of vacuum pressure depends on the permeability of the materials, the complexity and desired quality of the final part. Typically, about 95% of the maximum vacuum pressure of the pump is desired for the good quality part except the cases, for example a low-density foam core could be crushed by excessive vacuum. After the initial vacuum, the vacuum pump is closed for a while and the level of vacuum is checked on the gauge. If the vacuum pressure continues to stand completely or fairly constant, then the vacuum bag and mold is sufficiently leak-proof to continue the vacuum infusion process. However, in the case of rapid vacuum pressure drop, the process should stop and the air leaks need to be detected and eliminated before continuing the process. The acceptable leak rates depend on the size of the part to be manufactured. While, a leak rate of less than 3 mbar/min is acceptable for large parts such as boat hulls, 0.3 mbar/min leak rate may be acceptable for smaller or critical parts [45].

Once an appropriate level of leak-proofing is achieved, the line of the vacuum pump can be reopened. After the vacuum pump is opened, the resin supply line is opened and the resin is driven into the part with the aid of the pressure difference between the atmospheric pressure acting on the resin and the vacuum pressure, plus or minus static head of the resin column arising from the elevation of the resin supply relative to the part. The correct positioning of resin feed lines and vacuum lines are crucial for the complete infusion of the resin into the reinforcement.

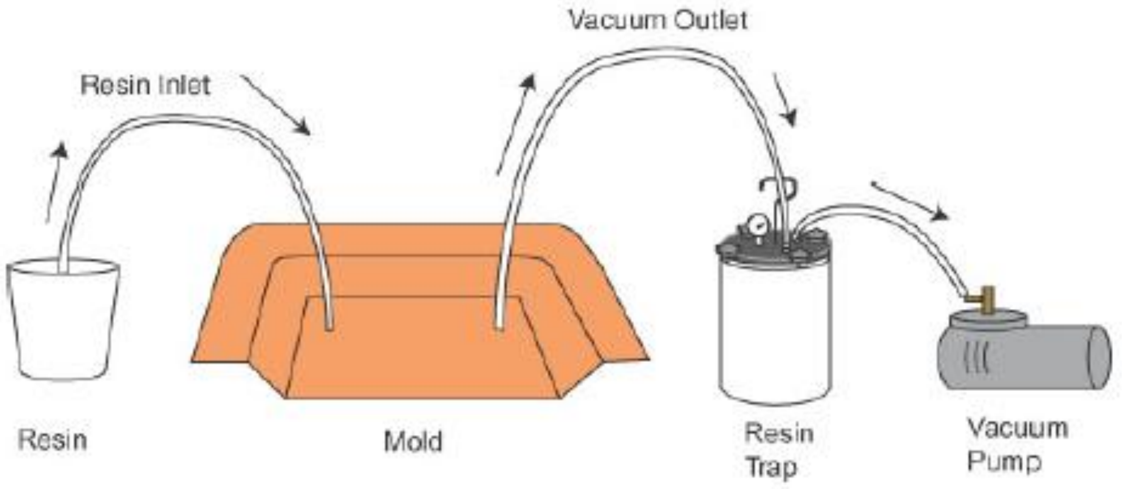

Figure 3.2. Vacuum infusion diagram [43].

When thermosetting resins are used, a certain period of time is needed for the resin to cure after the laminate is completely diffused with the resin. This period varies from a few minutes to a few hours depending on the type of resin and the size of the part to be manufactured. After the resin is solidified, the bag and the part can be extracted from the mold. The final part is a homogeneous structure, with all components bound together within the resin matrix.

The benefits of vacuum infusion process may be grouped as follows [46]:

- Higher fiber-to-resin ratio by the suction of the excess resin out of the laminate.
- Higher stiffness and strength characteristics of the final part.
- High reliability and repeatability with less human errors.
- Minimal part shrinkage with good surface profile and accuracy.
- Efficient way of manufacturing complex geometries.
- Cleaner way with no volatile organic compound (VOC) emission.

Although, vacuum infusion process is a superior method for manufacturing higher quality parts with higher mechanical properties compared to other manufacturing methods, the disadvantages listed below should be considered [46]:

- Complicated setup and needs to provide proper vacuum and resin supply lines.
- Scrapped parts in case of vacuum leak.
- Inferior surface finish due to fabric print compared to the open mold process however, the finish can be improved by using a barrier coat.
- Materials used in vacuum infusion process cost more than standard resins and fabric.
- Usage of harmful chemicals such as cleaners, wax, and resin.

3.2. The Manufacturing Procedure

Sandwich composite specimens used in the tests are manufactured by vacuum infusion process (VIP), which is explained in the previous section. In this section, the manufacturing process is summarized step-by-step. Most of the steps presented in this section are the same with the previous study [30]; however some additional steps are performed due to the higher level of complexity of the core geometry used in this study.

- The reinforcement material is E-glass fiber. The glass fiber reinforcements are commercially available in rolled form with desired lay-up and densities. The operator cuts the glass fiber from the roll and sizes by a guillotine paper cutter in required dimensions (Figure 3.3). Then, the glass fiber layers are positioned in the desired stacking sequence.

- A 3D-printed PLA mold is used for the manufacturing of the core section. The surface of the mold has a surface profile tolerance of 0.2 mm. The surface quality of the mold should be sufficiently fine to avoid sticking of the composite material onto the mold surface. The mold surface is coated with Loctite Frekote® mold release agent to improve the surface slippage for easy removal of the final product from the mold (Figure 3.4). After the coating, Loctite Frekote® is allowed to cure for 15 minutes.

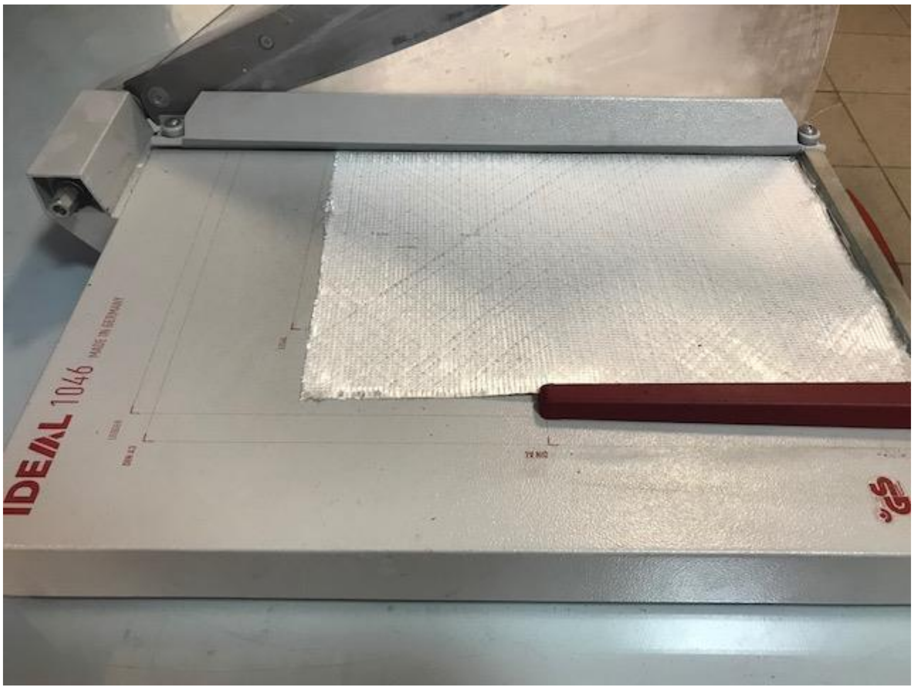

Figure 3.3. Guillotine paper cutter used for sizing the glass fiber reinforcements.

- After the application of Loctite Frekote®, mold release wax is brushed onto the mold surface twice to ensure that the surface is smooth enough to avoid sticking of the final material to the mold. After the mold release is allowed to dry for 15 minutes, Scotch-Weld™ adhesive spray is sprayed onto the waxed mold surface to provide sticking of the reinforcement to the mold and ease the following forming process.

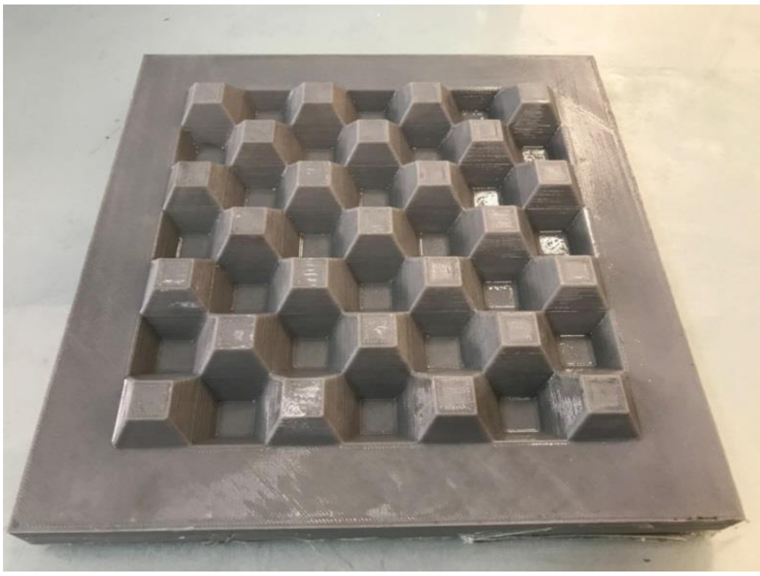

Figure 3.4. Loctite Frekote® applied mold.

- The glass fiber reinforcement is laid onto the mold and formed carefully by hand to give the shape of the mold. Since the core geometry is complex and the reinforcement is inelastic, this step is cumbersome. The reinforcement layers should be properly forced into the trenches in the mold. After manually forcing the reinforcement into the trenches, the other counterpart mold is placed onto the reinforcement. Also, a 50-kg weight is placed onto the top mold to provide better forming (Figure 3.5).

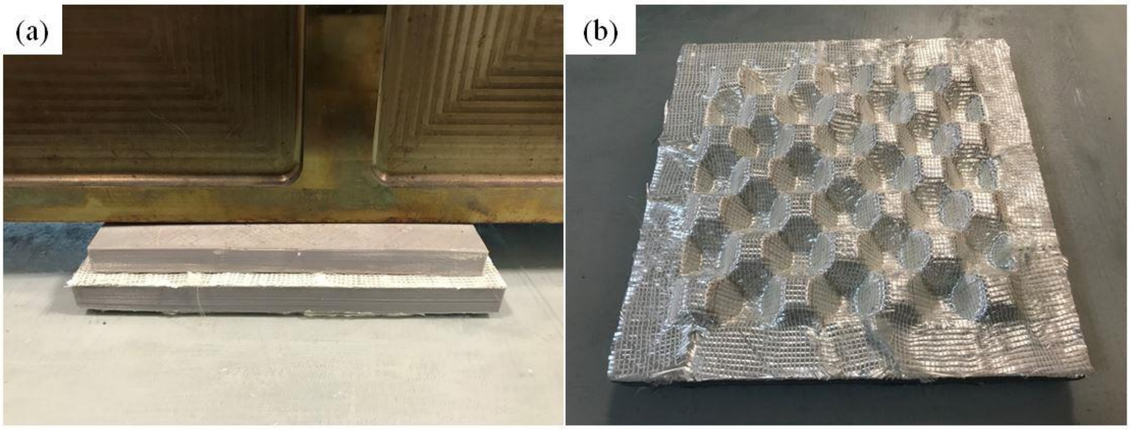

Figure 3.5. (a) Weight-pressed molds and, (b) final shape of the reinforcement.

- VIP needs a rigid and clean surface on which the dry reinforcements are placed. A properly cleaned thick glass is sufficient for two face sheets. The glass surface on which dry reinforcements are placed is properly cleaned with thinner.

- The lines on which sealing bands are to be stuck are taped with a paper tape since the mold surfaces are coated by mold release wax. Direct contact of the tape with the wax may reduce its sealing performance and cause leakage.

- Mold release wax is applied to the whole glass surface to avoid sticking of the mold to the glass (Figure 3.6).

- A peel ply layer is placed onto the dry reinforcements to separate the parts that will be removed after the manufacturing (Figure 3.7). Otherwise, when the dry reinforcement is impregnated under the vacuum pressure, the resin may stick with the other parts and prevent proper separation. For this reason, the peel ply should be large enough to cover the part.

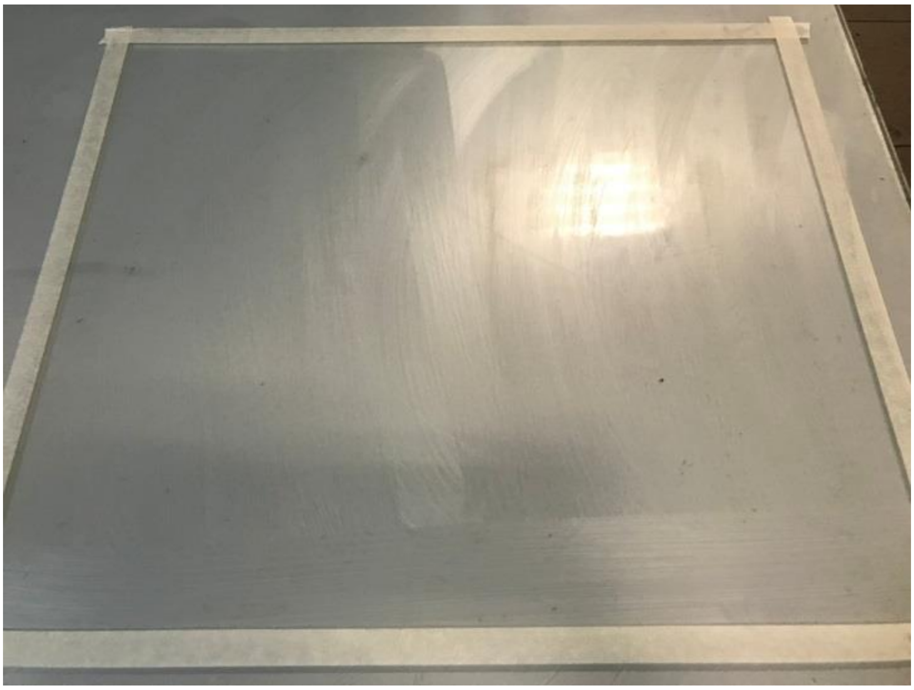

Figure 3.6. Cleaned and waxed glass surface.

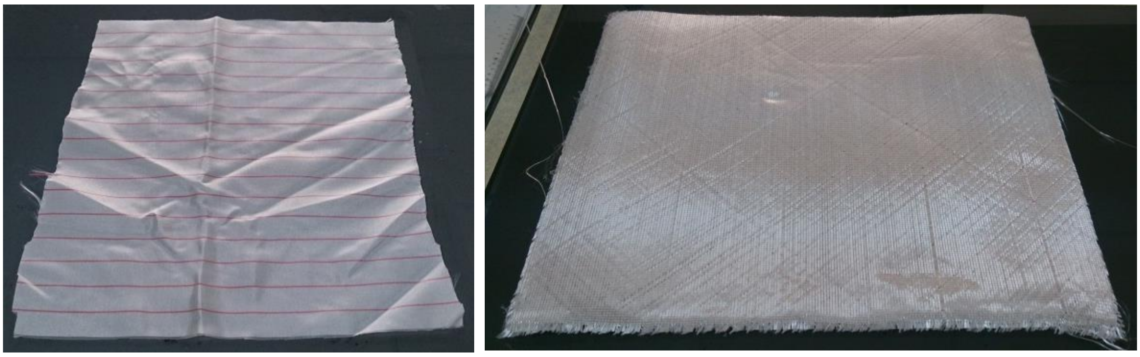

Figure 3.7. (a) Peel ply, and (b) E-glass fiber reinforcement.

- The resin material is epoxy. The flow rate of epoxy under vacuum pressure should be sufficiently high to diffuse into the whole part before solidification starts. A layer of infusion mesh is cut in approximate dimensions of the part by the operator and laid onto the part to increase the flow rate of the epoxy to avoid premature solidification (Figure 3.8). The infusion mesh also helps the vacuum pump evacuating the air.

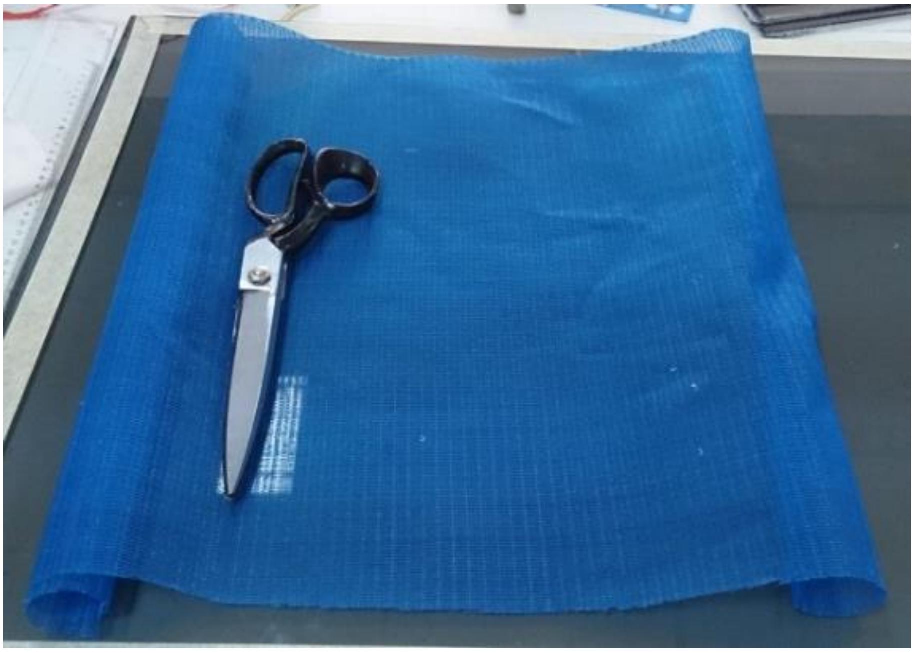

Figure 3.8. Infusion mesh.

- The operator cuts two spiral tubes for both inlet and outlet lines. A spiral tube is placed at one end of the reinforcements as resin feed line and another spiral tube is placed at the other end as vacuum line.

- Vacuum bag is cut in the desired dimensions.

- The paper tapes are replaced with sealing tapes. The mold with reinforcement is placed onto the clean waxed glass surface. The peel ply and infusion mesh are laid over the reinforcement layers (Figure 3.9).

- The resin feed line and vacuum line tubes are placed properly. Their sharp ends are taped with paper tape to avoid the sharp ends from puncturing the vacuum bag and causing leakage.

- A second infusion mesh is placed as an extension of the vacuum line to assist the air evacuation. This mesh does not directly contact with the reinforcement and other parts instead, the connection is made by small filament pads that prevent resin infusion and enabling the air extraction at the same time.

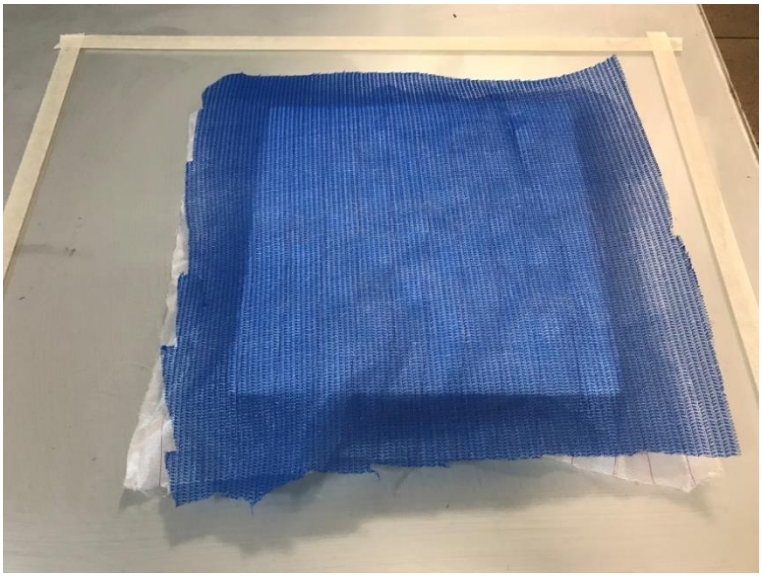

Figure 3.9. Placement of the peel ply and infusion mesh onto the reinforcement.

- The vacuum bag is strongly stuck by the sealing tape and the bag is remained loose appropriately to avoid excessive stretching. The placement of the vacuum bag should be properly done prior to vacuum since it cannot be arranged after the vacuum starts.

- The vacuum pump is turned on to evacuate the air in the bag. Since the resin line is previously blocked by the operator, the pressure in the vacuum bag should drop to a very low value which is ideally zero (Figure 3.10 and Figure 3.11). After the bag is vacuumed, the operator checks the whole setup carefully against leakage. The leakage check is very critical prior to resin infusion, since once the resin infusion is started, it cannot be reversed. The potential air bubbles greatly deteriorate the quality of the end product.

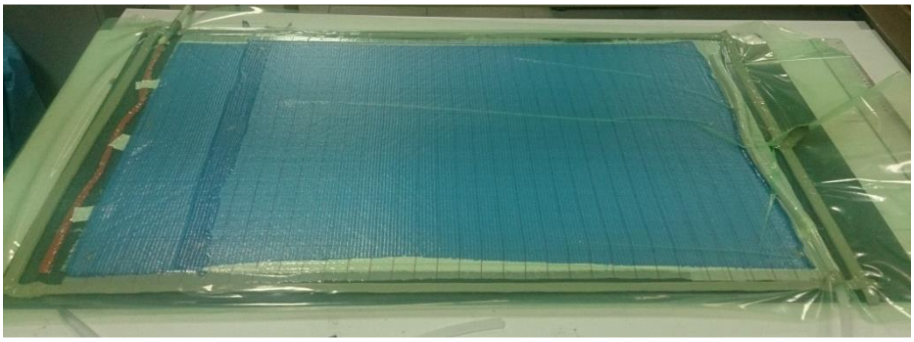

Figure 3.10. Face sheet setup under vacuum pressure.

- A last check is done by blocking the vacuum line and turning off the vacuum pump after evacuating the air in the bag. The pump should prevent the air from being sucked back into the vacuum bag. The vacuum pressure is observed for a while. A pressure rise of 0.1 bars in 15 minutes is acceptable.

Figure 3.11. Core section setup under vacuum pressure.

- Once proper vacuum is ensured, the operator proceeds to prepare the resin. The epoxy is composed of L285 laminating resin with H285 hardener. The resin and hardener are mixed in 100:40 ± 2 ratio as stated in the technical instructions provided with the material. The air bubbles and dissolved gases in the mixture are vacuumed by keeping the mixture pot in the vacuum chamber for three minutes.

- The resin line is immersed into the resin pot before releasing the chocking. As an important detail, the air cannot be allowed to be sucked into the vacuum bag during the impregnation (Figure 3.12). For this reason, the amount of resin in the pot is more than needed. Once the reinforcement is completely impregnated by the resin, the resin line is chocked again. The excessive resin in the vacuum bag is eventually sucked out of the vacuum bag.

Figure 3.12. Resin impregnation to the core section.

- The pot life of the resin depends on the temperature. As the temperature of the resin increases, the rate of the solidification also increases. The vacuum pump should remain on during the whole solidification process. The pump is continued to run for extra five hours for proper gelation. The product becomes ready for use after at least one day curing.

- After the curing, the face sheets or core part is removed carefully from the glass surface or the PLA mold surface. The peel ply is separated from the parts gently without using excessive force to avoid delamination (Figure 3.13).

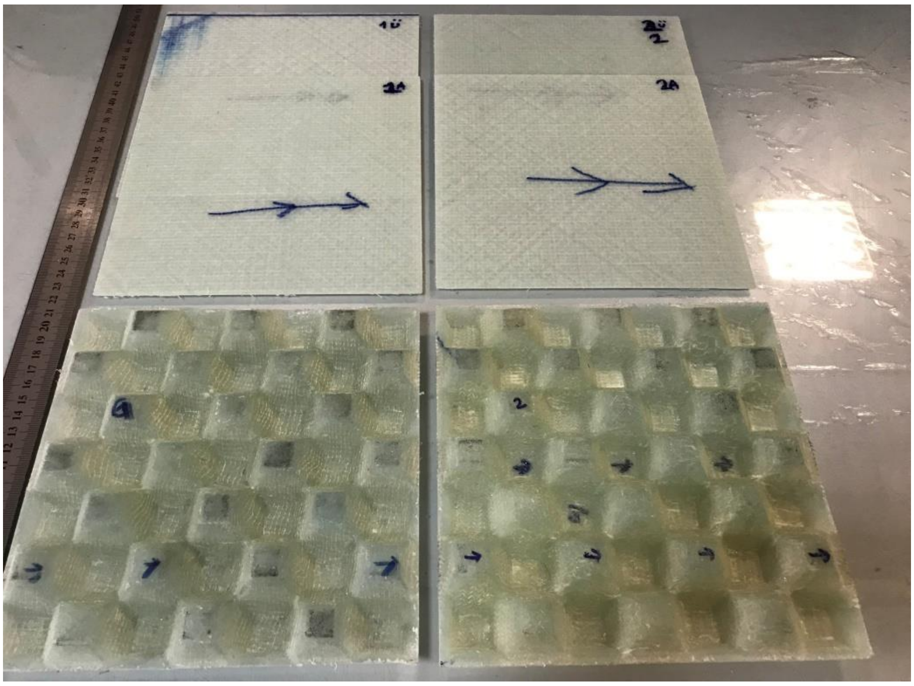

Figure 3.13. Final face sheets and core parts.

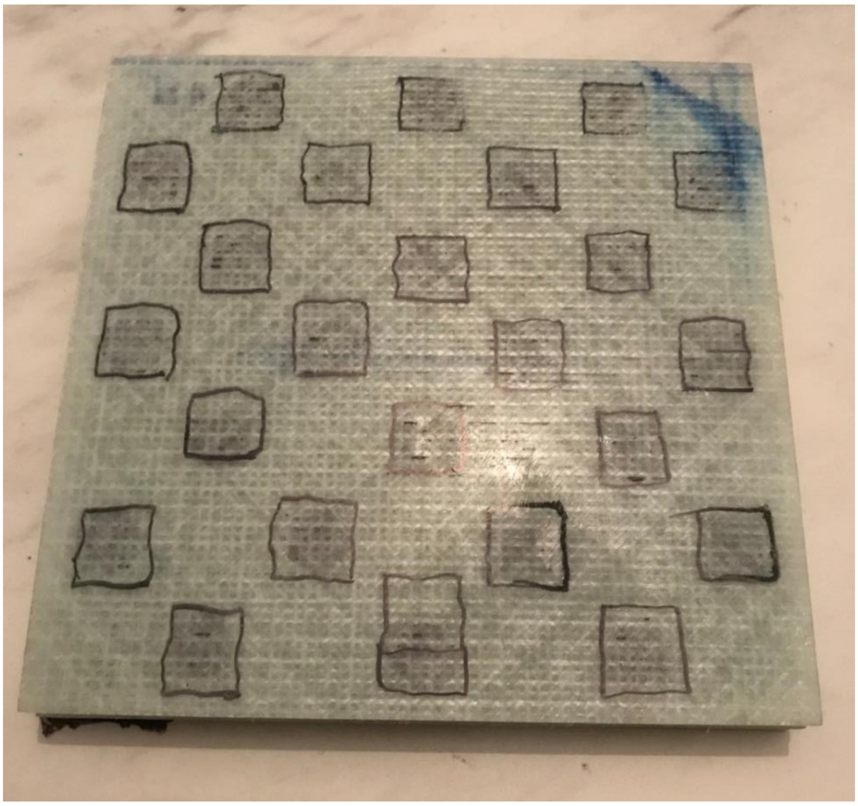

Figure 3.14. Final sandwich plate.

- One sandwich structure consists of one core part and two face sheets. The face sheets are obtained by manufacturing one large plate and then cutting into two parts. It should be noted that the surface finish at the top and bottom sides of the face sheets are not the same. The bottom sides laying onto the glass surface of the face sheets are smooth and these sides are not appropriate for bonding. For this reason, the smooth sides of the face sheets are sandpapered to increase the roughness. The first and second face sheets are bonded to the core part by applying resin. In order to ensure a strong attachment, heavy blocks are placed on top during the curing. While bonding the face sheets to the core, it is made sure that the stacking sequences of the face sheets are correct. The final sandwich plate is shown in Figure 3.14.

The thickness of the two sandwich specimens are measured from four sides and given in Table 3.1.

Table 3.1. The thickness of the sandwich specimens.

		Thickness [mm]	
		Specimen No	
Section	Side No	1	2
Top face	1	1.16	1.13
	2	1.19	1.14
	3	1.23	1.04
	4	1.21	1.06
Core	1	1.50	1.44
	2	1.41	1.40
	3	1.36	1.61
	4	1.37	1.57
Bottom face	1	1.25	1.12
	2	1.07	1.24
	3	1.26	1.16
	4	1.22	1.12

4. TENSION TESTS

4.1. Material

In this study, E-glass fiber is chosen as the reinforcement material. The non-crimped fabric is supplied in two different preforms by the manufacturer, Metyx: Quadriaxial [0/45/-45/90] and biaxial [0, 90]. Tension tests are performed with three different lay-ups: Quasi-isotropic $[0/45/-45/90]_s$, cross-ply $[0/90]_{2s}$ and angle-ply symmetric $[45/-45]_{2s}$ to determine the stiffness and strength characteristics of the composite laminates made of these fabrics. Angle-ply symmetric lay-up is obtained by rotating and cutting biaxial preform 45° in clockwise direction. The physical and mechanical properties of the fabrics are given in Table 4.1 and Table 4.2, respectively.

Table 4.1. Physical properties of quadriaxial and biaxial E-glass fabrics [47,48].

Construction / Product Name	Layer	Fiber Type	Area Weight (gr/m^2)
Q625 E10C-0/45/90/45 Quadriaxial E-Glass-127CM	0°	300+600 Tex	177
	45°	300 Tex	150
	-45°	300 Tex	150
	90°	300 Tex	154
	Stitch	76 Dtex	10
	Total Weight		641 (±3%)
LT300 E10B-0/90 Biaxial E-Glass Fabric-127CM	0°	300/600 Tex	177
	90°	300 Tex	142
	Stitch	76 Dtex	10
	Total Weight		329 (±3%)

L285 laminating resin with H285 hardener is used as the epoxy material. The mixing ratio of the resin and the hardener is given as 100:40 ± 2 in the technical instructions [50]. Since this ratio affects the material properties of the final epoxy resin, it should be ensured during the mixing. The resin and the hardener should be mixed in a pot until it becomes completely homogeneous. Then, the mixture pot is put into the vacuum oven with 0.1 MPa for 5 minutes to evacuate the air bubbles. The properties of the hardened resin are given in Table 4.3.

Table 4.2. Mechanical properties of the fibers [49].

	[0/90] biaxial fabric	[0/45/-45/90] quadriaxial fabric
E_f, elastic modulus of fiber [GPa]	72.4	72.4
ν_f, poisson's ratio of fiber	0.22	0.22
G_f, shear modulus of fiber [GPa]	26.2	26.2

Table 4.3. The properties of the hardened resin [50].

Density [gr/cm^3]	1.12
E_m, elastic modulus of matrix [GPa]	3.2
ν_m, poisson's ratio of matrix	0.36
G_m, shear modulus of matrix [GPa]	1.18

4.2. Preparation of Test Specimens

Three large plates with quasi-isotropic [0/45/-45/90]$_s$, cross-ply [0/90]$_{2s}$ and angle-ply symmetric [45/-45]$_{2s}$ layups are manufactured with VIP. The large plates have the dimensions of 175 mm in width and 250 mm in length. End-tabs with a length of 56 mm are glued to both ends of the large plates using J-B® Weld plastic bonder. After the attachment of the end-tabs, the gauge sides of the tabs are tapered at nearly 45° by the grinder to prevent stress concentrations at these regions. End-tabs prevent the grips of the testing machine from crushing the material at the ends and leading to a premature fracture of the specimen at the grip sections. After the tab grinding, specimens are cut by a water-cooled diamond disc from the large plates. The final specimen dimensions are 25 mm in width and 250 mm in length in accordance with ASTM D3039 testing procedure. The measured dimensions of the final specimens are listed in Table 4.4.

Table 4.4. Dimensions of the test specimens.

Stacking Sequence	Specimen No	Width [mm]	Gauge Length [mm]	Thickness [mm]
Quasi-isotropic: $[0/45/-45/90]_s$	1	24.98	135.00	1.20
	2	24.98	133.00	1.19
	3	24.65	134.40	1.13
	4	24.91	133.70	1.15
	5	24.97	134.50	1.18
	Average	24.90	134.12	1.17
	Std. Dev.	0.14	0.78	0.03
Cross-ply: $[0/90]_{2s}$	1	24.71	135.70	1.30
	2	24.90	137.00	1.33
	3	24.90	136.70	1.28
	4	24.86	135.50	1.36
	5	24.82	136.00	1.35
	6	24.80	135.50	1.30
	Average	24.83	136.07	1.32
	Std. Dev.	0.07	0.64	0.03
Angle-ply symmetric: $[45/-45]_{2s}$	1	24.93	157.00	1.34
	2	24.90	157.00	1.31
	4	25.04	157.00	1.34
	5	25.02	157.00	1.30
	6	24.82	157.00	1.31
	7	25.03	157.00	1.32
	8	25.00	157.00	1.35
	Average	24.96	157.00	1.32
	Std. Dev.	0.08	0.00	0.02

As a final step before the testing, white spray paint is applied to the bright surfaces of the specimens to suppress the transparency of the laminates. Then, two black dots are marked horizontally and vertically to determine the axial and transverse gage sections of the specimens for the video extensometer to use them for axial and transverse strain measurements.

4.3. Acoustic Emission

Acoustic emission (AE) monitoring is a useful process to detect and classify damage within a laminate. An acoustic emission signal is an ultrasonic wave emerging from a rapid energy release when damage occurs. These waves are detected by highly sensitive sensors and converted into electrical signals. The signals are amplified and transmitted to the data acquisition software. The software records these signals in real-time with their several characteristics such as time, amplitude and frequency. These data are evaluated to correlate the damage signals with a specific type of failure mode. A schematic view representing damage detection with AE method is given in Figure 4.1. Definitions of AE parameters shown in Figure 4.1 are briefly given in Table 4.5.

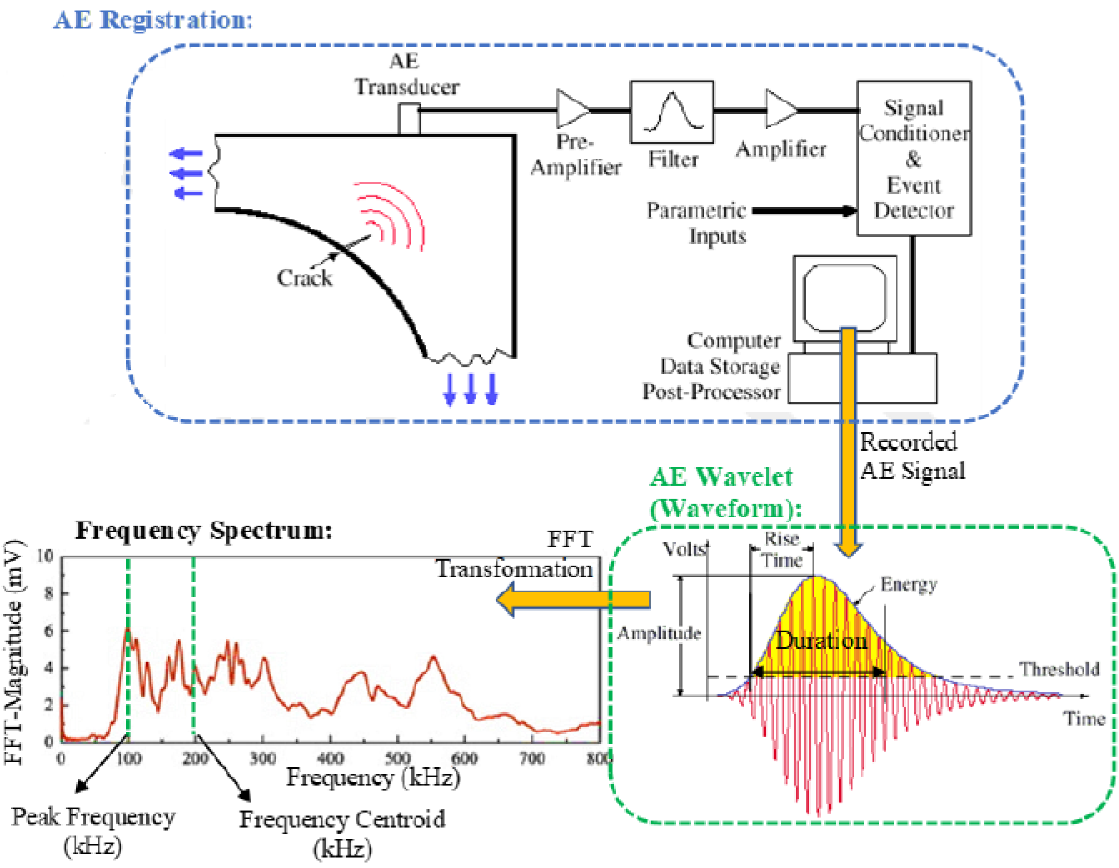

Figure 4.1. A schematic view of damage detection with AE system [52].

Table 4.5. Definitions of AE parameters [52].

AE Parameter	Definition	Unit
Amplitude (A)	Greatestvoltage in a waveform.	dB
Rise time (R)	Time interval between the first threshold crossing and the signal peak.	µs
Duration (D)	Time difference between the first and last threshold crossings.	µs
Energy (E)	Measure of the area under the envelope of the rectified linear voltage time signal from the transducer.	aJ
Peak Frequency (P-FRQ)	Frequency value corresponds to maximum FFT magnitude.	kHz
Frequency Centroid (FRQ-C)	Weighted frequency average.	kHz
Weighted Frequency (WF)	Geometric mean of peak frequency and frequency centroid.	kHz
Rise Amplitude (RA)	Shows reciprocal of gradient in AE signal waveform.	-

In this study, AE data acquisition is performed by two-channel MISTRAS AE node system and AEwin^{TM} software. Two PKWDI sensors with 200-850 kHz operating frequency range are used for signal detection [51]. The integrated amplifier is set to 26 dB. A frequency range of 20 kHz-1 MHz is selected for data acquisition to register possible damage events in a wide range. Peak definition time, hit definition time and hit lockout time are selected as 50, 100 and 300 µs, respectively. 55 dB is set as the threshold value to filter the noises during the test. In addition, a second noise filtering is applied during the post-process. If the time of arrival to both sensors is greater than 1 ms for a signal, then this signal is considered as noise and eliminated. In this way, only the signals registered by both sensors are kept and evaluated.

4.4. Tension Tests

Tension tests are performed with a computer-controlled servo-hydraulic Instron 8801 test machine, having 100 kN load cell. The system is powered by an integrated hydraulic power unit INSTRON 3520 with a running pressure of 207 bars. The complete test setup is shown in Figure 4.2. Bluehill 3.0 software is used to control test parameters. Video extensometer is used to measure deformation in the axial and transverse directions. Before starting the test, the thickness, the width and the length of the specimen are entered to the program. After starting the test, the program collects the real-time data such as load, displacement, stress, mechanical strain and video strain. Displacement-controlled loading is performed on each specimen until failure and at least five specimens are tested from each group. While the rate of loading is 1 mm/min for quasi-isotropic and cross-ply specimens, the rate is increased to 2 mm/min for angle-ply symmetric specimens to reduce the test duration due to excessive elongation of the specimens. While test standard ASTM D3039 [53] is followed for quasi-isotropic and cross-ply specimens, ASTM D3518 [54] is followed for angle-ply specimens.

Tension specimens are attached to the grips of the testing equipment from the tabs at both ends of the specimens. The specimens are positioned in the testing equipment so that the tabs completely remain in the grips. The alignment of the specimens is done properly in order to avoid unwanted bending effects due to misalignment. After the specimen is placed between the grips of the testing equipment, the acoustic emission sensors are clamped on the surface of the specimen (Figure 4.3). Before clamping the sensors, ultrasonic gel is applied to the sensor's surface contacting with the specimen to reduce losses in the signal. For the sake of consistency between the tests, the sensors are clamped close to the ends of the specimens 30 mm away from the tabs in all tests.

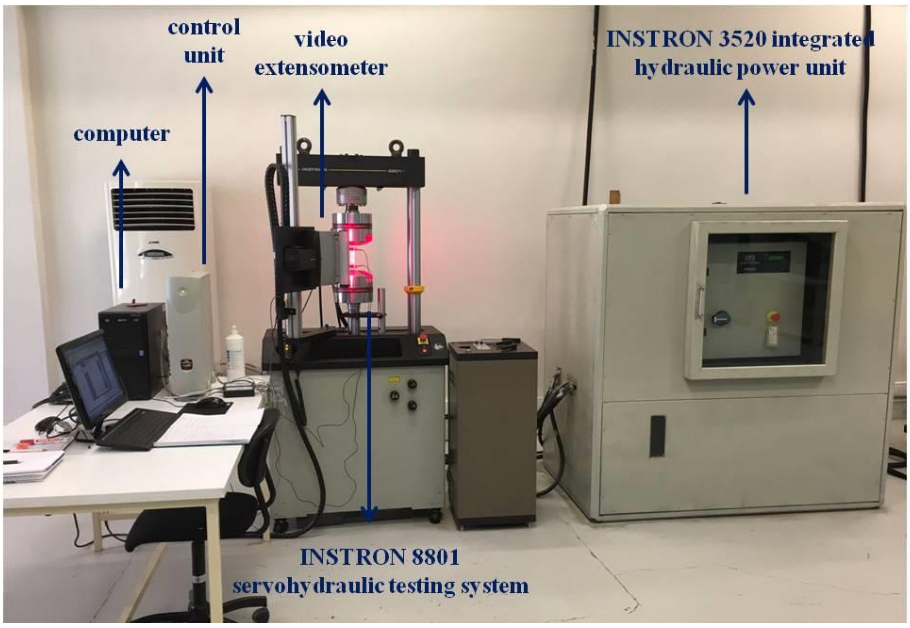

Figure 4.2. Complete test setup.

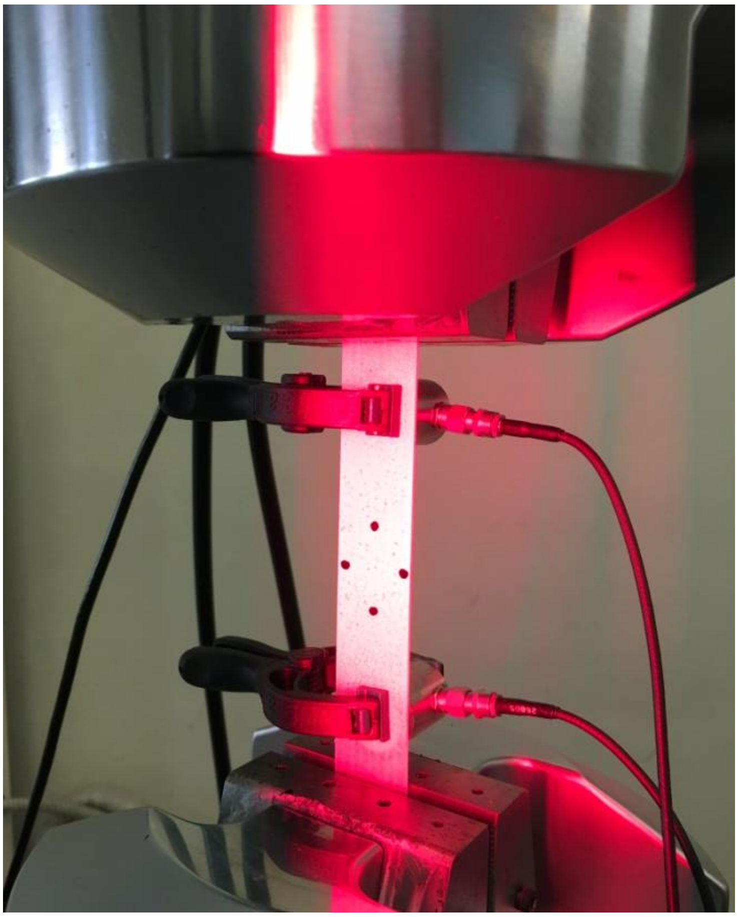

Figure 4.3. Properly placed specimen.

The strain of the specimen is measured by a video extensometer. The device measures the strain from the changes of the distances between two points in both horizontal and vertical directions. This method of strain measurement is more reliable than the mechanical measurement performed by the testing equipment since it directly gets the strain data from the four points at the middle of the specimen rather than hydraulic grip movement at the end of the specimen.

4.5. Tension Test Results

4.5.1. Quasi-isotropic $[0/45/-45/90]_s$ Specimens

Figure 4.4 shows the load-strain curves for five quasi-isotropic specimens, $[0/45/-45/90]_s$, as well as absolute energy levels together with peak frequency distribution. The peak frequency, cumulative counts and absolute energy data obtained using AE equipment are matched with axial strain data based on the time scale. The cumulative number of hits and absolute energy parameters are scaled appropriately just to fit the graph considering that damage assessment is made on the variation in the values of these parameters not their absolute magnitudes.

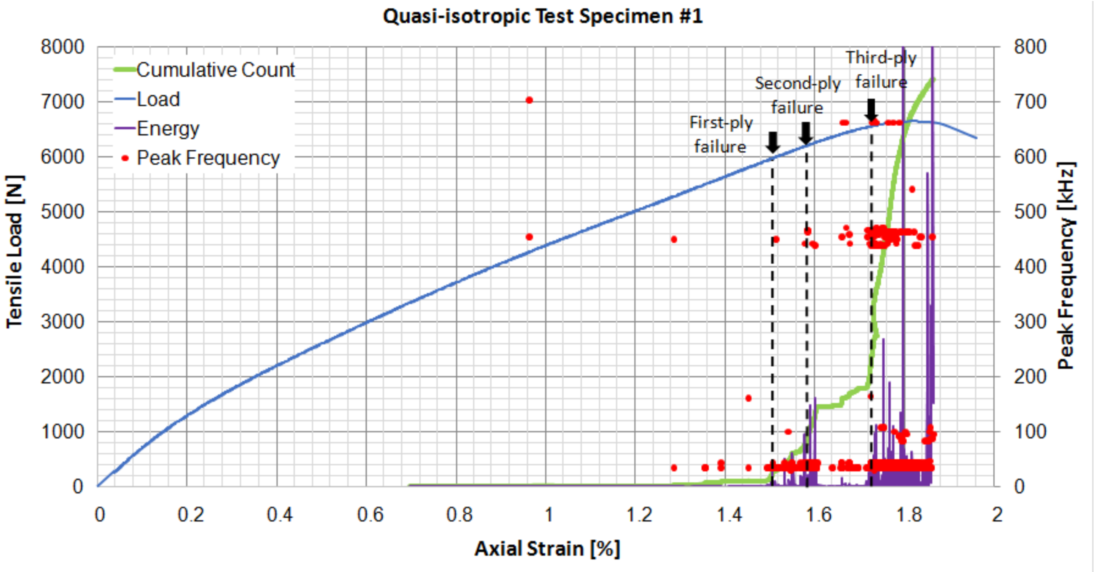

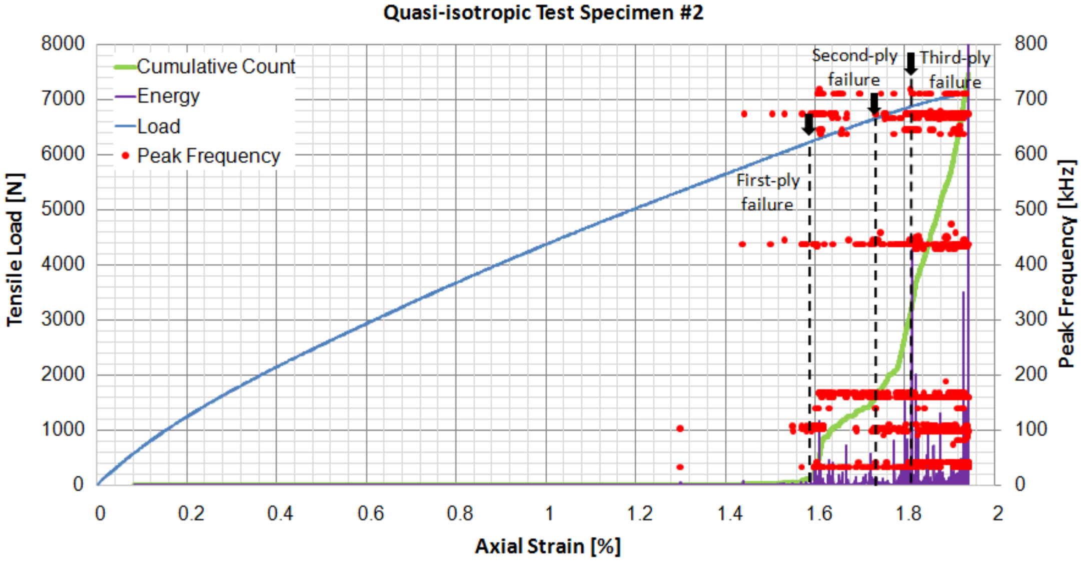
Quasi-isotropic Test Specimen #2
Cumulative Count
Energy
Load
Peak Frequency
Tensile Load [N]
Peak Frequency [kHz]
Axial Strain [%]
First-ply failure
Second-ply failure
Third-ply failure
0
1000
2000
3000
4000
5000
6000
7000
8000
100
200
300
400
500
600
700
800
0.2
0.4
0.6
0.8
1
1.2
1.4
1.6
1.8
2

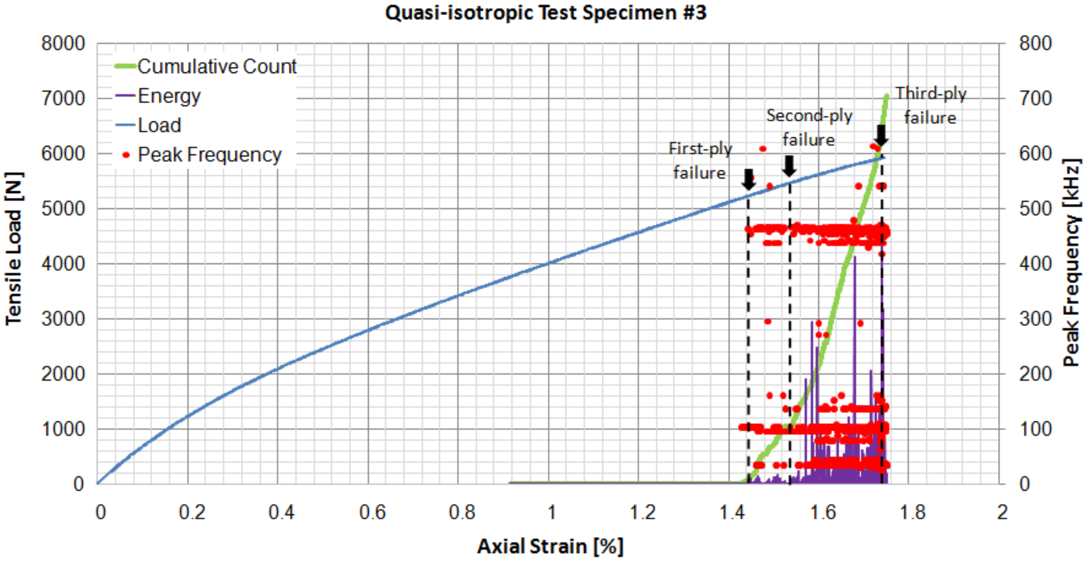
Quasi-isotropic Test Specimen #3
Cumulative Count
Energy
Load
Peak Frequency
Tensile Load [N]
Peak Frequency [kHz]
Axial Strain [%]
First-ply failure
Second-ply failure
Third-ply failure
0
1000
2000
3000
4000
5000
6000
7000
8000
100
200
300
400
500
600
700
800
0.2
0.4
0.6
0.8
1
1.2
1.4
1.6
1.8
2

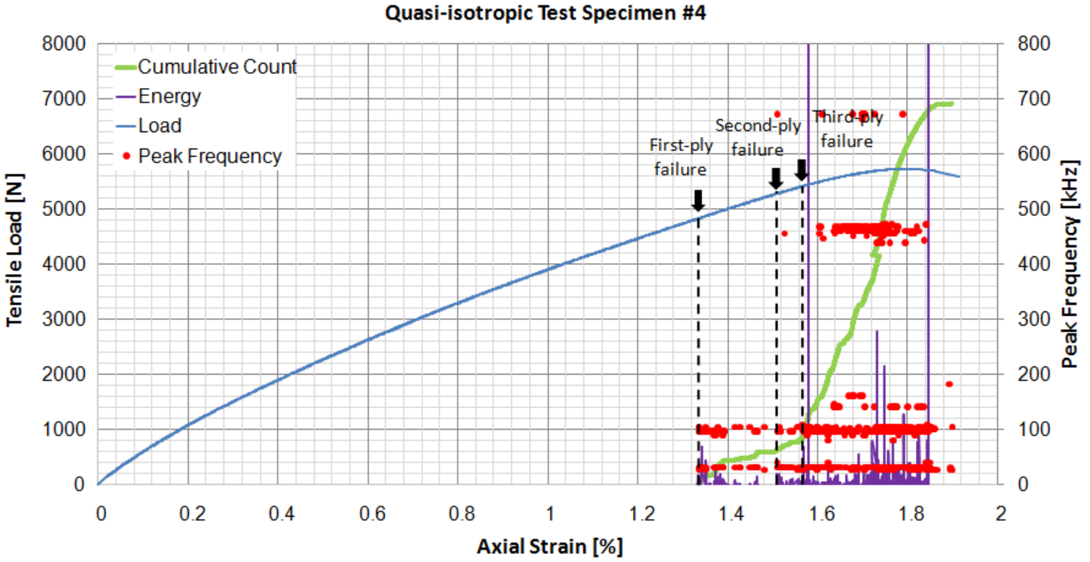
Quasi-isotropic Test Specimen #4
Cumulative Count
Energy
Load
Peak Frequency
Tensile Load [N]
Peak Frequency [kHz]
Axial Strain [%]
First-ply failure
Second-ply failure
Third-ply failure
0
1000
2000
3000
4000
5000
6000
7000
8000
100
200
300
400
500
600
700
800
0.2
0.4
0.6
0.8
1
1.2
1.4
1.6
1.8
2

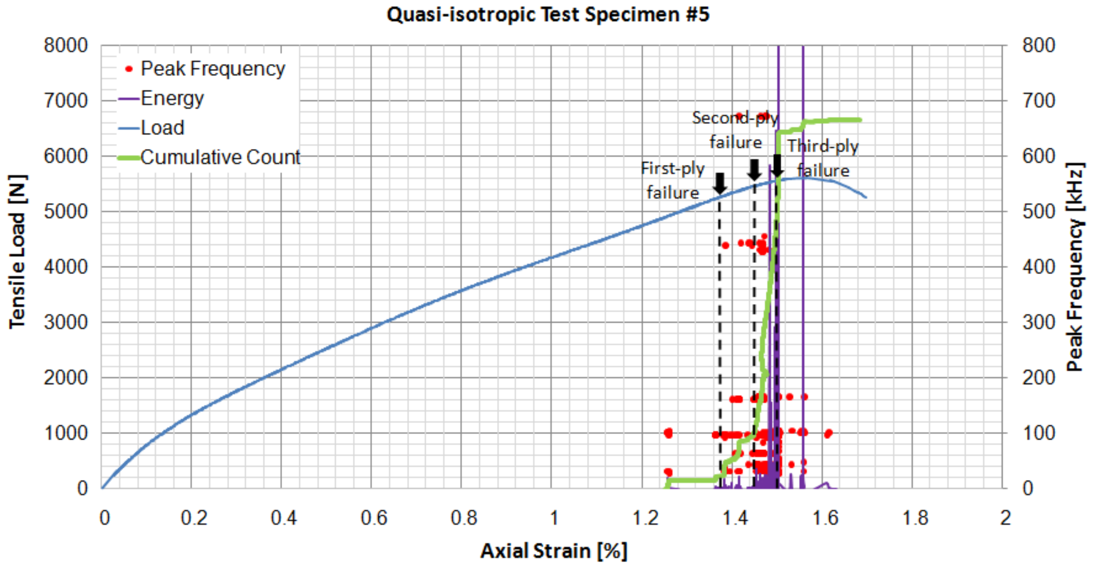

Figure 4.4. Peak frequency distribution, absolute energy levels, number of AE hits and load vs. strain curve for quasi-isotropic laminates with sequence $[0/45/-45/90]_S$.

Five quasi-isotropic specimens are subjected to tension test to determine the mechanical response of the material. Load vs. strain curves for five quasi-isotropic specimens are shown in Figure 4.5. Specimen 1, 2, 3, 4 and 5 fail when the strain reaches 1,96%, 1,94%, 1,75%, 1,91%, and 1.70%, respectively. For specimen 2 and 3, stiffness of the specimens does not show a remarkable change and these specimen suddenly fracture. However, the load bearing capacity of the specimens 1, 4 and 5 considerably reduces after reaching the maximum load before fracture.

As seen in Figure 4.4, few AE hits are detected before first-ply failure occurs in the quasi-isotropic specimens. These early signals are not interpreted as damage because of the absence of consistent hits. Besides, energy levels of these signals are low. They may be the result of noises or micro-cracks. Some local damage not propagating in the ply is not considered as a failure. The first-ply failure is determined as the point where the number of hits increases rapidly and consistent signals are received from at least one frequency band. The first-ply failure occurs at 1.50%, 1.59%, 1.44%, 1.33%, and 1.37% strain levels for the specimen 1, 2, 3, 4 and 5, respectively. After the first-ply failure, the frequency bands between 20 and 160 kHz are formed commonly for all specimens. In the studies presented by Aramugam *et al*. [55] and Fotouhi *et al*. [56], the peak frequency bands of 90-110 kHz and 100-190 kHz were associated with matrix cracking in the glass-epoxy laminates similar to this study, respectively. Therefore, it is assumed that this low-frequency band is related to the transverse matrix cracking developed in 90° plies. Following the first-ply failure, the slope of the load-strain curves gradually decreases and the slope of the cumulative-count curves rapidly increases. In addition, energy level of the signals become noticeable. These remarkable changes in these two curves and the energy levels can be associated with substantial damage progression in the 90° plies. For specimen 2, frequency bands of 400-500 kHz and 600-750 kHz also develop at the first-ply failure. For specimen 3, the frequency band 600-750 kHz is not activated and for specimen 1 and 4, only 20-180 kHz frequency band is activated following the first-ply failure.

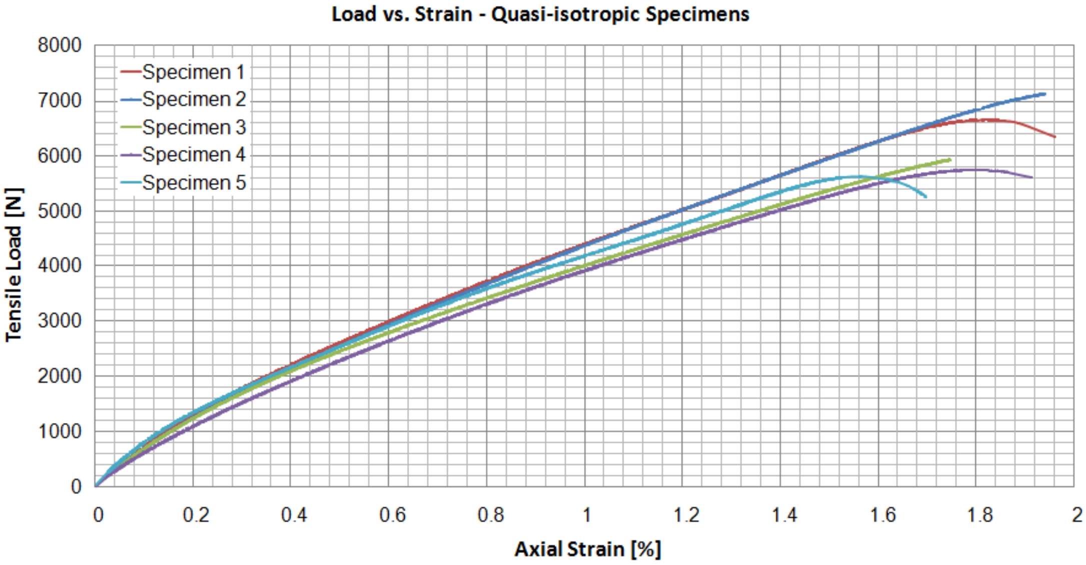

Figure 4.5. Load vs. strain behavior of the cross-ply specimens with sequence [0/45/-45/90]$_s$.

The second-ply failure is assumed to occur when the slope of the cumulative-count curve changes significantly for all specimens. For specimen 1, the frequency band of 400-500 kHz is formed following the second-ply failure. For specimen 2 and 3, since the frequency band 400-500 kHz is already activated at the first-ply failure, the number of hits received from this band increases after the second-ply failure. The persistent hits from 600-750 kHz band are observed only in specimen 2 after the second-ply failure. For specimen 4, the second-ply failure is determined as the point where the density of the signals from 20-180 kHz band increases. There are almost no high frequency signals from 600-750 kHz band after the second-ply failure for specimens 3, 4 and 5.

The third-ply failure is recognized with the change in the cumulative-count curves and increase in the density of the hits received from certain frequency bands in all specimens. For specimen 1 and 4, the frequency band of 400-500 kHz is formed following the third-ply failure. In specimen 1, few signals from 600-700 kHz are also observed after the third-ply failure. The densities of the hits registered from 400-500 kHz and 600-700 kHz bands band increase for specimen 2. For specimen 3, the third-ply failure occurs with fracture. The main failure mechanisms remain in 20-180 kHz and 400-500 kHz for specimens 3, 4 and 5. Therefore, the cumulative-count increases just in these two bands. Up to the first-ply failure, stiffness of the specimens remains constant; however the stiffness gradually decreases due to the damage progression in the material and eventual ply failures. After the third-ply failure, the material significantly loses its load bearing capacity and ultimate failure follows quickly.

The mechanical properties of the quasi-isotropic specimens are listed in Table 4.6.

Table 4.6. Mechanical properties of the quasi-isotropic specimens.

Specimen	Elastic modulus [GPa]	Max. tensile stress [MPa]	Max. axial strain [%]	1st ply failure [kN]	2nd ply failure [kN]	3rd ply failure [kN]
1	16.20	222.71	1.96	5.95	6.20	6.50
2	16.99	240.16	1.94	6.20	6.60	6.85
3	16.86	212.99	1.75	5.25	5.50	5.90
4	15.34	202.00	1.91	4.85	5.30	5.40
5	14.83	192.61	1.70	5.30	5.45	5.55
Average	16.04	214.09	1.85	5.51	5.81	6.04
Std. dev.	0.94	18.46	0.12	0.55	0.56	0.62

4.5.2. Cross-ply $[0/90]_{2s}$ Specimens

Figure 4.6 shows the load-strain curves for six cross-ply specimens, $[0/90]_{2s}$, as well as absolute energy levels together with peak frequency distribution.

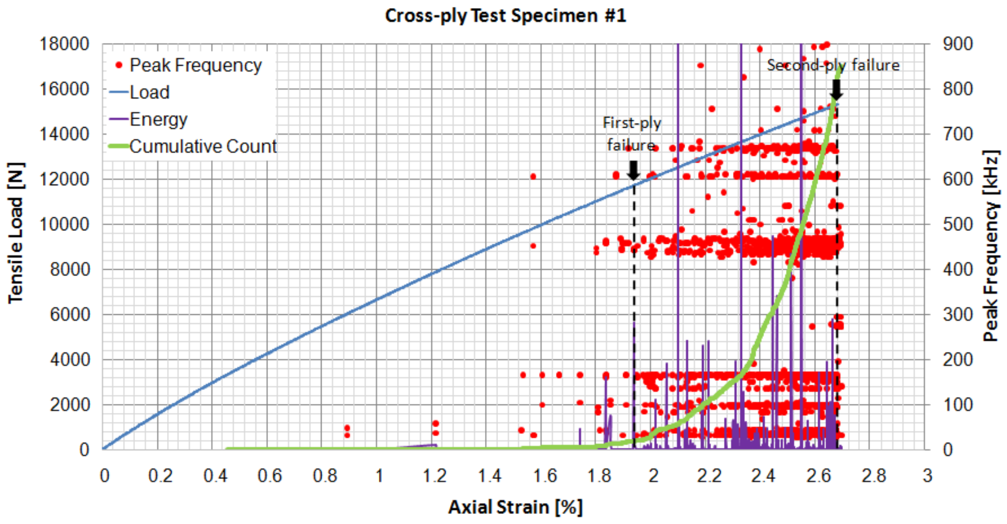
Cross-ply Test Specimen #1
Peak Frequency
Load
Energy
Cumulative Count
First-ply failure
Second-ply failure
Tensile Load [N]
0
2000
4000
6000
8000
10000
12000
14000
16000
18000
Peak Frequency [kHz]
0
100
200
300
400
500
600
700
800
900
Axial Strain [%]
0
0.2
0.4
0.6
0.8
1
1.2
1.4
1.6
1.8
2
2.2
2.4
2.6
2.8
3

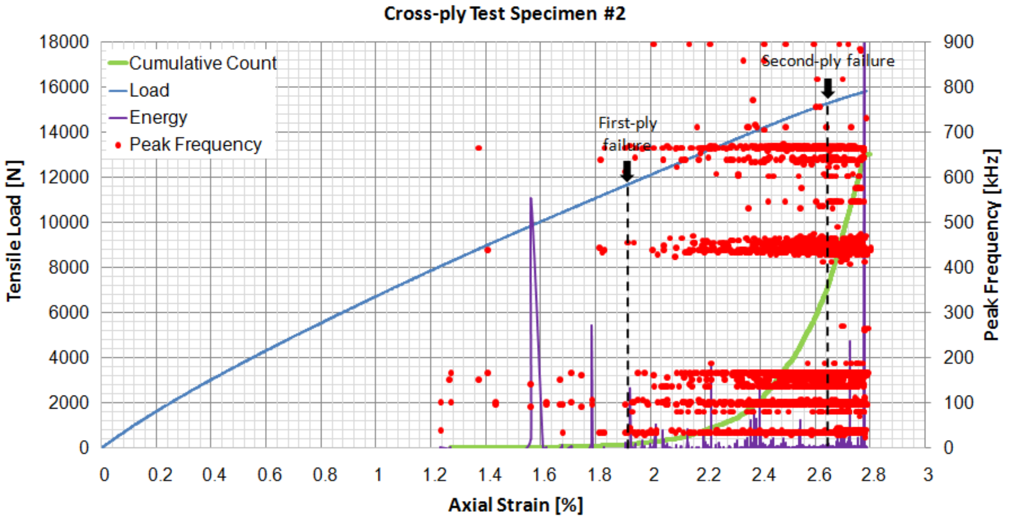
Cross-ply Test Specimen #2
Cumulative Count
Load
Energy
Peak Frequency
First-ply failure
Second-ply failure
Tensile Load [N]
0
2000
4000
6000
8000
10000
12000
14000
16000
18000
Peak Frequency [kHz]
0
100
200
300
400
500
600
700
800
900
Axial Strain [%]
0
0.2
0.4
0.6
0.8
1
1.2
1.4
1.6
1.8
2
2.2
2.4
2.6
2.8
3

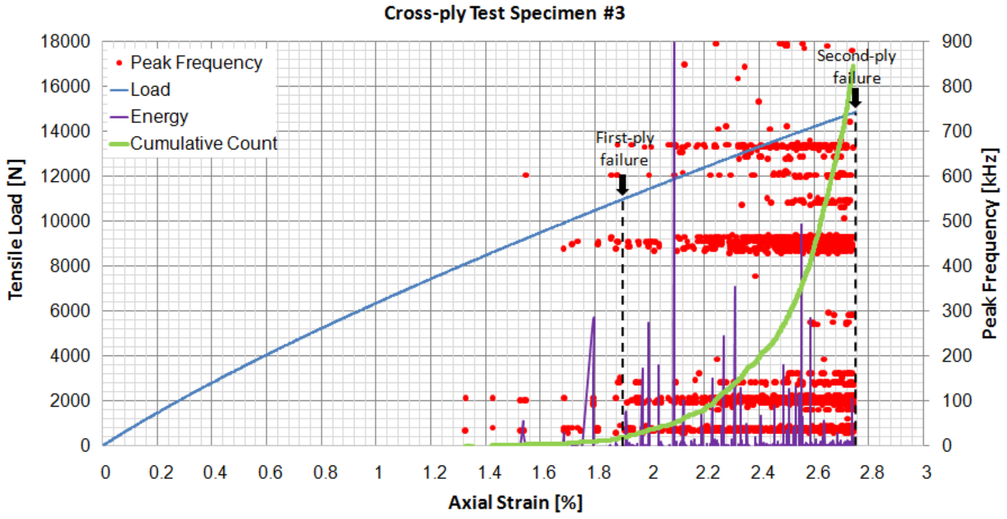
Cross-ply Test Specimen #3
Peak Frequency
Load
Energy
Cumulative Count
First-ply failure
Second-ply failure
Tensile Load [N]
0
2000
4000
6000
8000
10000
12000
14000
16000
18000
Peak Frequency [kHz]
0
100
200
300
400
500
600
700
800
900
Axial Strain [%]
0
0.2
0.4
0.6
0.8
1
1.2
1.4
1.6
1.8
2
2.2
2.4
2.6
2.8
3

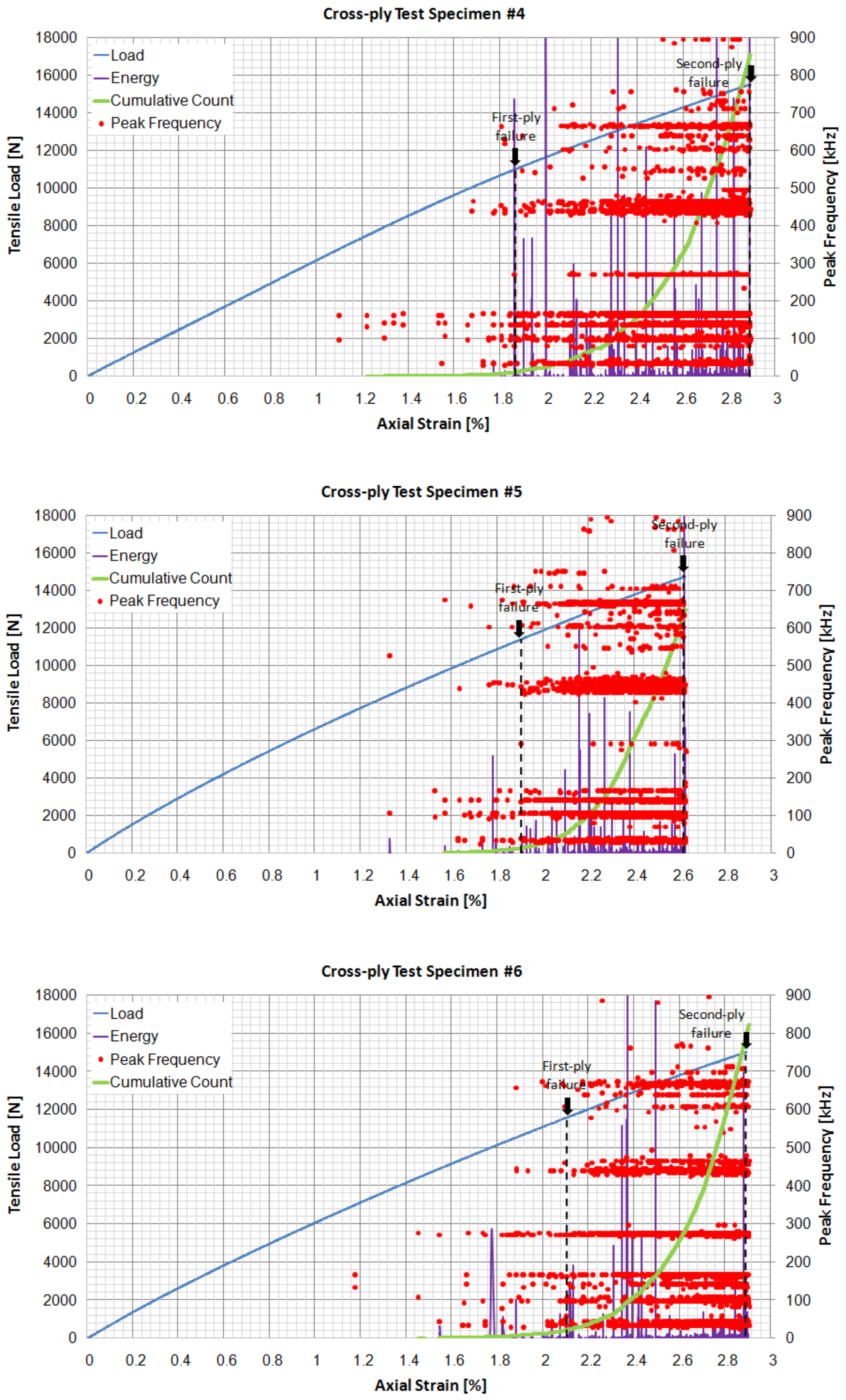

Figure 4.6. Peak frequency distribution, the absolute energy levels, the number of AE hits and the stress strain for cross-ply laminates with sequence $[0/90]_{2s}$.

Six cross-ply specimens are subjected to tension test to determine the mechanical response of the material. Load vs. strain curves for six cross-ply specimens are shown in Figure 4.7. The load of the cross-ply specimens increases almost linearly up to fracture. The cross-ply specimens fail when the strain reaches 2.60-2.90% range and the fracture loads are in the range of 15-16 kN. The load bearing capacity of the cross-ply specimens are comparably higher than the quasi-isotropic specimens due to the number of plies aligned in the loading direction. While two layers are aligned in the loading direction for quasi-isotropic sequence, there are four 0° layers in the cross-ply sequence. The damage gradually developing in 0° plies during the loading does not reduce the stiffness of the cross-ply specimens significantly. However, the cumulated damage in the material eventually leads to a sudden fracture.

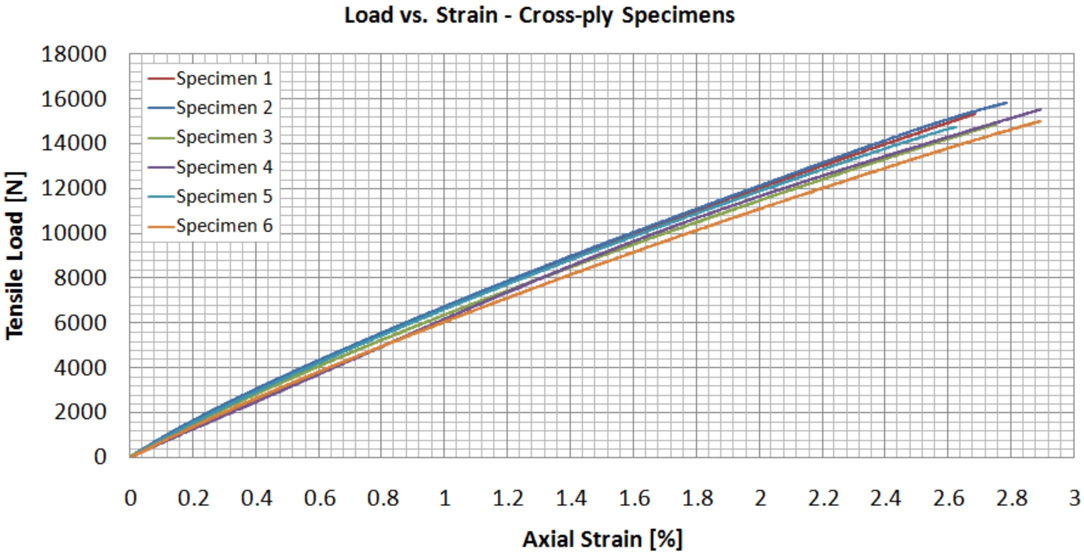

Figure 4.7.Load vs. strain behavior of cross-ply specimens with seqeunce $[0/90]_{2s}$.

The AE sensors start to detect signals from 20-180 kHz frequency band as early as 1.25% strain level, however the number of hits and energy of the signals are quite low, these signals may be attributed to micro-cracks rather than macro-damage occurred in the material. As the strain level reaches to 1.85-1.95% range except specimen 6, the number of hits starts to ramp up and signals are registered from multiple frequency bands. The first-ply failure load is assumed as the point where the slope of the cumulative-count curves increase significantly and the AE sensors start to receive persistent signals from 20-180, 400-600 and 600-750 kHz frequency bands. As the strain increases, the intensity of the signals from all frequency bands increases. At the strain level of 2.25-2.50%, the high energy peaks and rise of the cumulative-count curve are observed. Also, the density of the signals from 700-800 kHz frequency band is activated. Since there is no significant change in the stiffness of all specimens, these high energy signals may be attributed to the delaminations at the interface between 0° plies and 90° plies. Additionally, the third-ply failure is assumed as the point where the ultimate fracture occurs for all specimens except specimen 2 due to no significant change in the cumulative-count slope and no formation of new frequency bands. In specimen 2, the third-ply failure is assumed to occur at the point where the density of the signals from 600-700 kHz frequency band increases. The ultimate failure is assumed due to the fiber breakage in 0° plies and loss of load bearing capacity.

The mechanical properties of the cross-ply specimens are listed in Table 4.7.

Table 4.7. Mechanical properties of the cross-ply specimens.

Specimen	Elastic modulus [GPa]	Max. tensile stress [MPa]	Max. axial strain [%]	1st ply failure [kN]	2nd ply failure [kN]
1	22.805	481.31	2.68	11.80	15.40
2	22.661	482.81	2.78	11.90	15.50
3	21.877	470.80	2.75	11.20	15.00
4	18.244	463.99	2.89	11.20	15.70
5	21.668	446.24	2.62	11.60	15.00
6	21.034	488.56	2.90	11.80	15.20
Average	21.38	472.29	2.77	11.58	15.30
Std. Dev.	1.67	15.53	0.11	0.31	0.28

4.5.3. Classification of Failure Modes

ASTM D3039, Standard Test Method for Tensile Properties of Polymer Matrix Composite Materials, categorizes failure modes based on the failure type, failure area and failure location. Each of these three features is designated by a letter. The first, second and third letter designate failure type, failure area and failure location, respectively. Figure 4.8 shows the classification of failure modes.

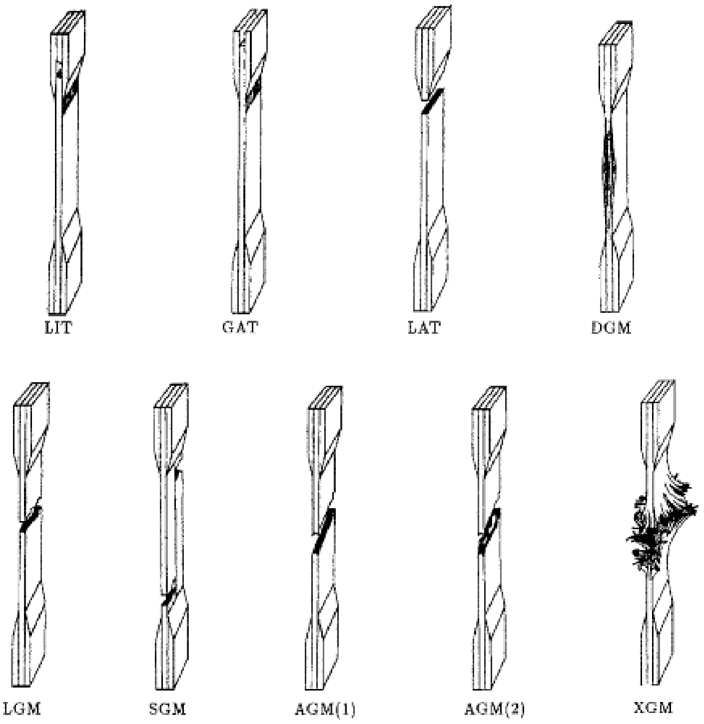

First Character

Failure Type	Code
Angled	A
edge Delamination	D
Grip/tab	G
Lateral	L
Multi-mode	M(xyz)
long. Splitting	S
eXplosive	X
Other	O

Second Character

Failure Area	Code
Inside grip/tab	I
At grip/tab	A
<1W from grip/tab	W
Gage	G
Multiple areas	M
Various	V
Unknown	U

Third Character

Failure Location	Code
Bottom	B
Top	T
Left	L
Right	R
Middle	M
Various	V
Unknown	U

Figure 4.8. The classification of failure modes.

Figure 4.9(a) shows the failed quasi-isotropic specimens numbered as 1, 2, 3, 4 and 5 from left to right, respectively. Figure 4.9(b) shows the failed cross-ply specimens numbered as 1, 2, 4, 5, 6 and 3 from left to right, respectively. Figure 4.9(c) shows the failed angle-ply symmetric specimens numbered as 1, 2, 6, 7 and 8 from left to right, respectively. Failure modes of the quasi-isotropic specimens 1, 2, 4 and 5 and cross-ply specimens 2, 3, 4, 5 and 6 are LGM. L indicates lateral for the failure type, G indicates gage for the failure area and M indicates middle for the failure location. Failure mode of the quasi-isotropic specimen 3, cross-ply specimen 1 and all angle-ply symmetric specimens are AGM. A indicates angled for the failure type.

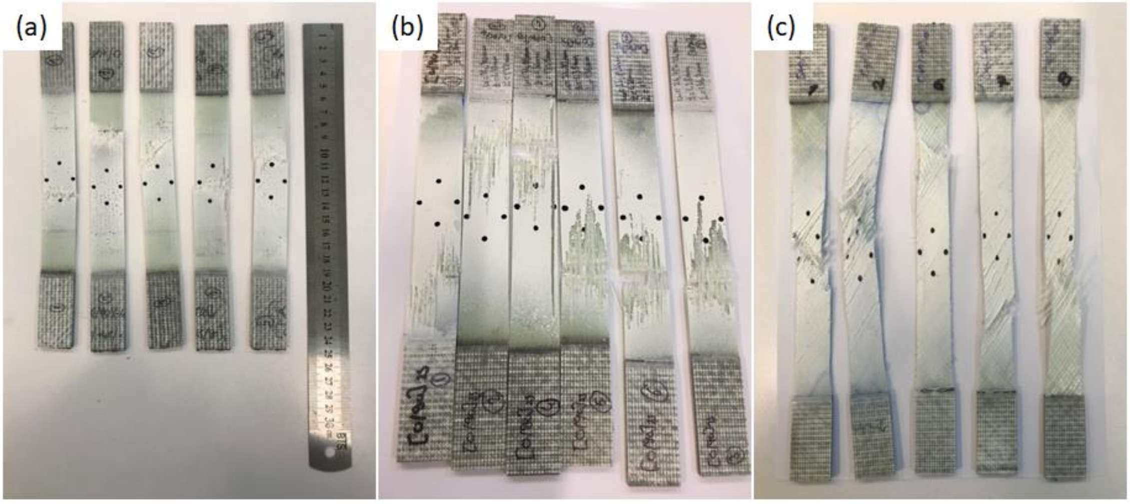

Figure 4.9. Failed (a) quasi-isotropic, (b) cross-ply, (c) angle-ply symmetric specimens.

4.6. Estimation of Material Properties

Because the fibers in the individual plies of the non-crimped fabric are stitched together, it is not possible to determine the stiffness and strength of a single ply in the fiber direction or transverse to it directly by experimental methods. For this reason, a progressive damage model [57] based on the classical lamination theory (CLT) and the maximum stress failure theory is used to determine the strength properties of E-glass-epoxy lamina. Figure 4.10 shows a comparison between the experimental load-strain curves of cross-ply and quasi-isotropic tension test specimens and the curves predicted by the progressive model using the stiffness properties in Table 4.5. The values in the table for E_1, E_2, and G_{12} are obtained by an iterative optimization algorithm so that the predicted load-strain line for the quasi-isotropic specimens provides the best fit to the experimentally obtained curves. ν_{12} is obtained using the rule of mixture formulation of micromechanics. The mechanical properties used in the calculation are given in Table 4.2 and Table 4.3 for the fiber and matrix materials, respectively. The load-strain curves of the model nearly coincide with the first linear section of the experimental curve. This coincidence shows that the stiffness values of unidirectional lamina given in Table 4.8 provide an acceptable fit. The experimental results of cross-ply specimens are considered in evaluating stiffness and strength properties, because the sandwich specimens contain only quasi-isotropic layers. However, comparison between the predicted load-strain curve of cross-ply specimens and the experimental one is shown in the figures.

Table 4.8. Stiffness properties for the unidirectional E-glass-epoxy lamina.

E_1, longitudinal elastic modulus [GPa]	29.20
E_2, transverse elastic modulus [GPa]	4.62
ν_{12}, in-plane Poisson’s ratio	0.40
G_{12}, shear modulus [GPa]	2.40

The mechanical properties of the tension test specimens are estimated by the progressive damage model by assuming that the ply-failures occur suddenly with significant loss of load bearing capability of the failed lamina. Therefore, the load-strain curve of the model is piecewise linear with sudden fall in load level. However, total failure of a ply actually does not occur suddenly and the damage in the specimens develops progressively as can be seen from the experimentally obtained curves in Figure 4.10. The slopes of the experimental load-strain curves continuously decrease with increased strain. This gradual decrease points that damage in a ply develops progressively and causing progressive reduction in stiffness. On the other hand, the model uses maximum stress theory, which ignores the interactive intralaminar failure mechanisms and progression of damage. However, the resulting error is not significant from the engineering stand point.

As mentioned before, ply-failure load levels are determined based on the AE data. First-ply-failure of the quasi-isotropic specimen with $[0/45/-45/90]_s$ stacking sequence occurs at 5.5 kN on the average due to matrix failure in 90° plies. The normal stress transverse to the fibers in the failed layers is calculated as 57 MPa based on CLT. Therefore, the transverse tensile strength, Y_t, is taken as 57 MPa. After the 90° plies failed, the stiffness properties transverse to the fibers, E_2, ν_{12}, ν_{21}, and G_{12}, are reduced in these plies by multiplying their values given in Table 4.5 by a degradation factor, d_m; so their subsequent values after 90° plies failed are $d_m E_2$, $d_m \nu_{12}$, $d_m \nu_{21}$, and $d_m G_{12}$. The fibers are assumed undamaged. The value of $d_m$is selected as 0.1 so that the slope of the analytical curve would be closer as much as possible to the experimental curve at this load level. The second-ply failure in the quasi-isotropic specimen occurs due to shear failure in 45° plies at 5.8 kN. The shear stress in these plies in the principal material coordinates is calculated to be 47 MPa. Therefore, shear strength, S, is taken as 47 MPa. Again, the stiffness properties mostly affected by the matrix, E_2, ν_{12}, ν_{21}, and G_{12} are reduced by taking the value of the degradation factor, d_m, as 0.6. The third-ply failure occurs at 6.10

kN due to fiber failure in 0° plies. Normal stress along the fiber direction in 0° plies calculated with the reduced stiffness values for 90° and 45° plies is 506 MPa. Therefore, the longitudinal tensile strength, X_t, is taken as 506 MPa.

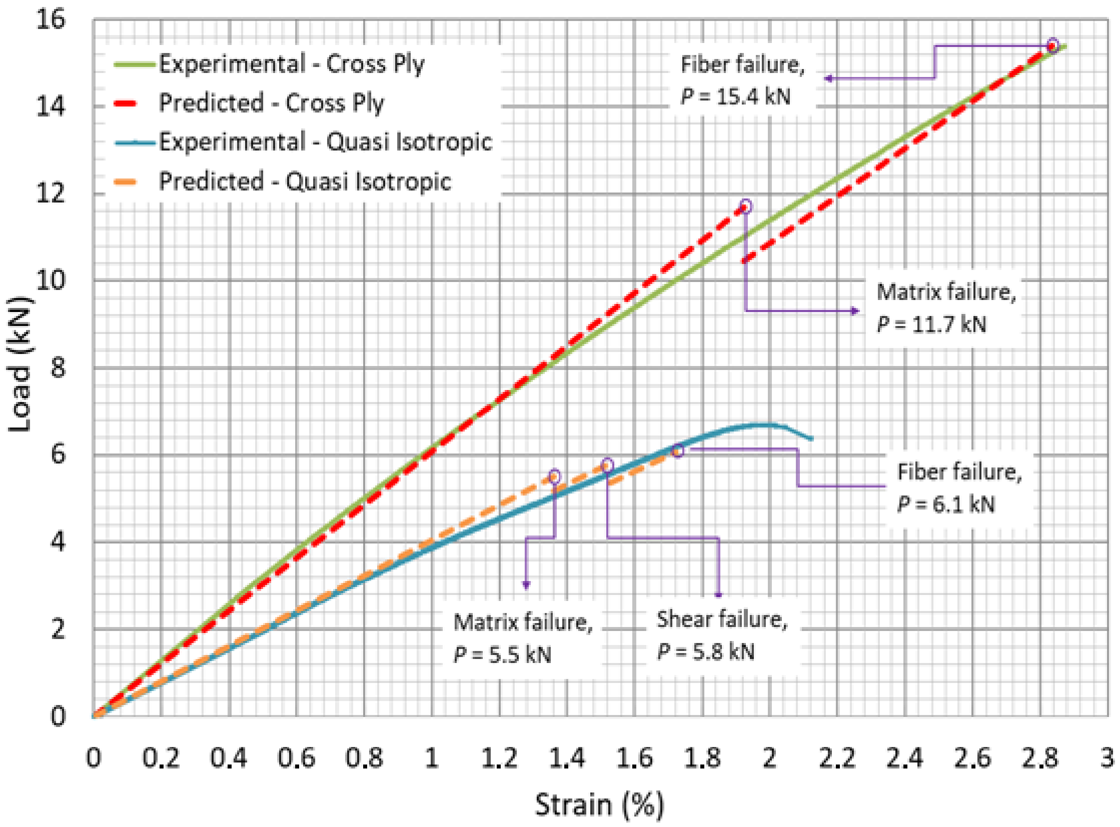

Figure 4.10. Experimental load-strain curves of tension test specimens with quasi-isotropic, [0/45/-45/90]$_s$, and cross-ply, [0/90]$_{2s}$, stacking sequences and the curves proposed by the progressive damage model.

Considering that the initial failure of sandwich specimens are observed to develop due to tensile stresses, tests are not performed to find the compressive strength properties of the material; however, their values are estimated based on the information given in the literature. For the compressive strength in the transverse direction, the value in the technical data sheet of the resin material is used (see Table 4.9). Resin tensile and compressive strengths were reported to be 70-80 MPa and 120-140 MPa, respectively. Accordingly, Y_c, is taken as -120 MPa. The data sheet also reports that the epoxy reinforced with 16-ply 8H satin woven glass fabric with 43% fiber content has a compressive strength about 10% lower than its tensile strength. The compressive strength value for epoxy-reinforced non-crimp glass fabrics was also reported to be slightly lower than the tensile strength in the literature [58,59]. Accordingly, the longitudinal compressive strength of unidirectional E-glass epoxy laminate, X_c, is taken as -480 MPa. The overall strength properties of unidirectional E-glass epoxy lamina are listed in Table 4.10.

Table 4.9. The strength properties of the neat resin [50].

Flexural strength [MPa]	110-120
Tensile strength [MPa]	70-80
Compressive strength [MPa]	120-140
Elongation of break [%]	5.0-6.5
Impact strength [MPa]	45-55

Table 4.10. Strength properties for the E-glass-epoxy lamina.

X_t, longitudinal tensile strength [MPa]	506
X_c, longitudinal compressive strength [MPa]	-480
Y_t, transverse tensile strength [MPa]	57
Y_c, transverse compressive strength [MPa]	-120
S, shear strength [MPa]	47

5. COMPUTATIONAL WORK

5.1. Finite Element Model of the Three-Point Bending Test

A finite element model (Figure 5.1) representing the physical test setup is developed in ABAQUS to simulate the mechanical behavior of the composite sandwich plate under three-point bending. Besides the full model, a quarter model is developed using the double symmetry in the model in order to reduce computational burden of the optimization studies. The analyses are solved in the explicit solver. A fixed time step of 0.05 is taken as the step size in order to observe the load changes as the displacement increases in small increments.

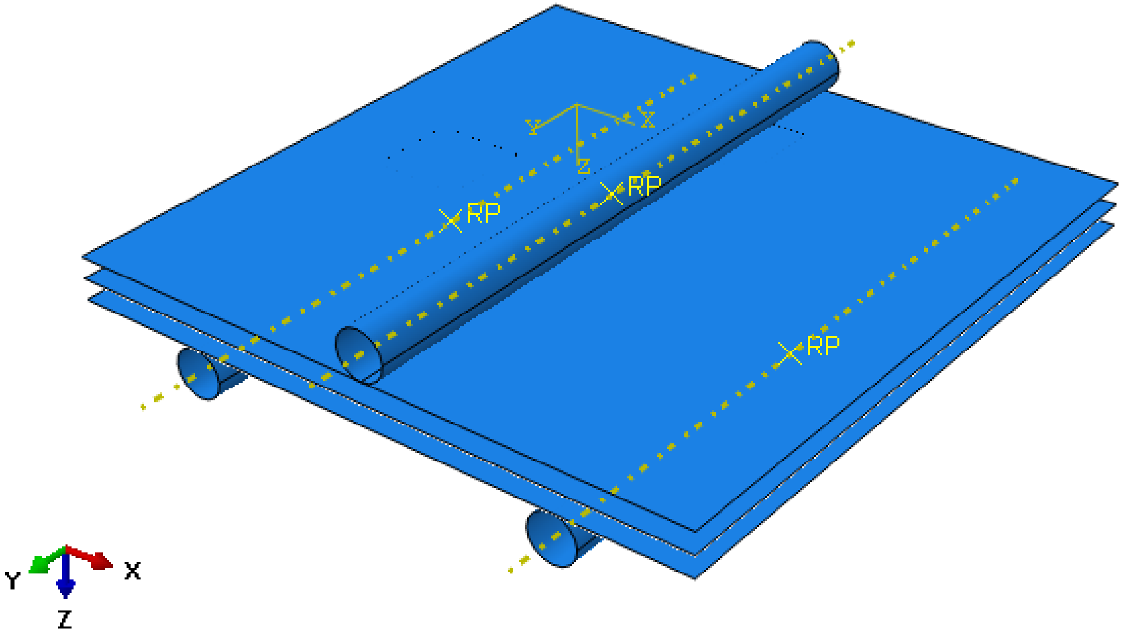

Figure 5.1. The full-scale finite element model representing three-point bending test setup.

The face sheets and the core structure are modeled separately. The quasi-isotropic stacking sequence $[0/45/-45/90]_s$ is defined for the core and the face sheets. Then, all parts are added to the assembly and translated to their exact positions. Considering that, the face sheets and the core are bonded to each other by a quite strong epoxy, the surfaces in contact on the face sheets and the core are simply tied to each other in the model since no slip expected during the loading.

The face sheets and the core are meshed with shell elements. The element type S4R with four nodes is used for the face sheets, whereas S8R with eight nodes are used for the core section due its complex geometry. Both elements have six degrees of freedom: three for translation and three for rotation. First-order shear deformation theory applies for both element types and thus, transverse shear strains are assumed to be constant throughout the thickness.

Finite element algorithms perform numerical calculations at some certain points called integration points to determine the values in each element and interpolate these values to the other points within the element. S4R and S8R elements have reduced integration points. As shown in Figure 5.2, first-order interpolation is performed for four-node elements, while second-order interpolation is performed for eight-node elements [60].

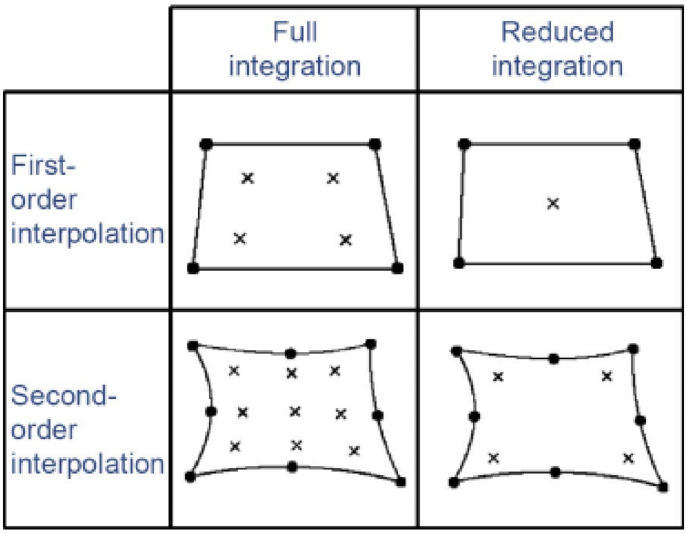

Figure 5.2. The integration type and the order of interpolation [60].

A mesh convergence study is performed with the core section in order to determine the appropriate element size. The analyses are performed for the fixed displacement loading with different element sizes for the core. Considering the results seen in Figure 5.3, the element sizes are selected as 2.5 mm and 5.0 mm for the core and face sheets, respectively.

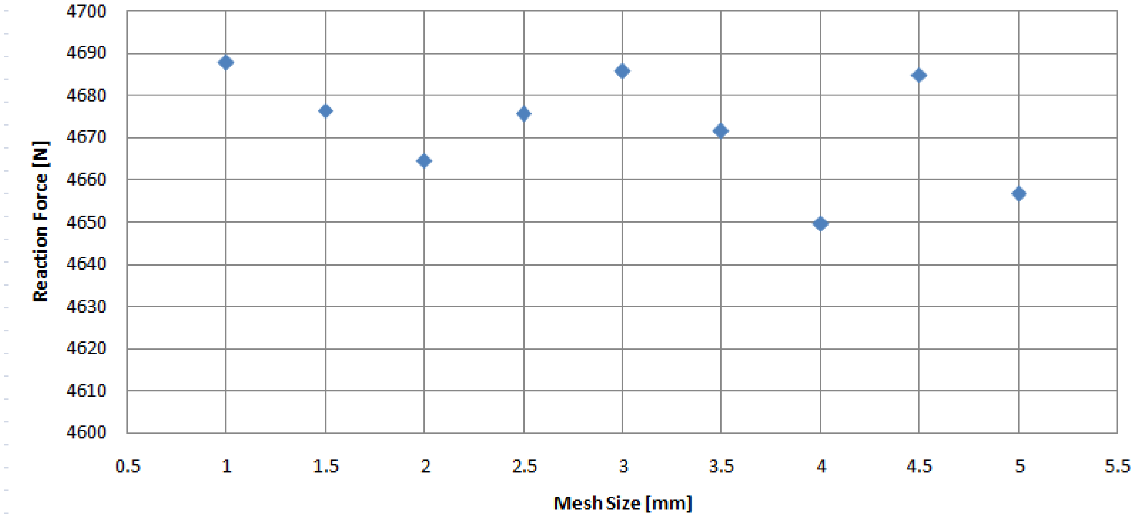

Figure 5.3. Mesh convergence study.

The full model has geometric features similar to that of the specimens used in the experiments conducted by Uzal [30]. Nevertheless, the geometry of the core section is parametrically modelled; its size can easily be changed by modifying the values of the geometric parameters. In this study, the core section of the sandwich plate consists of forty-nine unit cells arranged in a seven-by-seven grid where unit cells are positioned alternately upright and upside-down (Figure 5.4).

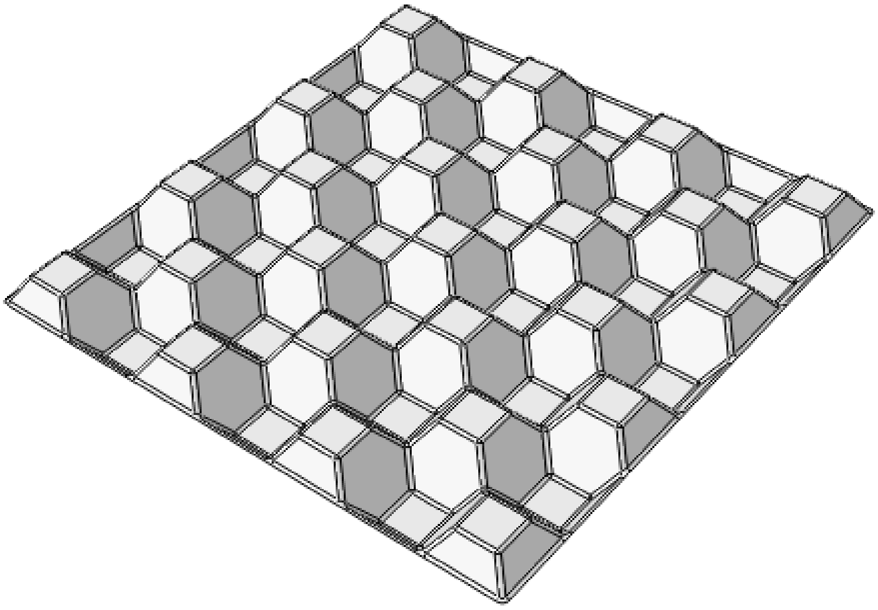

Figure 5.4. The core section of the sandwich plate.

A unit cell has a truncated pyramidal shape with a square top and base having side lengths of L_c and L_b, respectively. The top side length L_c, the angle between the side faces and base area θ, the cell height h, and number of unit cells are defined as individual parameters generating the model (Figure 5.5). Accordingly, the plate size changes as these parameters change. After merging forty-nine unit cells in a seven-by-seven grid, fillets determined parametrically are introduced at all sharp edges. The fillet radius is set to one-tenth of the contact length, which is the edge length of the square region of the core in contact with the face sheets. Two face plates and the core structure have $7L_b \times 7L_b$ dimensions.

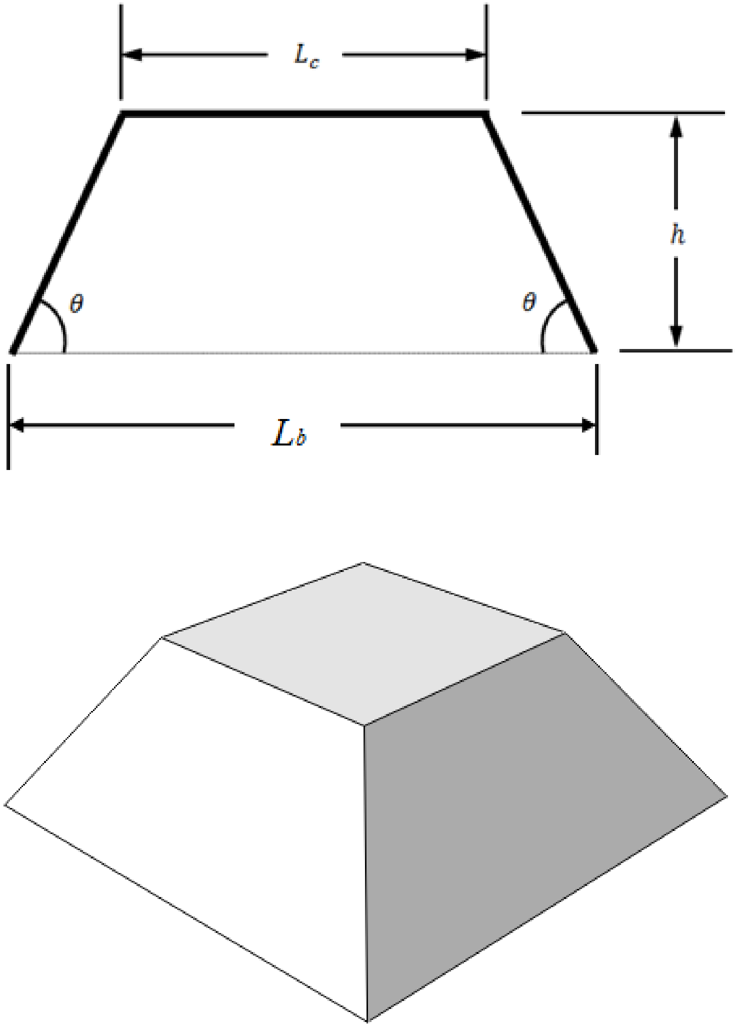

Figure 5.5. The cross-sectional (top) and three dimensional (bottom) geometry of the unit cell.

In the specimens manufactured for this study, the measured thicknesses of the face plates and core section are 1.20 mm and 1.44 mm, respectively. Considering that the laminates contain eight plies, the average ply thickness of the face plates and core section is calculated as $t_f = 0.15$ mm and $t_c = 0.18$ mm, respectively. However, the thickness of the core plies is taken as 0.15 mm in the finite element model, same as the face plates considering that the amount of the reinforcement material in the face plates and the core are the same and the effect of the larger amount of resin in the core on its stiffness and strength is negligible. However, the real thickness of the core plate is reflected in the offset between the finite elements of the core and face plates. Shell elements are generated at the mid-surfaces of the laminates. Accordingly, there is an offset between the mid-planes of the core and the face plates (as shown in Figure 5.6). Since there are four plies between the mid-plane and the outer surfaces of the laminates, the resulting offset, ℓ, is calculated as

$$\ell = 4t_c + 4t_f = 1.32\ mm \tag{5.1}$$

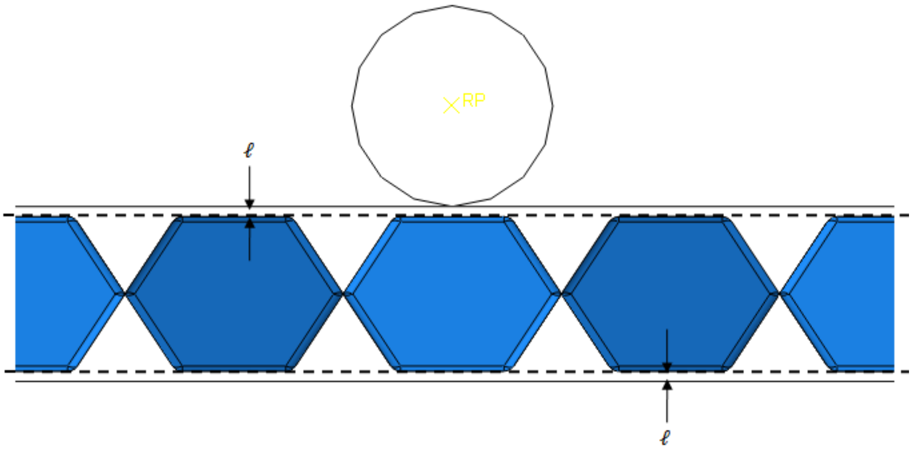

Figure 5.6. The offset defined between the core section and face plates.

The boundary conditions of the model reflect the physical loading conditions of the displacement-controlled three-point bending test. In order to apply the load on the top surface and support the sandwich plate at the bottom, three cylindrical bars are created as rigid parts. The diameter of the rigid bars is 26 mm, same as the diameter of the bars used in the three-point bending test setup. The distance between the axes of the two rigid bars supporting the sandwich plate (Figure 5.1) is 200 mm, which is the same as the distance between the mid-points of the bars supporting the sandwich plate at its bottom surface. The rigid bars supporting the specimen are restricted in all degree of freedoms, namely, $u_x = u_y = u_z = \theta_x = \theta_y = \theta_z = 0$. The top rigid bar is free to move only in the z-direction and a given displacement is applied in the z-direction, then, $u_x = u_y = \theta_x = \theta_y = \theta_z = 0$. Considering that the structure is symmetric with respect to y-z plane, displacement in the x-direction is set to zero for the midline of the top face, namely $u_x = 0$. In this way, rigid body motion of the plate is prevented.

5.1.1. The Quarter Model

In order to reduce the computational time in the parametric studies and optimization runs, a quarter of the plate is modeled by making use of the double symmetry in the geometry and loading. Also, the number of the unit cells in a row is chosen to be seven in this study to avoid small plate sizes as previously shown in Figure 5.4. Because the aim of this study is to maximize the flexural strength of the composite sandwich plate, the plate should be large enough to ensure that the shear effects are not large and the bending loading is dominant. This condition is realized in relatively large plates. A quarter model is constructed by utilizing the x-z and y-z plane symmetry of the sandwich plate. The symmetry boundary conditions $u_y = \theta_x = \theta_z = 0$ and $u_x = \theta_y = \theta_z = 0$ are defined for the faces and the core section in the x-z and y-z symmetry planes, respectively (Figure 5.7).

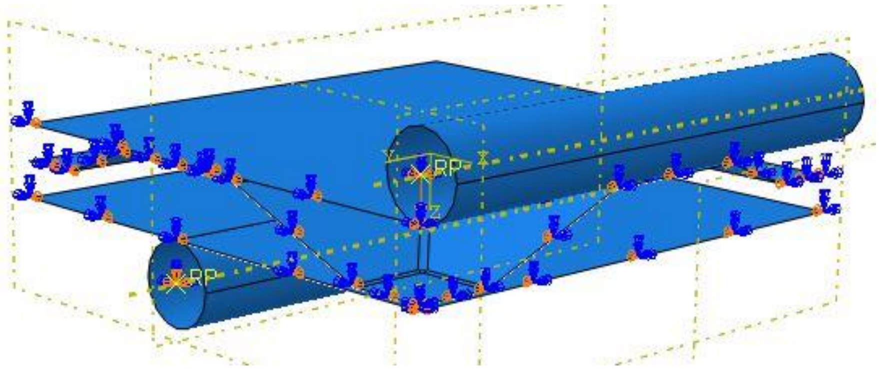

Figure 5.7. The quarter model.

The quarter model reduces the computational time and yields almost the same result as the full model as shown in the next section.

5.1.2. Validation of the Quarter Model

The predictions of the full model and the quarter model are compared with the results of the three-point bending tests performed by Uzal [30]. In Uzal's study, the unit cell has the dimensions the top side length $L_c = 50$ mm, the base length $L_b = 100$ mm, the cell height $h = 10$ mm, and the resulting angle $\theta = 21.80$ degrees. The core section of the sandwich plate consists of nine unit cells arranged in a three-by-three grid where unit cells are positioned alternately upright and upside-down. After merging nine unit cells in a three-by-three grid, fillets with 5 mm radius are introduced at all sharp edges and an outer frame with 20-mm width is added to the core structure. The core structure of this study is shown in Figure 5.8.

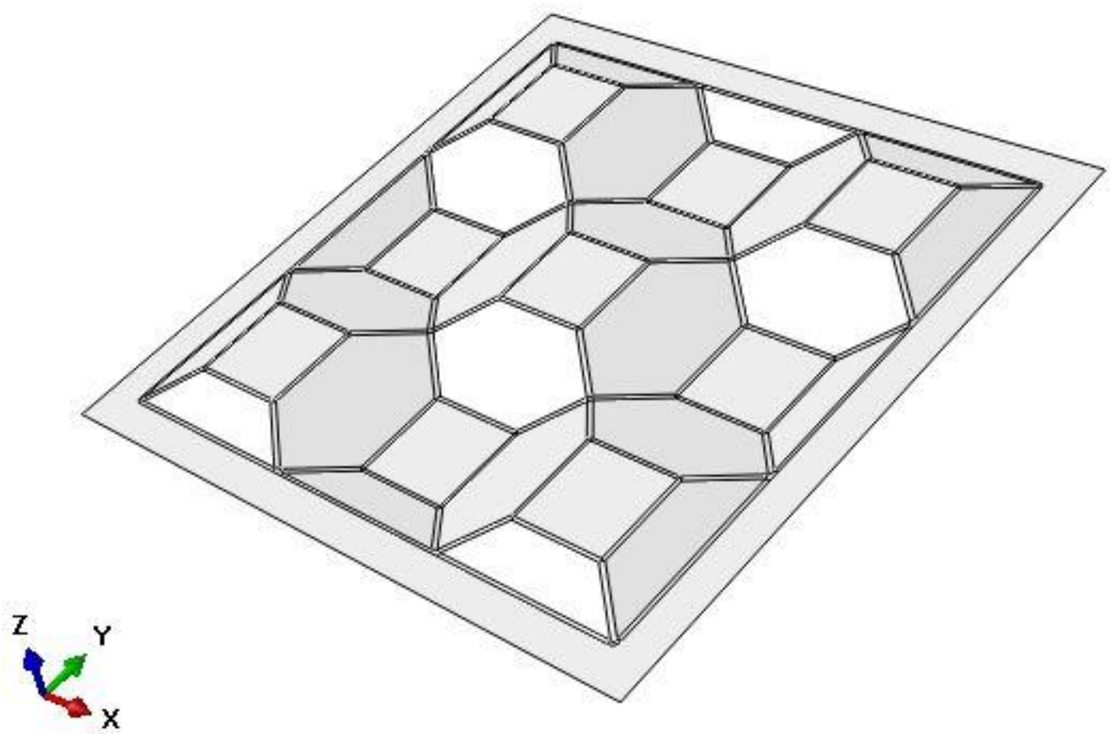

Figure 5.8. The core section of the sandwich plate used by Uzal [30].

The three-point bending tests performed by Uzal [30] are simulated using the stiffness and strength properties given in Table 5.1 and Table 5.2.

Table 5.1. Stiffness properties for unidirectional E-glass-epoxy lamina used by Uzal *et al.* [57].

E_1, longitudinal elastic modulus [GPa]	30.00
E_2, transverse elastic modulus [GPa]	5.00
ν_{12}, in-plane Poisson's ratio	0.29
G_{12}, shear modulus [GPa]	1.80

Table 5.2. Strength properties for unidirectional E-glass-epoxy lamina used by Uzal *et al.* [57].

X_t, longitudinal tensile strength [MPa]	619
X_c, longitudinal compressive strength [MPa]	-600
Y_t, transverse tensile strength [MPa]	70
Y_c, transverse compressive strength, [MPa]	-120
S, shear strength, [MPa]	41

The reaction force on the top bar obtained by the finite element analysis due to the applied displacement is compared with the measured force in the tests in order to validate the model. The analysis is conducted up to 6-mm displacement of the upper rigid bar for both models, where the maximum load is observed in the test. The load-displacement curves estimated by the full model and the quarter model demonstrate almost identical behavior with the experimentally obtained curve results up to 4-mm displacement (Figure 5.9). Both models reflect the reduction of stiffness quite successfully as the load increases. Because linear material model is used in the FE model and damage is not considered, the nonlinearity in the numerical curve is attributed to the buckling of the faces. After 4 mm displacement, the decrease in the stiffness of the finite element model is more apparent compared to the tested specimen. This difference can be ascribed to material nonlinearity and progression of damage, which are neglected in the finite element model. The maximum load 4822 N is observed at 5.50 mm displacement during the test and the full model calculates 4609 N for the same displacement. There is approximately 4% underprediction for the maximum load of the full model which is quite acceptable. The reaction forces calculated by the full model and the quarter model are almost identical, the largest difference is 0.68% up to 6-mm displacement. This means the quarter model can reliably be used in the design optimization study.

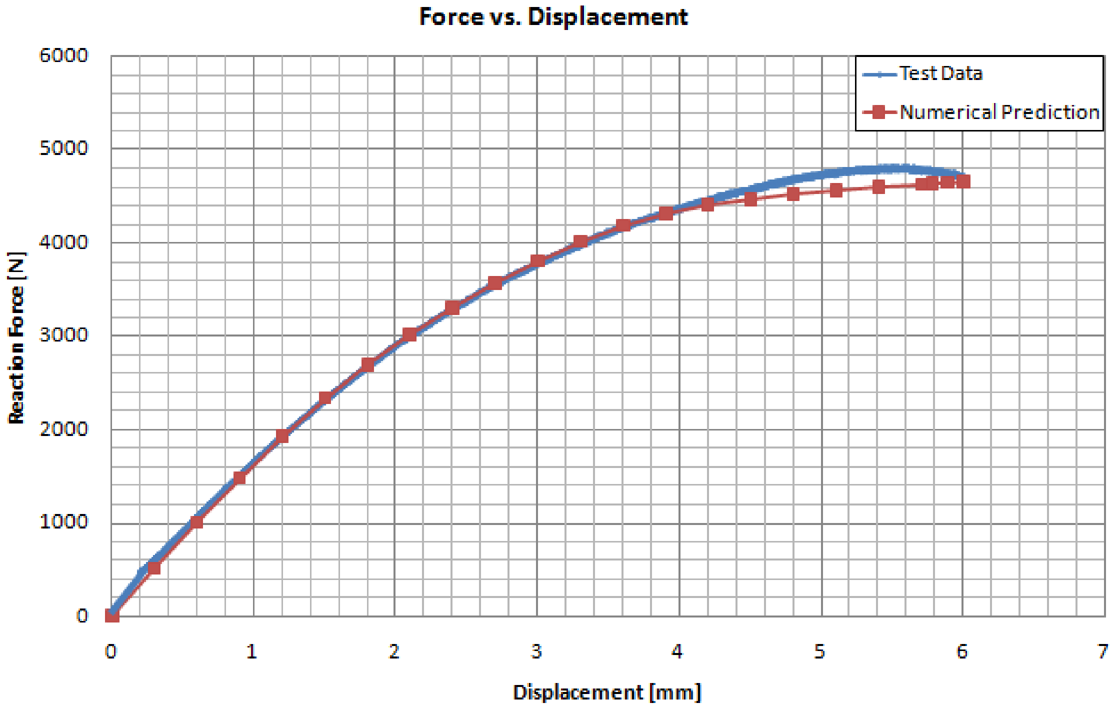

Figure 5.9. The comparison of the force-displacement curves of the FE model and the three-point bending test data [30].

In addition to the comparison of load-displacement curves, the first-ply failure load calculated by the model is also compared with the empirically determined failure-load level. The failure index is evaluated using Tsai-Hill failure criterion based on the stress state determined by the FE model. The first-ply failure load is iteratively found using the secant algorithm as used by Uzal *et al*. [30].

The secant algorithm (Equation 5.2) is a method that iteratively finds the root of a function, $f(x)$. In order to implement the method, two initial points, x_0 and x_1, are input at the beginning.

$$x_n = x_{n-1} - f(x_{n-1}) \frac{x_{n-1} - x_{n-2}}{f(x_{n-1}) - f(x_{n-2})} \tag{5.2}$$

Since the tests are conducted by controlling displacement, the displacement of the top bar is considered as the parameter representing the external loading; accordingly, it is the input parameter for the iterative root finding process and the maximum Tsai-Hill failure index of the plate is the output parameter representing the response of the plate; in other words x denotes deflection of the top bar, $f(x)$ denotes the maximum value of the failure index, $I(x)$, minus 1.0 (Equation 5.3).

$$f(x) = I(x) - 1.0 \tag{5.3}$$

Firstly, the FE model calculates the Tsai-Hill indices of the plate $I(x_0)$ and $I(x_1)$ corresponding to the first two input displacements x_0 and x_1. Then, as stated in Equation 5.2, the algorithm calculates a new displacement input based on the previous two inputs and outputs. This step is iteratively executed until the Tsai-Hill index converges to 1.0. As a stopping criterion, the difference between the last two displacement values is compared with a limiting value. When the difference between the last two deflections is smaller than 0.05 mm, the algorithm does not continue with further iterations. Finally, the displacement value that makes the maximum Tsai-Hill failure index value 1.0 is determined and at this point, the plate is assumed to have failed. Also, it should be noted that the non-linear geometric effects (NLGEOM is on) are considered in the analyses in order not to disregard local buckling failures.

Considering that the top bar applies a line load and, the junctions between the top face and the core section are sharp, the stress concentration in the model is severer than the actual case. For this reason, these stress concentration regions in the skin and the core are ignored in the failure evaluations. The stress concentrated areas of the top face and core section are highlighted red in Figure 5.10 and 5.11, respectively.

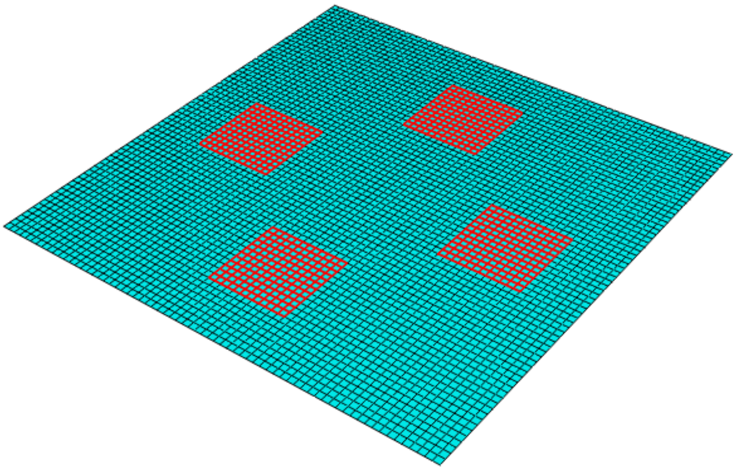

Figure 5.10. The stress concentrated areas of the top face.

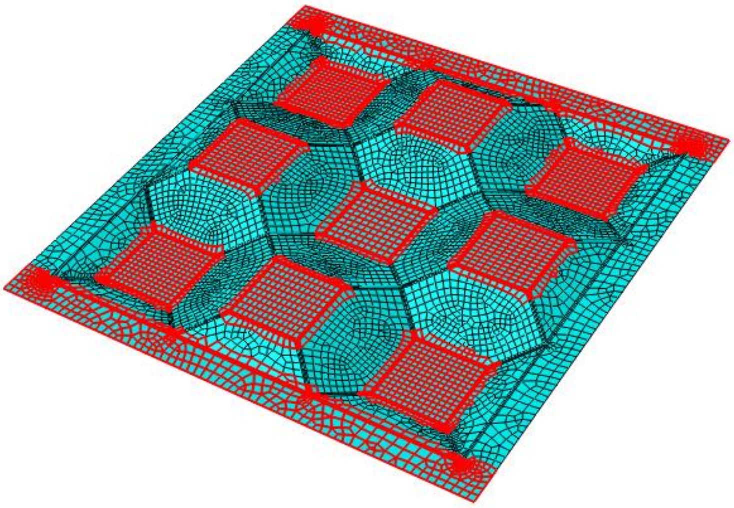

Figure 5.11. The stress concentrated areas of the core section and neglected outer frame region.

The FE model calculates the first-ply failure load as 3880 N at 3.10 mm displacement. The failure region is predicted to be on one of the angled surfaces of the unit cells located at the middle of the core section (Figure 5.12). The first-ply failure load level and the failure region prediction of the model match quite fairly with the test results of Uzal's work [57]. In Uzal's study, the first-ply failure is observed at 4240 N and 7.40 mm displacement for specimen 2 and 4110 N and 7.20 mm displacement for specimen 3 (Figure 5.13) [57]. Consequently, the failure load level is predicted by the model within about 8% error, which is satisfactory. However, the difference between the failure displacements of the model and the test arises from the use of rubber bands in the tests to improve the load distribution and avoid the stress concentrations between the top bar and top face.

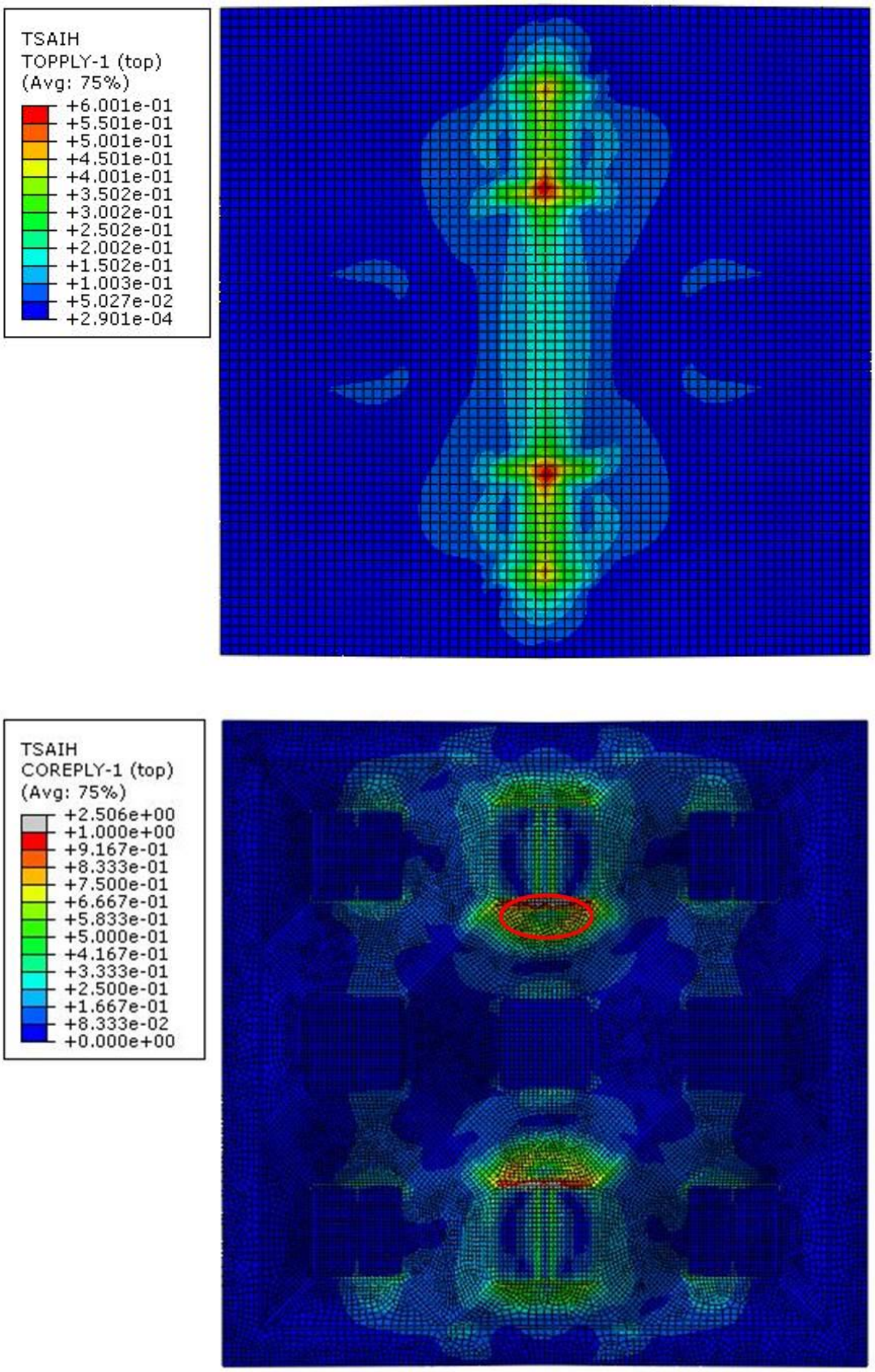

Figure 5.12. The predicted failure region of the top face (top) and the core section (bottom).

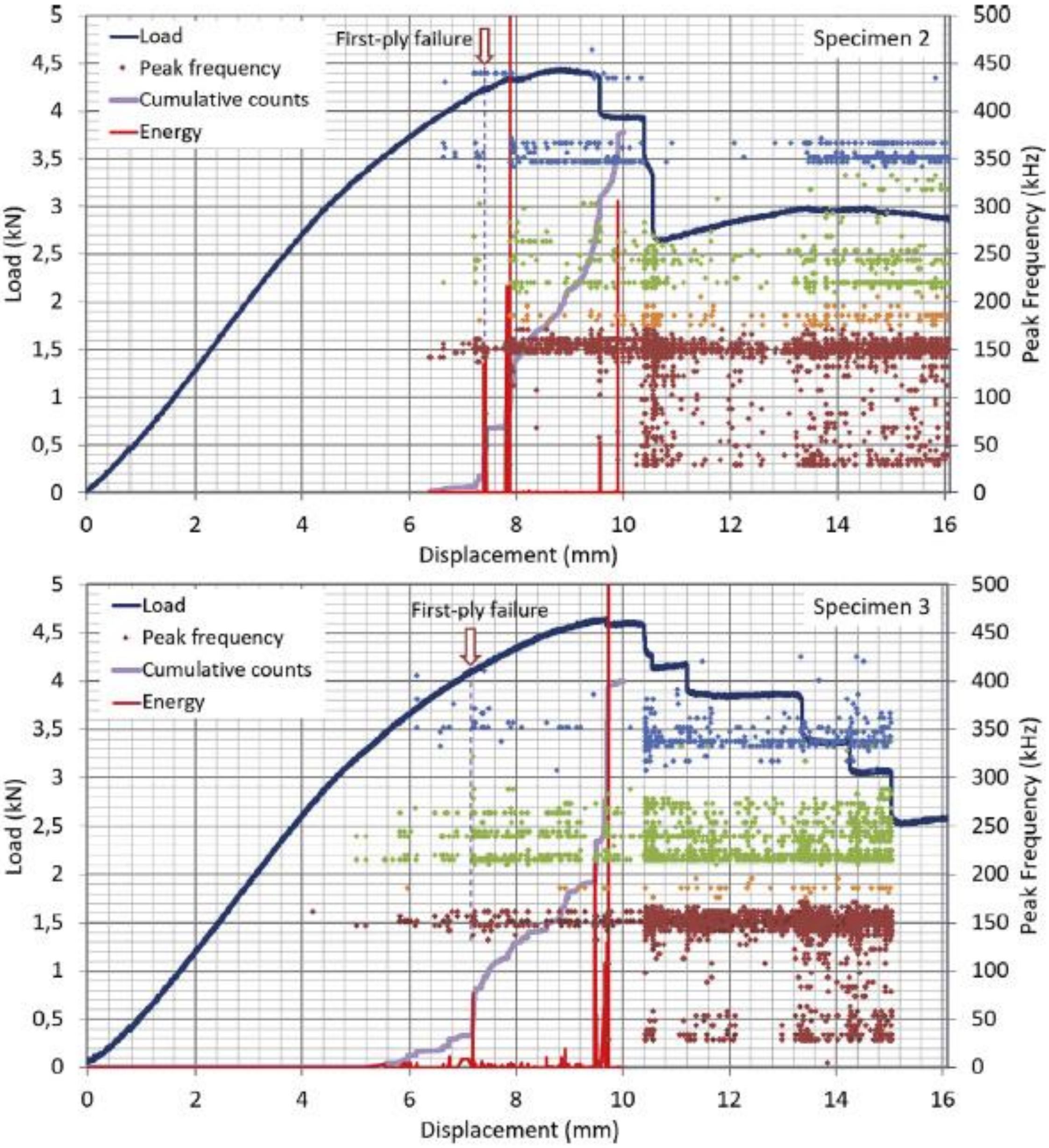

Figure 5.13. The peak frequency distribution of AE hits and load vs. displacement for two sandwich specimens under three-point bending, together with energy levels and cumulative counts of the AE hits [57].

5.2. Optimization Method

5.2.1. Geometry of the Unit Cell

The composite sandwich plate consists of two flat face plates and a core section in between having an egg-crate shape. Since the face plates have simple square shape, only the geometry of the core section is optimized to maximize the strength of the sandwich plate. It should be noted that layer thickness and ply orientations are not varied; only shape parameters are optimized.

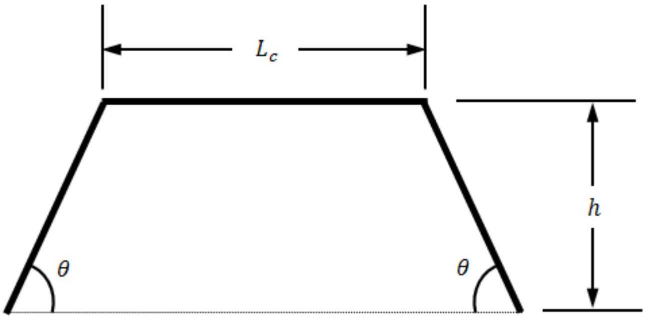

Figure 5.14. The cross-sectional geometry of a unit cell.

The unit cell has a trapezoidal cross-section (Figure 5.14). Therefore, the geometry of the unit cell can be fully described with three parameters; namely, contact length, L_c, base angle, θ, and height, h. The top area is a square with a side length L_c and the side length of the base area can be simply calculated as

$$L_b = L_c + \frac{2h}{tan\theta} \tag{5.4}$$

5.2.2. Objective Function and Design Variables

The objective function of this optimization study is the first-ply failure load of the sandwich plate. The failure load is maximized by tailoring two variables, namely, contact length L_c and base angle θ. The thickness of the sandwich plate, h, is kept constant.

Because varying these two variables results in a change in the size of the unit cells, which in turn leads to a change in the width and the length of the plate, the resulting plate strength reflects not only the effect of unit-cell geometry, but also the effect of the change in the plate size. Besides, with a change in geometry, the amount of composite material in the plate changes. For an efficient use of material in the design, changes resulting in slight increase in strength with a significantly increased use of material should not be considered as favorable in the optimization process. For these reasons, the first-ply failure load needs to be normalized to cancel out the effects of plate dimension and amount of composite material.

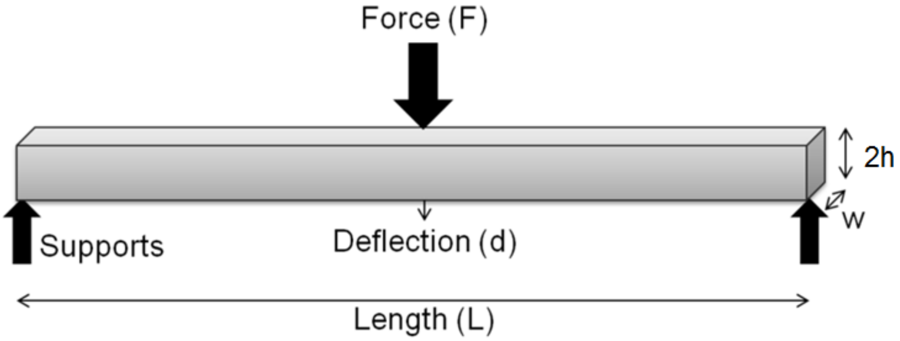

Figure 5.15. A solid beam subjected to three-point bending.

Consider a simply supported beam with dimensions $L \times w \times 2h$ under three-point bending (Figure 5.15). The force applied on the plate, F_f, that leads to failure causes a stress equal to the failure stress of the material, σ_f, given by

$$\sigma_{max} = \sigma_f = \frac{Mc}{I} = \frac{\left(\frac{F_f}{2}\frac{L}{2}\right)\left(\frac{2h}{2}\right)}{\frac{1}{12}\mathrm{w}(2h)^3} = \frac{3F_f}{8h^2}\left(\frac{L}{\mathrm{w}}\right) \tag{5.5}$$

The three-point bending formulation of critical stress for a solid beam is assumed approximately applicable for the sandwich plate in this study. w is the width of the plate and L is the distance between the lower supports, which is the same as the distance between the middles of the left-most and right-most cells, which are given by

$$L = (n-1)L_b \tag{5.6}$$

$$w = nL_b \tag{5.7}$$

where n is the number of unit cells in a row of the core section and L_b is the length of the base of a unit cell given by Eq. 5.4. In this study, n is chosen as seven to obtain a sufficiently large plate (Figure 5.16).

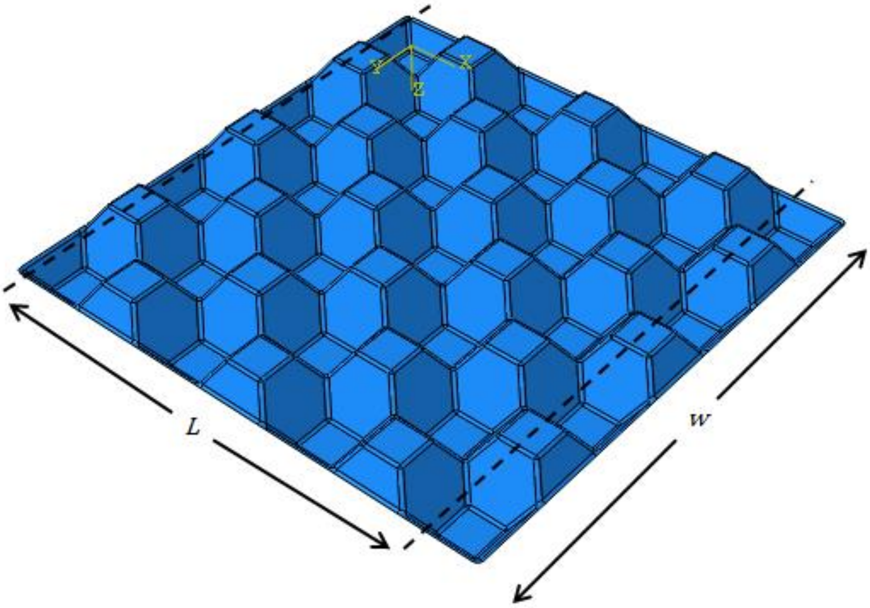

Figure 5.16. The core section with $\mathbf{7 \times 7}$ unit-cell configuration.

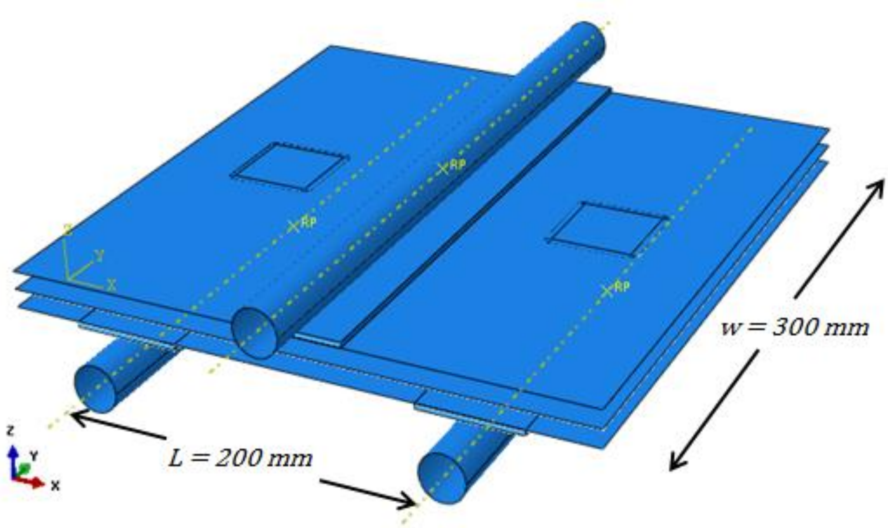

Figure 5.17. The plate dimensions used in Uzal's study [30].

The plate dimensions used in Uzal’s study [30] (Figure 5.17) are taken as the reference for the normalization. First-ply failure load level of the sandwich plate, F_0, was experimentally measured in that study and the FE model is verified using the experimental data. The same failure stress state is obtained in the plate with reference dimensions by force F_0

$$\sigma_f = \frac{M_0 c_0}{I_0} = \frac{3F_0}{8{h_0}^2}\left(\frac{L_0}{w_0}\right) \tag{5.8}$$

The thickness of the plate is 20 mm, namely $h_0 = 10$ mm, and L_0 is the span between the lower support bars 200 mm, namely $L_0 = 200$ mm, w_0 is the width being equal to 300 mm. When the failure stresses in the reference plate and any plate with different dimensions are taken as equal, from Eqs. 5.5 and 5.8, the normalized failure load, F_n, is obtained as follows

$$\sigma_f = \frac{3F_0}{8{h_0}^2}\left(\frac{L_0}{w_0}\right) = \frac{3F_f}{8h^2}\left(\frac{L}{\mathrm{w}}\right) \tag{5.9}$$

$$F_0 = F_n = F_f\left(\frac{h_0}{h}\right)^2\left(\frac{w_0}{w}\right)\frac{L}{L_0} \tag{5.10}$$

Here F_f is the failure load level predicted by the FE model. For the reference plate, F_f is equal to F_0, that means normalized failure load, F_n, is equal to the calculated failure load, F_0, for the reference plate.

For a composite plate, the load should also be normalized with respect to the composite mass per unit volume to ensure effective use of material as follows

$$F_n = F_f\left(\frac{h_0}{h}\right)^2\left(\frac{w_0}{w}\right)\left(\frac{L}{L_0}\right)\frac{\frac{m_0}{L_0 w_0 2h_0}}{\frac{m}{Lw2h}} \tag{5.11}$$

$$F_n = F_f\left(\frac{h_0}{h}\right)\left(\frac{L}{L_0}\right)^2\frac{m_0}{m} \tag{5.12}$$

where m is the mass of the portion of the composite sandwich plate between the lower supports and m_0 is the mass in the reference plate. When the geometric parameters are modified, the size of the unit cells and, in turn, the plate size change. The first-ply failure load level, F_f, is evaluated using the FE model. The normalized failure load level, F_n, is evaluated by substituting the corresponding values of L, h, and m, and value of F_f into Eq. 5.12.

Considering that thickness is not varied during the optimization study, $h = h_0$, the equation reduces to

$$F_n = F_f \left(\frac{L}{L_0}\right)^2 \left(\frac{m_0}{m}\right) \tag{5.13}$$

Since the fiber-volume fraction in the analyzed plates is taken to be the same as that of the reference plate, the volume ratio is used instead of mass ratio. Accordingly, Equation 5.13 becomes

$$F_n = F_f \left(\frac{L}{L_0}\right)^2 \left(\frac{V_0}{V}\right) \tag{5.14}$$

The deflection at the middle of the plate, δ, is given by

$$\delta = \frac{FL^3}{48EI} = \frac{FL^3}{48E\left(\frac{1}{12}w(2h)^3\right)} = \frac{FL^3}{32Ewh^3} \tag{5.15}$$

The force corresponding to 1-mm deflection for the reference plate and any plate with different dimensions are named p_0 and p, respectively. When the deflection is taken equal for these two plates as 1.00 mm, the normalized stiffness, k, is obtained as follows

$$1\,mm = \frac{p_0 {L_0}^3}{32Ew_0 {h_0}^3} = \frac{pL^3}{32Ewh^3} \tag{5.16}$$

$$k = p_0 = p\left(\frac{h_0}{h}\right)^3 \left(\frac{L}{L_0}\right)^3 \left(\frac{w_0}{w}\right) \tag{5.17}$$

The stiffness should also be normalized with respect to the composite mass per unit volume to ensure effective use of material as follows

$$k = p\left(\frac{h_0}{h}\right)^3\left(\frac{L}{L_0}\right)^3\left(\frac{w_0}{w}\right)\frac{\frac{m_0}{L_0 w_0 h_0}}{\frac{m}{Lwh}} \tag{5.18}$$

$$k = p\left(\frac{h_0}{h}\right)^2\left(\frac{L}{L_0}\right)^4\left(\frac{m_0}{m}\right) \tag{5.19}$$

Similar to the failure load normalization, the volume ratio is used instead of mass ratio. Accordingly, Equation 5.19 becomes

$$k = p\left(\frac{h_0}{h}\right)^2\left(\frac{L}{L_0}\right)^4\left(\frac{V_0}{V}\right) \tag{5.20}$$

The volume V is calculated as

$$V = V_{core} + 2V_{face} \tag{5.21}$$

The subscript 0 denotes the reference plate used in Uzal's study [30]. The volume of the composite material in reference plate is calculated as $V_0 = 235.84$ cm^3. The quarter of the core volume and the face volume sections of the reference plate are highlighted red in Figure 5.18 and Figure 5.19, respectively.

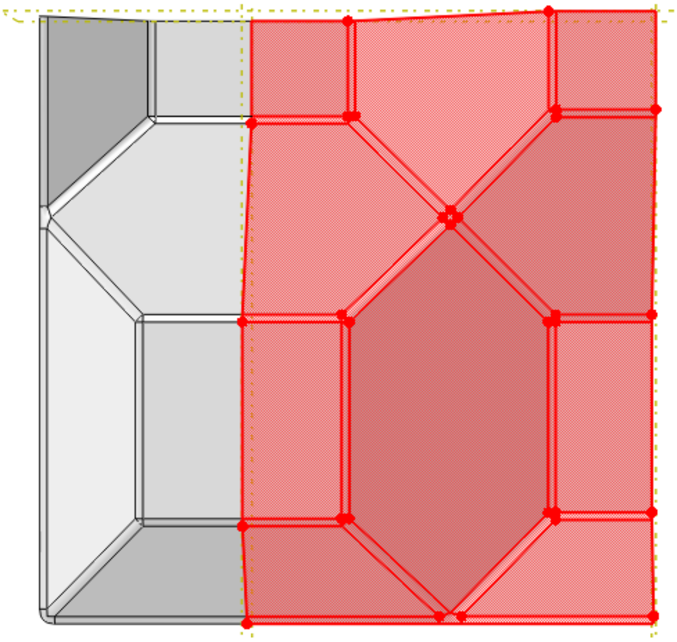

Figure 5.18. The quarter of the core volume section of the reference plate.

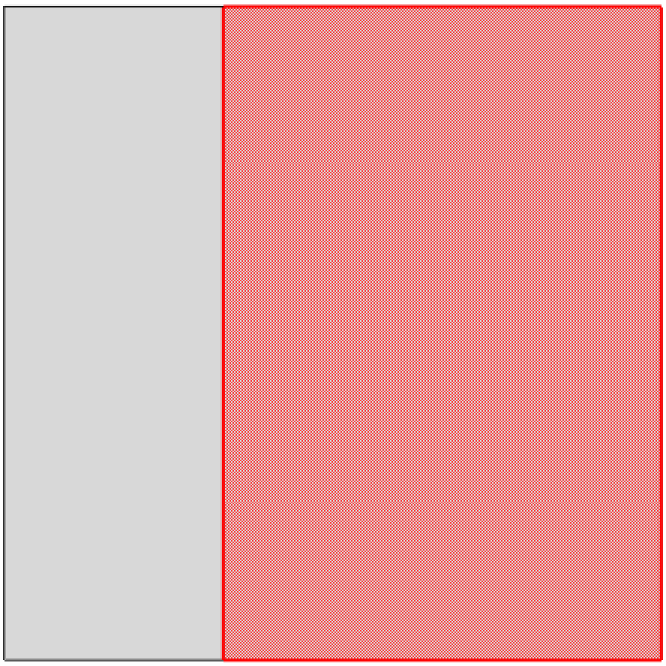

Figure 5.19. The quarter of the face volume section of the reference plate.

5.2.3. Parametric Study

Before conducting an optimization study, a parametric study is conducted to observe the individual effects of each parameter on the normalized failure load, F_n, (Eq. 5.14). Each parameter is varied between their corresponding lower and upper bounds while the other parameter is held constant. The effect of the base angle on the normalized failure load is observed for four different contact length values and the effect of the contact length is observed for four different base angle values.

Figure 5.20 shows the variation of the normalized failure load, F_n, due to changes in the contact length, L_c, for the base angles, θ, of 30°, 40°, 50°, and 60°. The normalized strength generally has a decreasing trend as the contact length increases. This effect becomes more noticeable for larger base angles. The contact length does not have a significant effect on the strength up to 25 mm for the base angle 30°. The maximum normalized failure load is observed at the contact length of 10 mm for all base angles except for 30° and 50°. The maximum normalized failure load is 18144 N, which is observed for a contact length of 10 mm and base angle of 60°. Although the overall trend is the decrease of the normalized failure load with larger contact lengths, this trend is not consistent and there are up and downs particularly for the contact lengths between 17.50 and 25 mm for the base angles of 40° and 50°. These up and downs may be caused by coarse meshing for the corresponding plate sizes.

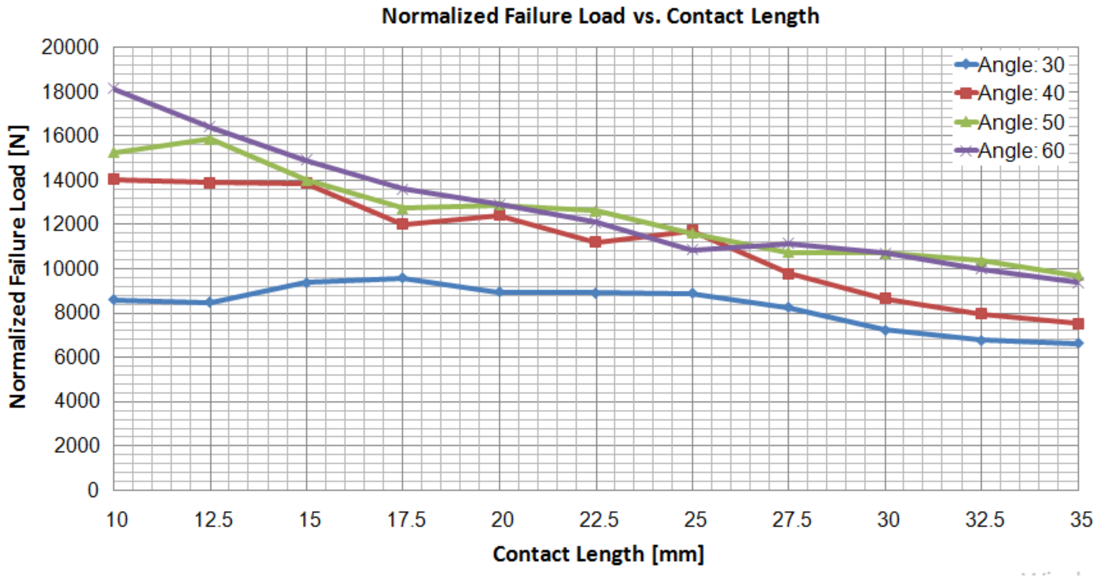

Figure 5.20. The variation of the normalized failure load with the contact length, $\boldsymbol{L_c}$.

Figure 5.21 presents the variation of the normalized failure load, F_n, due to change in the base angle, θ, for the contact lengths, L_c, of 15, 20, 25 and 30 mm. The normalized failure load generally has an increasing trend as the base angle increases up to 45°. Between the base angles 20° and 45°, the normalized failure load increases significantly. The maximum value of F_n is observed at 55° for all contact lengths except for 30 mm. The maximum value is obtained as 15587 N for the base angle of 55° and contact length of 15 mm. While there is a trend of increasing strength with increased base angle up to 40°, no significant effect of the base angle is observed beyond 40° except for the contact length of 15 mm.

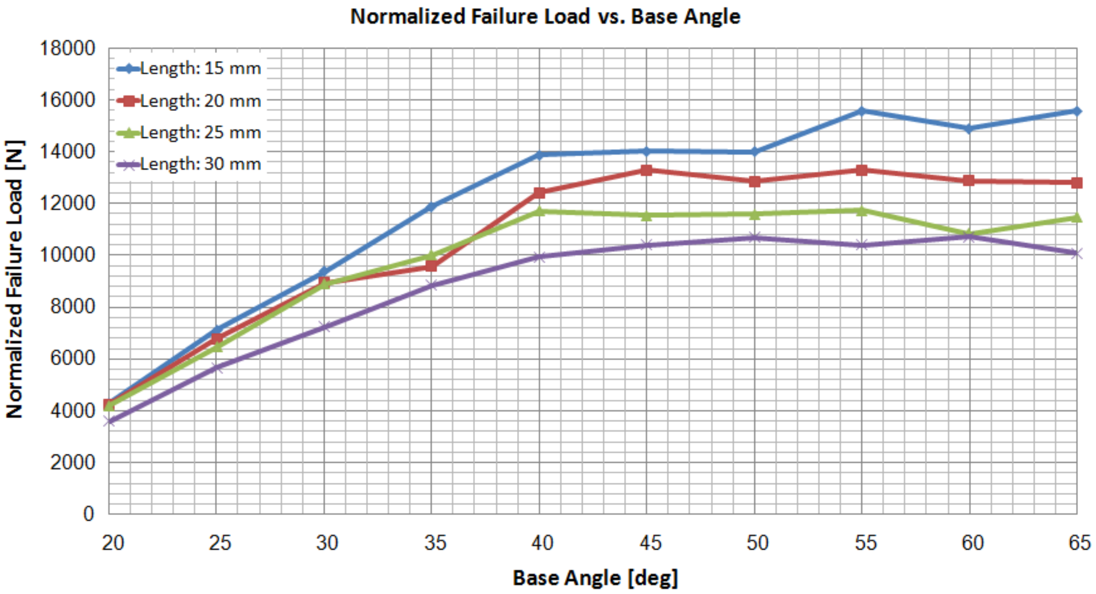

Figure 5.21. The variation of the normalized failure load with the base angle, $\boldsymbol{\theta}$.

In order to observe the effect of the cell height, h, on the normalized failure load, F_n, the parametric study is also performed for different cell height values, namely $h = 5, 15, 20, 30$ mm at the point $L_c = 25$ mm and $\theta = 40°$. Figure 5.23 shows the change of the failure load and the normalized failure load with different cell height values. As the cell height increases, the failure load decreases slightly. However, there is a sharp decline in the normalized failure load due to high degrading factors of mass and cell height normalization (see Equation 5.12). It can be concluded that increasing the thickness of the sandwich plate does not contribute to the strength. Moreover, increasing the thickness increases the mass of the overall structure and reduces the specific strength.

Figure 5.22 shows the failure regions of the plates with different cell heights. The failure regions are on one of the angled surfaces of the unit cells located at the middle of the core section for the cell heights of 5 mm and 10 mm. However, the failure region is the saddle junction regions for the cell heights 15 mm and 20 mm. This change in the failure region may be attributed to coarse meshing and resulting stress concentration in the saddle junction regions. For the cell height of 30 mm, the failure occurs at the top plate due to excessive buckling at a region next to core-top face contact.

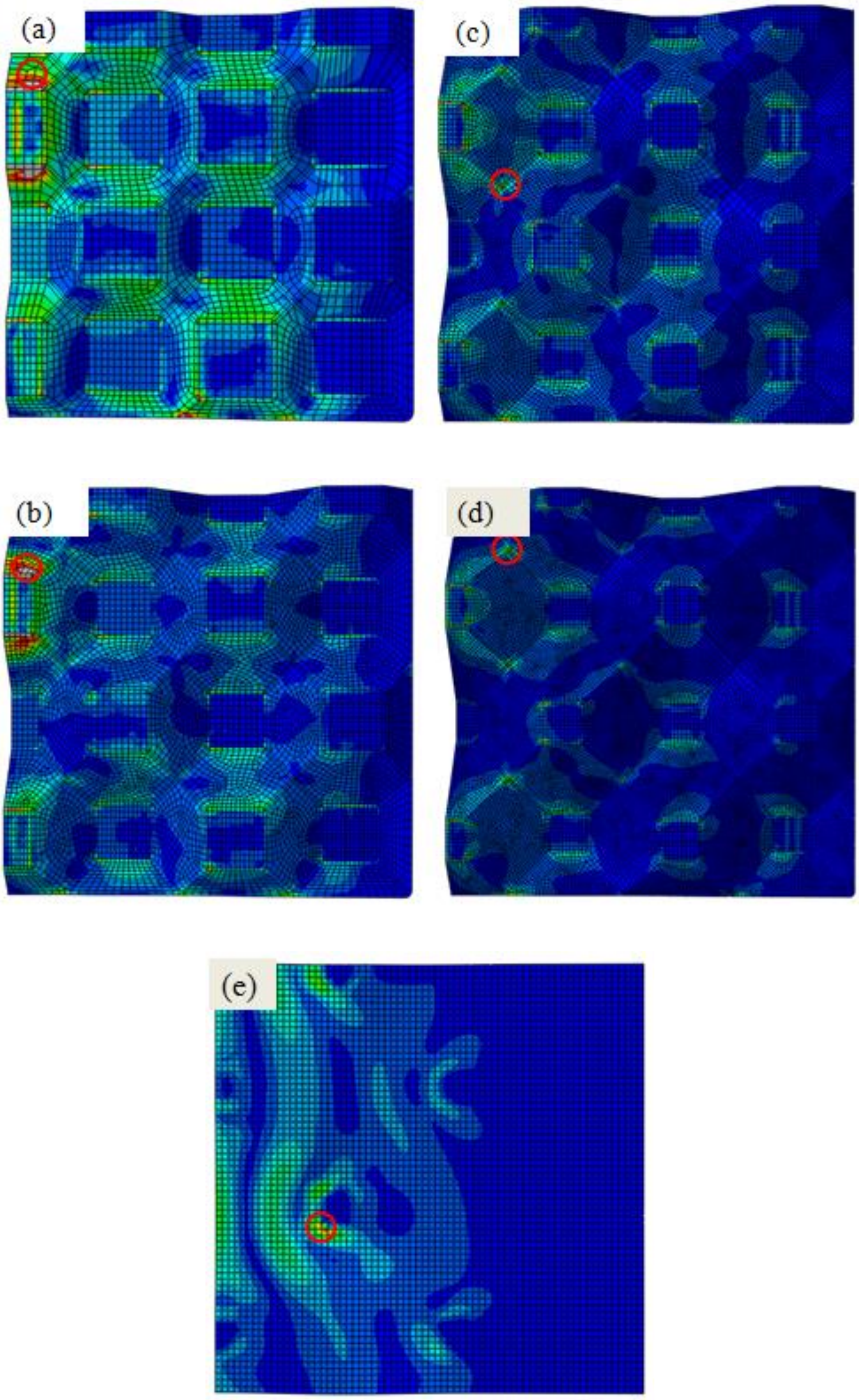

Figure 5.22. The failure regions of the plate with the cell heights of (a) 5 mm, (b) 10 mm, (c) 15 mm, (d) 20 mm, and (e) 30 mm.

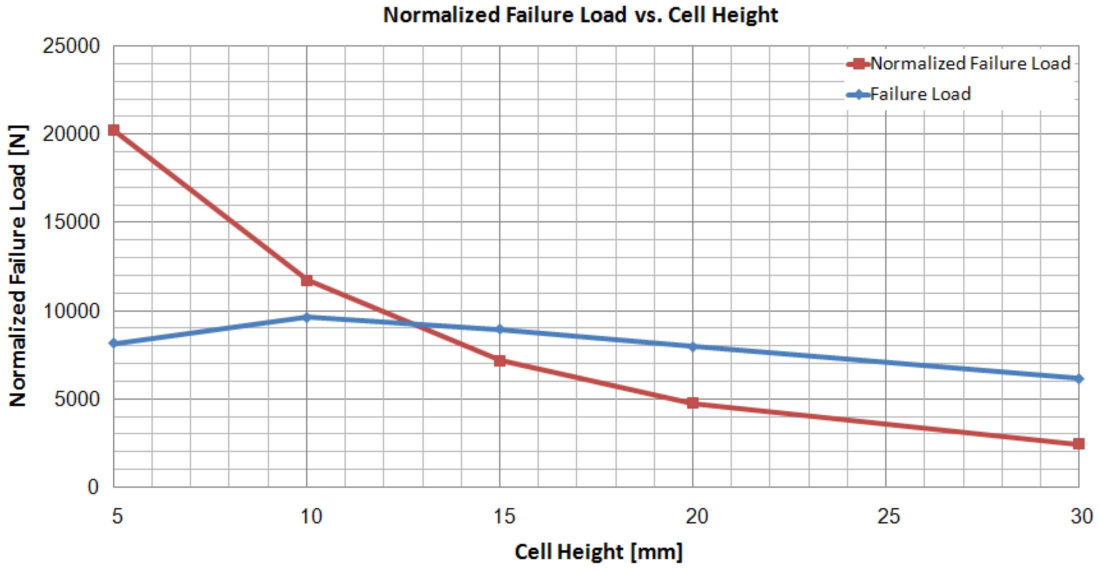

Figure 5.23. The variation of the normalized failure load at the point $\boldsymbol{L_c = 25}$ mm and $\boldsymbol{\theta = 40°}$ with the cell height, $\boldsymbol{h}$.

5.2.4. Optimization Method

The aim of this study is to maximize the strength of the plate under three-point bending by optimizing the core structure. Therefore, the normalized failure load F_n is maximized during the optimization process. Since the optimization problem has just two variables and the ranges of these variables are narrow, the maximization of the normalized failure load is performed by Nelder-Mead algorithm, which is explained in detail in Appendix A. Nelder-Mead is a deterministic search algorithm developed to find the local minimum of a function. Therefore, the negative of the normalized strength, F_n, is taken as the objective function to be minimized. Because Nelder-Mead is a local optimization algorithm, the converged optimum design may depend on the starting point and a local optimum much worse than the globally optimum design may be obtained. For this reason, the optimization search is repeated for 20 times to ensure that the result is the global optimum or near global optimum.

Because Nelder-Mead is an unconstrained search algorithm, penalty functions are defined for cases in which the algorithm assigns values for the optimization variables outside their allowable range. In these cases, penalties are added to the objective function in order to force the optimization process to search the optimum within the design space.

The design space is determined by considering the manufacturability of the core section using a PLA mold and extracting the final product from this mold. The lower and upper bounds on the contact length, L_c, and the base angle, θ (Figure 5.14) are chosen as 15 mm and 25 mm, and 30° and 45°, respectively. In the parametric study, it is observed that the normalized failure load increases as the contact length decreases (Figure 5.20) and the base angle increases (Figure 5.21). However, the lower limit for the contact length and the upper limit for the base angle are imposed considering the manufacturability of the core part. In early attempts of manufacturing a core part, it is being observed that unit cells having small contact lengths and large base angles pose difficulty in full impregnation of resin into the reinforcing fabric and removal of the part from the mold. The upper bound for the contact length and the lower bound for the base angle are selected to avoid unnecessarily large models considering that the normalized failure load decreases for large contact lengths and small base angles.

The optimization problem can be described as below

$$minimize \quad f_o = -F_n(L_c, \theta) + \sum_{k=0}^{4} p_k(L_c, \theta)$$

where f_o is the objective function, F_n is the normalized failure load and p_k is the penalty function. The penalty function values are added to the objective function when the upper or lower limit of a design variable is exceeded. These functions ensure that the optimum design is searched within the design space.

The objective function can be expanded as follows

$$f_o = -F_f(L_c, \theta)\left(\frac{L_c}{L_0}\right)^2\left(\frac{V_0}{V}\right) + \sum_{k=0}^{4} p_k(L_c, \theta)$$

$$L_{c,min} \leq L_c \leq L_{c,max}, \qquad \theta_{min} \leq \theta \leq \theta_{max}$$

where

$$L_{c,min} = 15 \text{ mm}, \qquad L_{c,max} = 25 \text{ mm}, \qquad \theta_{min} = 45°, \quad \theta_{max} = 60°$$

The four penalty functions are

$$p_1(L_c, \theta) = 5000\left(L_{c,min} - L_c\right) \qquad \text{if} \qquad L_c < L_{c,min}$$

$$p_2(L_c, \theta) = 5000\left(L_c - L_{c,max}\right) \qquad \text{if} \qquad L_c > L_{c,max}$$

$$p_3(L_c, \theta) = 5000(\theta_{min} - \theta) \qquad \text{if} \qquad \theta < \theta_{min}$$

$$p_4(L_c, \theta) = 5000(\theta - \theta_{max}) \qquad \text{if} \qquad \theta > \theta_{max}$$

$$p_1 = p_2 = p_3 = p_4 = 0 \quad \text{if} \quad L_{c,min} \leq L_c \leq L_{c,max} \quad \text{and} \quad \theta_{min} \leq \theta \leq \theta_{max}$$

The optimization results are listed in Table 5.3. The optimum contact length, L_c, and base angle, θ, for each iteration are given together with the core volume, face volume, failure load, and normalized failure load. The results show that 5 out of 20 iterations clearly converge to the point approximately $L_c = 15$ mm and $\theta = 56.50°$ resulting in the normalized failure load of 15645 N. The numbers of these iterations are 1, 3, 5, 8 and 17. The other optimum points can be considered as local minimums since the Nelder-Mead method does not find the global minimum and may converge to local minimums in a non-convex design problem. However, a significant population of 20 runs is performed to ensure the algorithm converges to the optimum solution multiple times.

The first ply failure and peak loads observed in the three-point bending tests of the previous study [57] as well as the finite element model prediction are given in Table 5.4. It can be concluded that the bending strength of the sandwich plate is increased approximately 3.70 times compared to the initial design.

Table 5.3. Optimization results.

Iteration	Best Point		Core Volume (cm^3)	Face Volume (cm^3)	Failure Load, F_f (N)	Normalized Failure Load, F_n (N)
	Contact Length, L_c, (mm)	Base Angle, θ, deg				
1	15.01	56.38°	75.42	80.77	14370	15646
2	16.30	52.10°	88.92	102.38	13054	14710
3	15.01	56.35°	75.48	80.88	14365	15644
4	16.42	54.79°	84.66	93.99	13706	15182
5	15.01	56.51°	75.25	80.43	14382	15645
6	18.73	50.55°	104.63	124.85	12200	13975
7	17.66	54.95°	90.52	101.26	12904	14345
8	15.01	56.43°	75.36	80.64	14375	15645
9	15.82	60.01°	74.01	75.45	13711	14511
10	15.10	52.55°	82.22	93.28	13462	15065
11	15.63	50.72°	88.32	103.16	13165	14934
12	15.87	50.50°	89.96	105.53	13221	15027
13	15.00	56.69°	74.91	79.83	14294	15524
14	15.33	56.39°	76.88	82.57	14168	15448
15	15.43	53.65°	81.82	91.60	13972	15538
16	16.86	56.86°	83.46	90.26	13411	14671
17	15.01	56.59°	75.13	80.21	14391	15645
18	17.09	53.07°	91.05	104.05	12602	14151
19	15.02	56.05°	75.96	81.76	14321	15632
20	15.98	55.10°	82.01	90.31	13642	15053

Table 5.4. The test results of the sandwich specimens and the FE model first-ply failure load prediction of the previous study [57].

Results	1st ply failure load [N]	Peak load [N]
Specimen 1	-	4820
Specimen 2	4240	4430
Specimen 3	4110	4650
FEM	3961	4676

The finite element analysis for the optimum design is repeated in the quarter model. The model calculates the first-ply failure load as 15051 N at 3.42 mm displacement. The failure region is predicted to be on one of the angled surfaces of the unit cells located at the middle of the core section (Figure 5.24). The failure occurs at a similar region with the reference plate [57].

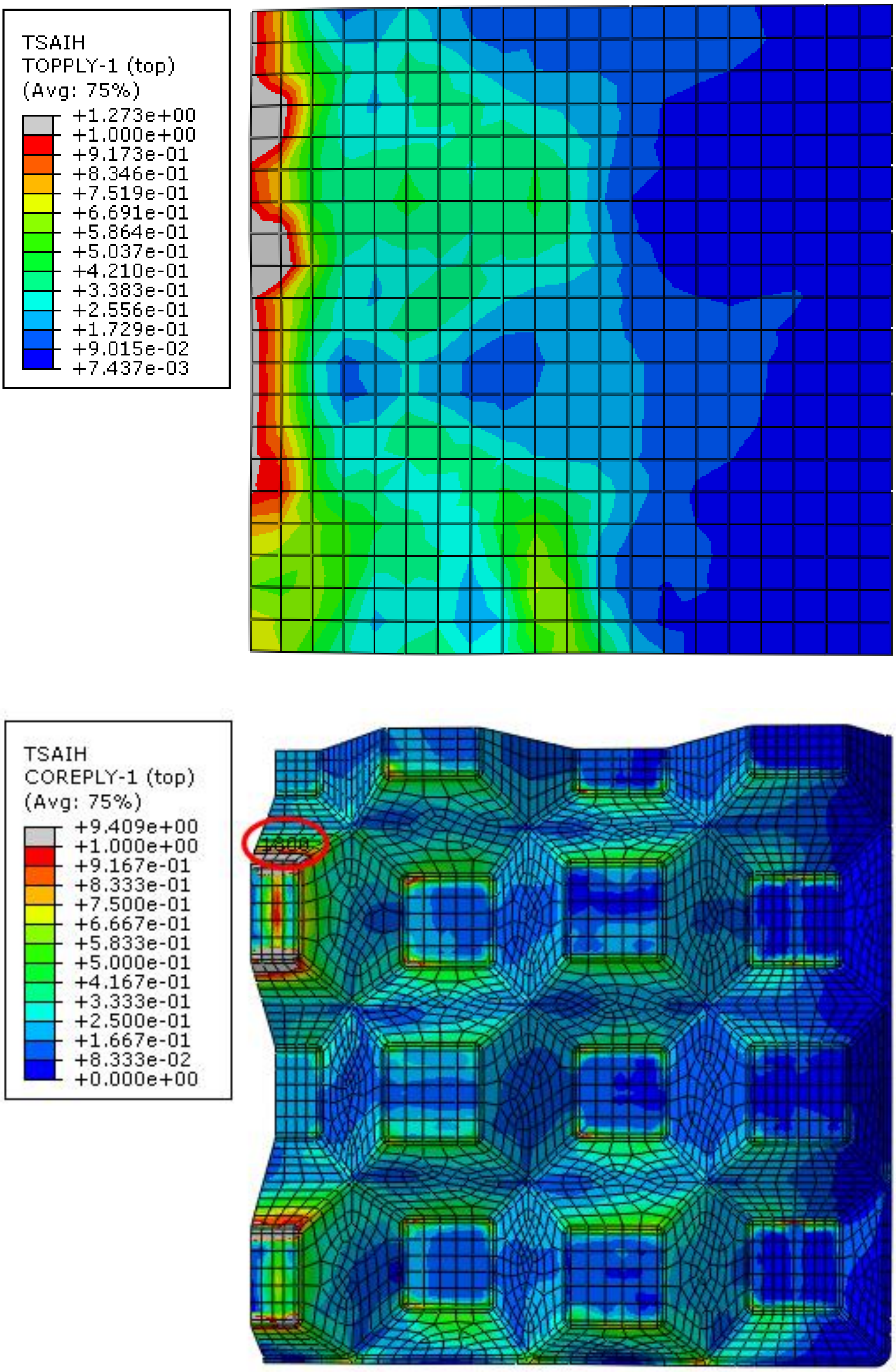

Figure 5.24. The predicted failure region of the top face (top) and the core section (bottom) for the optimum plate.

6. EXPERIMENTAL VALIDATION AND DISCUSSION

The optimum core geometry is manufactured and tested in order to observe the failure behavior of the optimum sandwich design and verify the finite element model and the failure model. Two sandwich plates are manufactured. The stacking sequence and measured thicknesses of the specimens are given in Table 6.1. The measured larger thickness of the core is due to larger resin content in the core section and it does not significantly contribute to the strength of the material. Therefore, the measured average ply thickness of the quasi-isotropic tension specimens are used in the finite element model. The upper face, lower face and core ply thicknesses are given as 0.15 mm.

Table 6.1. The stacking sequence and measured thicknesses of the specimens.

	Upper Face	Lower Face	Core
Stacking Sequence	$[0/45/-45/90]_s$	$[0/45/-45/90]_s$	$[0/45/-45/90]_s$
Thickness	0.15 mm/ply	0.15 mm/ply	0.18 mm/ply

6.1. Test Setup for Three-Point Bending of the Sandwich Plates

Three-point bending tests are conducted on the specimens using MTS servo hydraulic test hardware with a three-point bending fixture. The test setup is shown in Figure 6.1. Two bars provide support underneath the specimen and one bar applies force on the specimen. The circular bars have a diameter of 26 mm and length of 30 cm. Two acoustic emission sensors are clamped onto the upper face of the specimen with rubber bands. The sensors are positioned with a sufficient distance from the loading bar in order not to dislocate during the test. The test is displacement-controlled with a rate of 5 mm/min.

First-ply failure load is estimated by the model assuming that damage first initiates due to intralaminar failure mode not interlaminar failure mode. Because, the model does not account for progressive damage, the failure behavior of the plate after initial damage cannot be predicted by the model. Tests are conducted to validate the model regarding its first-ply failure assessment and also to observe the failure response of the sandwich plate beyond the initial damage. In the initial attempts of testing, debonding in the interface between the core and the face sheets occurred before initial intralaminar failure, because the shear stresses at the interface exceeded the shear strength of the adhesive material. The tests are repeated for the cases in which the faces and the core are bonded both by applying J-B® Weld plastic bonder and L285 laminating resin with H285 hardener. However, both bonding materials failed before the core section is damaged.

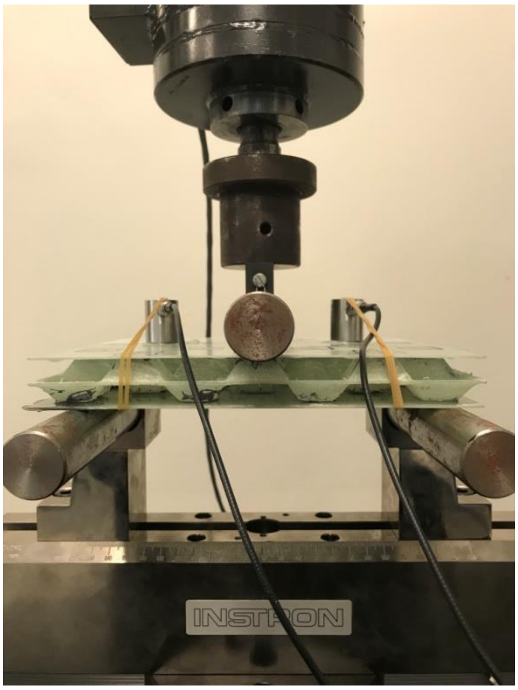

Figure 6.1. The three-point bending test setup.

Figure 6.2 and 6.3 show the deformed shapes of specimen 1 and specimen 2, respectively. The peak forces are recorded as 4867 N and 4834 N at 1.34 mm and 1.59 mm displacement for specimen 1 and specimen 2, respectively. The overall intralaminar failure behavior of the specimens could not be observed due to the premature split-off between the top faces and the core sections.

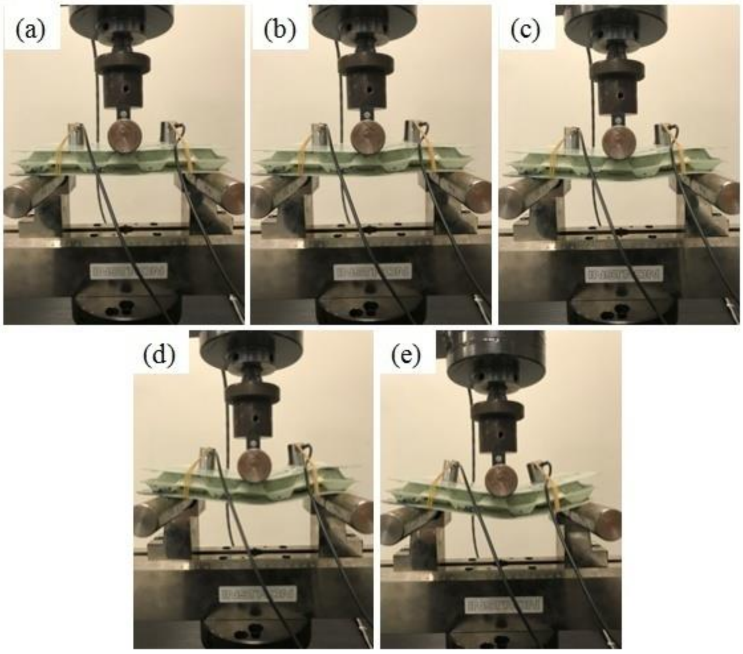

Figure 6.2. The deformed shapes of specimen 1 during the three-point bending test corresponding to the top bar displacements and loads (a) 2.58 mm - 2187 N, (b) 4.67 mm - 2037 N, (c) 7.42 mm - 1989 N, (d) 11.25 mm - 2296 N, and (e) 14.83 mm - 191 N.

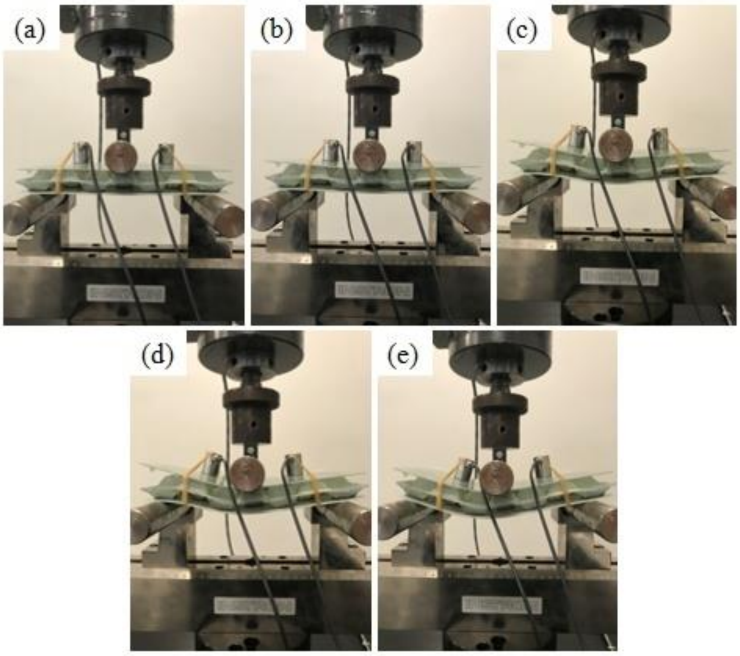

Figure 6.3. The deformed shapes of specimen 2 during the three-point bending test corresponding to the top bar displacements and loads (a) 1.83 mm - 4650 N, (b) 4.08 mm - 3393 N, (c) 8.67 mm - 2842 N, (d) 12.33 mm - 2163 N, and (e) 16.75 mm - 320 N.

6.2. Three-Point Bending Test Results

Figure 6.4 shows the load-displacement behavior of the specimen 1. Sudden load-drops are marked and numbered from 1 to 6. The load increases linearly up to the maximum load of 4867 N. At the maximum load, the top face and the core splits off at the sides. After that, the load bearing capacity of the sandwich structure dramatically reduces to 1534 N. Figure 6.5 shows the separation at the side region of the specimen 1. After the first split-off, the load starts to increase with a less steep slope due to the stiffness loss. When the displacement reaches about 4.50 mm, the second load-drop occurs at about 3465 N. The load-drops intermittently occur as the displacement increases and the overall sandwich structure loses its stiffness and load bearing capacity significantly. The load drop 1 shows the first split-off, the load-drops 2, 3, 4 shows the second split-off and the load-drop 6 shows the third and final split-off. The test for the first specimen is stopped after the sixth load-drop when the load bearing capacity is completely lost due to separation of the top face from the core section.

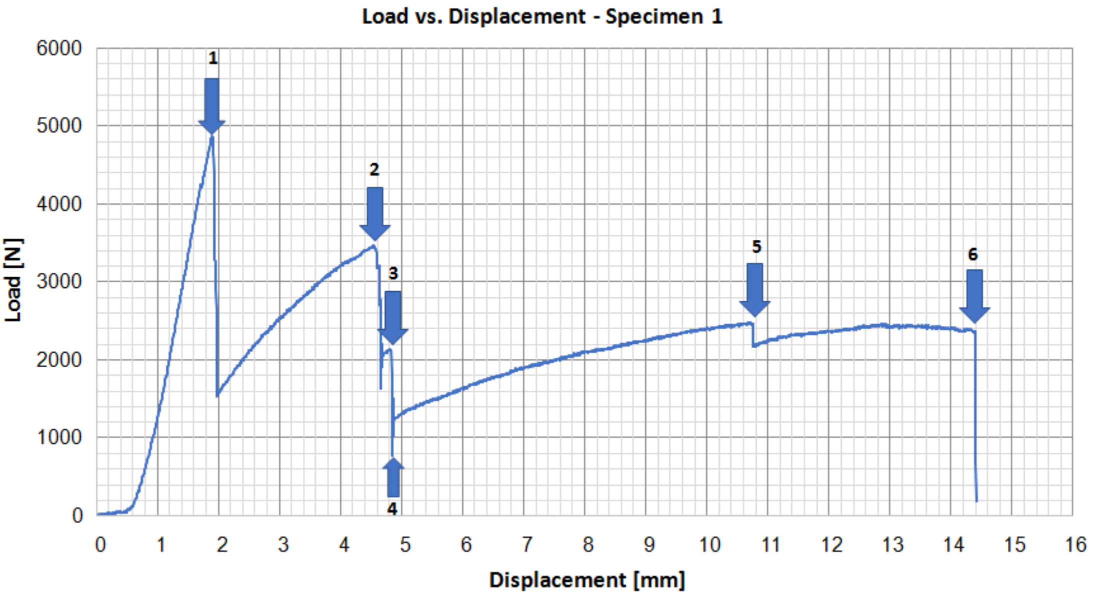

Figure 6.4. Load-displacement curve of the specimen 1.

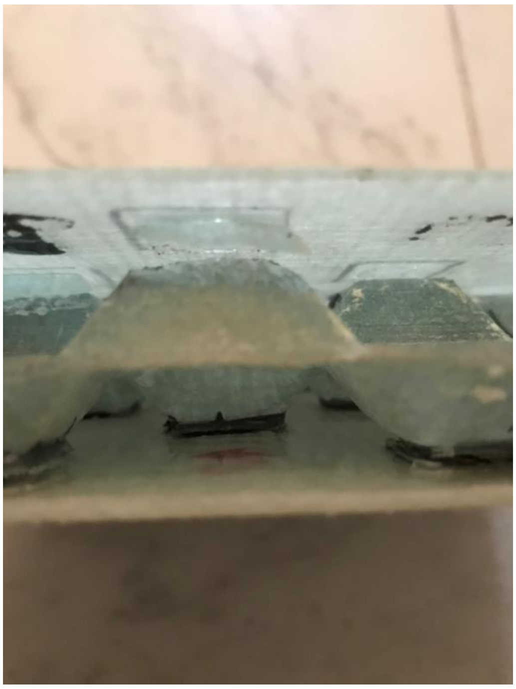

Figure 6.5. Split-off between the top face and the core section of the sandwich structure.

In order to investigate the failure mechanisms, the AE data are analyzed in the frequency spectrum. Figure 6.6 shows the peak frequency distribution for the first specimen. There are formations of two frequency bands in the test, which are 20-120 kHz and 340-460 kHz. From the AE frequency distribution, it may be concluded that matrix cracking is the activated failure mechanism for the sandwich structure since the activated 20-120 kHz frequency band is also observed in the tension tests of quasi-isotropic specimens. The matrix cracks may develop at the resin-rich regions of the top face-core junctions. When these cracks reach to a critical size, the junction cannot bear the shear load and it breaks. It can be seen that following the dense signal recordings, the top face-core bonds break and sudden load-drops occur due to excessive matrix cracks. The signals from 340-460 kHz are more densely recorded just prior and at the moment of the load-drops. Therefore, these signals may be due to noise during the split-offs and relative movement of the top face and the core section.

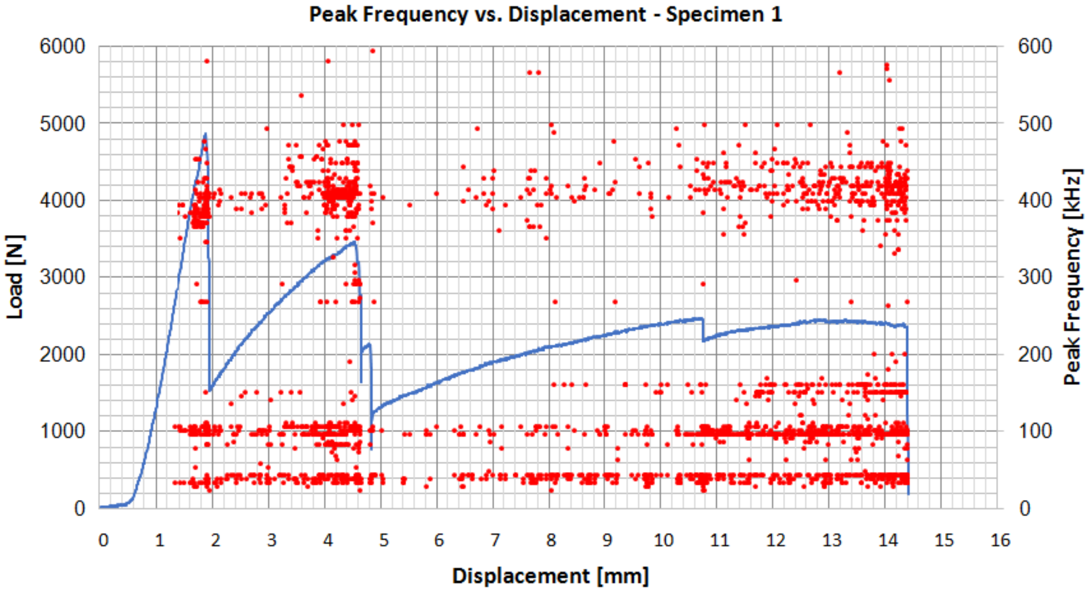

Figure 6.6. Peak frequency vs. displacement for the first specimen.

Figure 6.7 shows the load-displacement behavior of the specimen 2. Sudden load-drops are marked and numbered from 1 to 12. The load increases linearly up to the maximum load of 4834 N. At the maximum load, the bonding between the top face and the core starts to break at the regions closer to the edges. Up to the third load-drop, there are two mini load-drops where the stiffness does not decrease significantly. At the third and fourth load-drop, the first split off occurs between the top face and the core, therefore the load dramatically drops to 1925 N. After the first split-off, the load starts to increase with a less steep slope due to the stiffness loss. Starting from the load-drop 4 up to the load-drop 9, the displacement increases with frequent small load-drops where the load capacity of the sandwich structure does not fall remarkably. However, at the load-drops 9, 10 and 11, the second split-off occurs and the load drops to 1374 N. After the second split-off, the load starts to increase again with a very small slope due to significant loss of stiffness. Finally, the test is stopped at the load-drop 12, where the third and final split-off occurs and the top face mostly separates from the core.

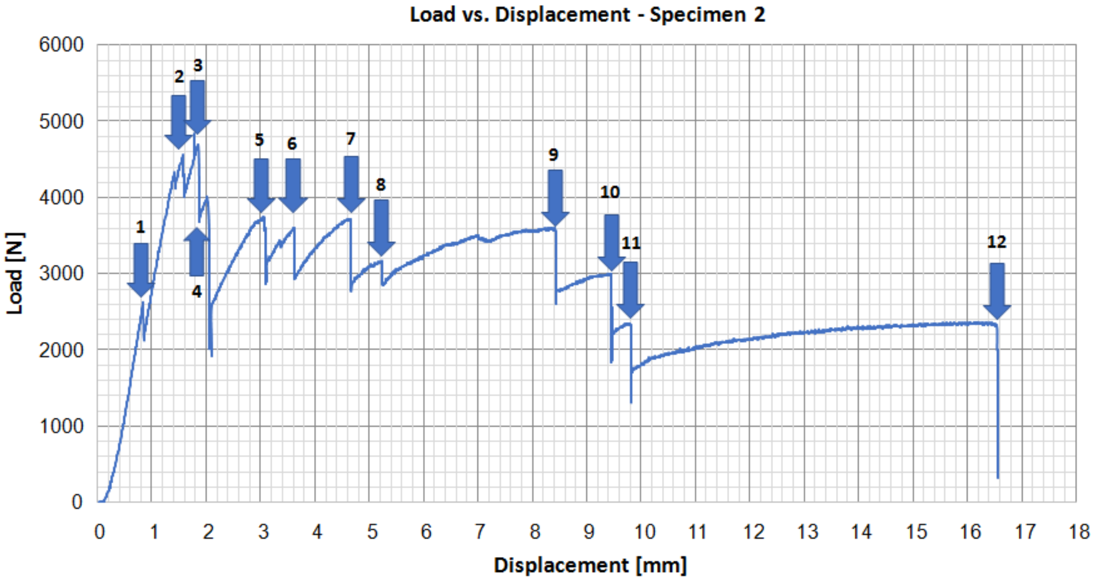

Figure 6.7. Load-displacement curve of the specimen 2.

Figure 6.8 shows the peak frequency distribution for the second specimen. Similar to the first specimen, two frequency bands form in the test as 20-120 kHz and 340-460 kHz. However, after the first load-drop, there are no intense signal recordings and 20-120 kHz frequency band remains indicating the only active damage mechanism. This situation may be associated with that since there are too many load-drops compared with specimen 1, the damage mechanisms cannot be developed. Since the main frequency band formed is 20-120 kHz, it may be concluded that matrix cracking in the resin-rich regions of the top face-core junctions is the essential failure mechanism observed in specimen 2. The density of the signals can be correlated with the severity of the load drops. As the signal density increases, the following load drop becomes more dramatically. The frequency band of 340-460 kHz may be associated with noise similar to specimen 1 since these signals are recorded just prior and at the moment of the load-drops.

The load-displacement diagram predicted by the finite element model for the optimum core design is compared with the linear portion of the experimentally obtained ones in Figure 6.9. The stiffness prediction of the finite element model is in a good agreement with the test results of specimens 1 and 2.

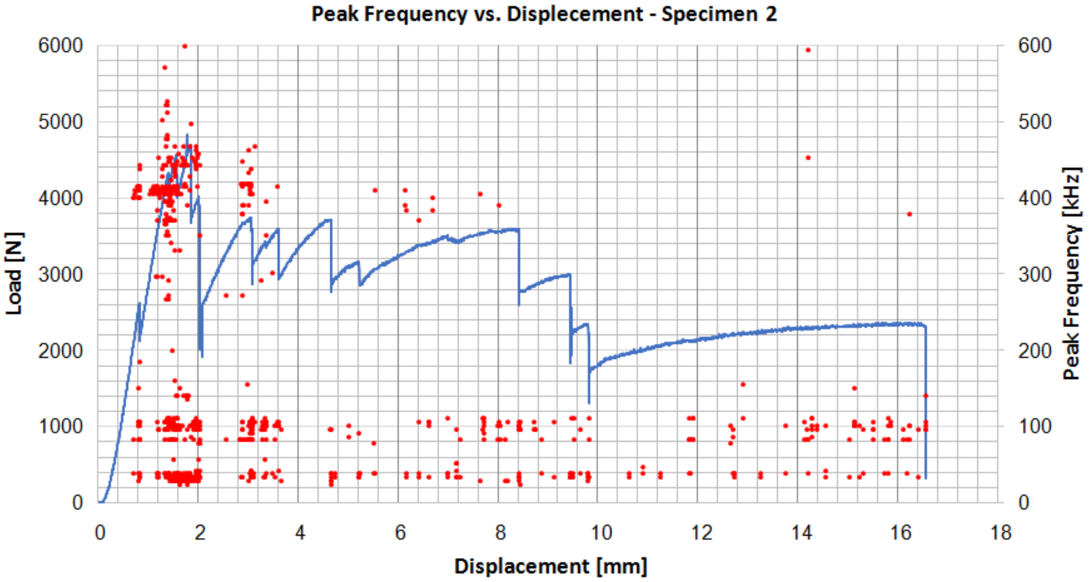

Figure 6.8. Frequency vs. displacement for the second specimen.

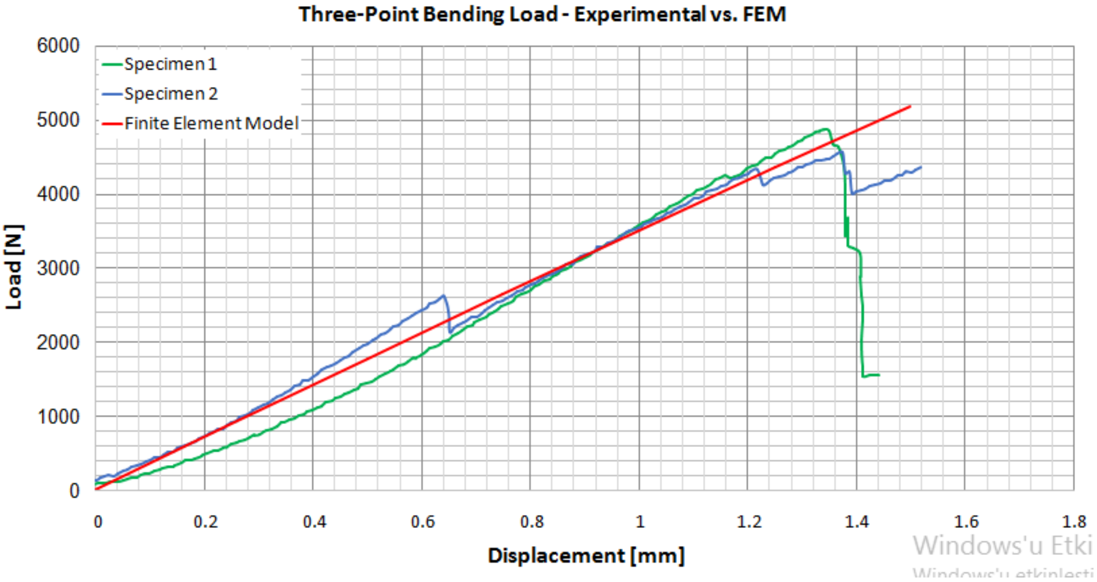

Figure 6.9. Load vs. displacement comparison of the test results with the finite element model.

6.3. Three-Point Bending Test of a Foam-Core Sandwich Plate

A three-point bending test is performed on a foam-core sandwich plate to compare its stiffness and strength properties with the reference plate and the optimum plate. The plate size is 300 × 300 × 23.6 mm and the foam core thickness is 20 mm. Plate dimensions are the same as that of the reference plate. The stacking sequence and measured average thicknesses of the specimens are given in Table 6.2. Comparison of Tables 6.1 and 6.2 reveals that total composite laminate thickness and stacking sequence of the egg-crate core reference plate and foam-core plate are the same.

Table 6.2. The stacking sequence and thicknesses of the foam-core specimen.

	Upper Face	Lower Face
Stacking Sequence	0/45/-45/90/90/-45/45/0/0/45/-45/90	90/-45/45/0/0/45/-45/90/90/-45/45/0
Thickness	0.15 mm/ply	0.15 mm/ply

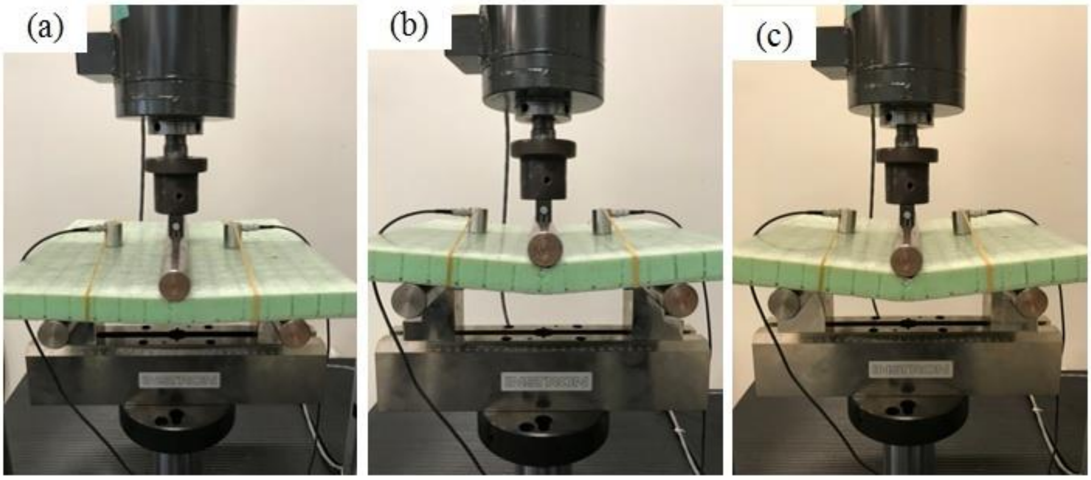

Figure 6.10. The deformed shapes of the foam-core sandwich plate during the three-point bending test corresponding to the top bar displacements and loads (a) 2 mm - 5945 N, (b) 5 mm - 10622 N, and (c) 8 mm - 9502 N.

Figure 6.10 shows deformed shapes of the foam-core sandwich plate at different stages of the three-point bending test. Figure 6.11 shows the load-strain curve for the foam-core sandwich plate as well as absolute energy levels together with peak frequency distribution. The peak load is recorded as 10737 N at 4.80-mm displacement. At 2.90-mm displacement, a high-energy hit is observed and this hit is followed by consistent signals from 20-120 and 260-300 kHz frequency bands. Therefore, the first-ply failure is assumed to occur at this point. The corresponding load level is 8300 N.

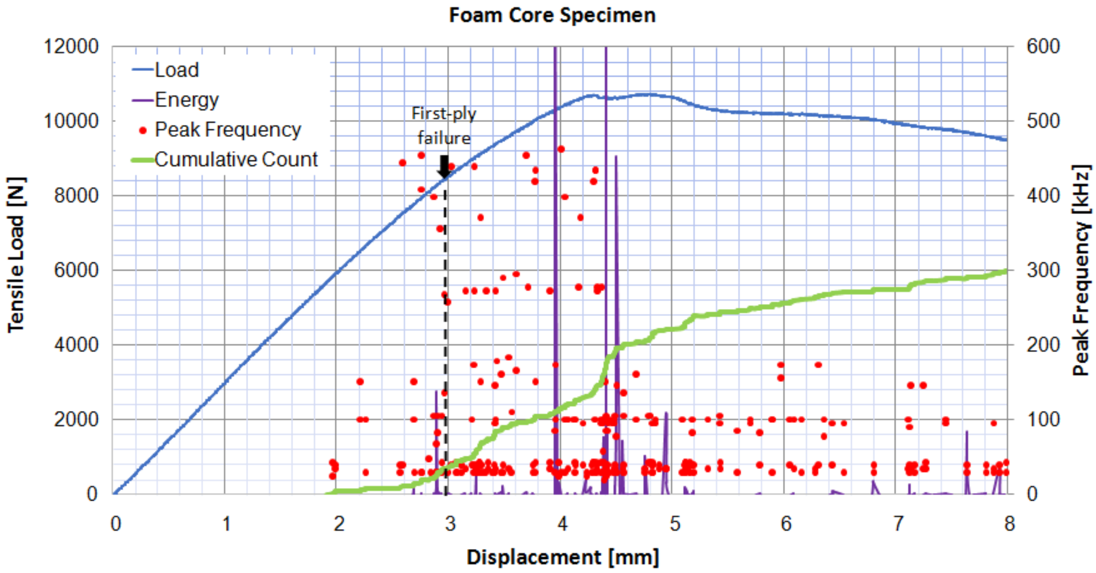

Figure 6.11. Load vs. displacement for the foam-core sandwich plate under three-point bending together with peak frequency distribution of AE hits, energy levels and cumulative counts of the AE hits.

The normalized values of the first-ply failure load and the flexural stiffness of the reference plate, the foam-core sandwich plate, and the optimum plate are calculated and compared. The span length and the plate thickness of these three plates and the volume of the composite material they contain are given in Table 6.3. The flexural stiffness is calculated by dividing the load corresponding to 2-mm displacement to 2.0 mm. Because, the dimensions of the plates and the amount of composite material they contain are different, the strength and stiffness values are not comparable. Normalization provides a way of comparing their strength and stiffness. The stiffness, the first-ply failure load, their normalized values (see Eqs. 5.12 and 5.20), and mass per unit volume of the plate are given in Table 6.4. The mass per unit volume of the plate is calculated by dividing the mass of the composite material that the plate contains to the overall plate volume. The density of the composite material is calculated as 1.65 gr/cm^3. For the foam-core plate, the mass of the foam is neglected. The comparison shows that the strength of the foam-core plate is about 2.16 times the strength of the reference plate. However, the strength of the optimum plate is about 1.71 times and 3.69 times the strength of the foam-core plate and the reference plate, respectively. In addition, the stiffness of the optimum plate is about 1.14 times and 5.86 times the stiffness of the foam-core plate and the reference plate, respectively. It can be concluded that the optimization of the egg-crate shaped core yields significant increase of the overall strength and the stiffness of the plate.

Table 6.3. The span length, the core thickness and the volume of the composite material for the reference plate, the foam-core plate and the optimum plate.

	Span length [mm]	Width [mm]	Thickness [mm]	Volume of the composite material [cm^3]		
				Core	Face	Total
Reference plate	200	300	23.84	91.82	144.02	235.84
Foam-core plate	200	300	23.60	-	216.00	216.00
Optimum plate	169.43	197.66	23.84	75.20	80.38	155.58

Table 6.4. The first-ply failure load, the flexural stiffness, and their normalized values of the reference plate, the foam-core plate and the optimum plate as well as the mass per unit volume of the plate.

	First-ply failure load [N]	Normalized first-ply failure load [N]	Flexural stiffness [N/mm]	Normalized flexural stiffness [N/mm]	Mass per unit volume of the plate[gr/cm^3]
Reference plate (Experimental)	4240	4240	645	645	0.272
Foam-core plate (Experimental)	8300	9155	2975	3315	0.252
Optimum plate (FEM prediction)	14383	15645	4844	3782	0.195

7. CONCLUSION

In this study, the bending strength of a composite sandwich plate is maximized under three-point bending by optimizing its egg-box shaped core. The material is selected as the E-glass-fiber-reinforced epoxy for both core and face sheets in quasi-isotropic $[0/45/-45/90]_s$ layup sequences. Tensile tests are performed on specimens with quasi-isotropic $[0/45/-45/90]_s$, cross-ply $[0/90]_{2s}$, and angle-ply symmetric $[45/-45]_{2s}$ layup sequences. Acoustic emission (AE) monitoring is used to detect the damage events and identify the damage mechanisms. Using the tensile test results and a progressive failure model, the mechanical properties of the plies are determined.

A two-variable shape optimization study is performed using Nelder-Mead method for the core structure to maximize the overall bending strength of the composite sandwich plate. The design variables are selected as contact length and base angle of the unit cells. A finite element model is developed in ABAQUS environment to simulate the behavior of the composite sandwich plate under three-point bending. The first-ply failure load level is determined based on Tsai-Hill failure criterion using the secant algorithm. The model is validated by comparing its predictions with the results obtained by three-point bending tests. The optimum core structure is manufactured by using a 3D-printed polylactid acid (PLA) mold. The face sheets and core structure are manufactured using vacuum infusion process (VIP). The comparison between the test results and the finite element model predictions shows that the finite element model predicts the first-ply failure load level and the failure region with sufficient accuracy. Finally, the optimized design results in about 269% bending strength increase and 486% flexural stiffness increase compared to the reference sandwich plate.

Two specimens with optimum core geometry are manufactured to verify the strength gain under three-point bending. However, split-offs between the core and the face sheets occurred before initial intralaminar failure, because the shear stresses at the interface exceeded the shear strength of the adhesive material. The tests are repeated for the cases in which the faces and the core are bonded by applying J-B® Weld plastic bonder and L285 laminating resin with H285 hardener. However, both bonding materials failed before the composite material is damaged. Nevertheless, the load-displacement response predicted by the finite element model for the optimum core design is compared with the linear portion of the experimentally obtained ones and it is observed that the stiffness prediction of the finite element model correlates well with the test results. In addition, the optimization yields a significant increase in the overall stiffness and strength of the plate. In order to avoid separation between the core and the face sheets, either a better way of bonding these parts should be found or the lower limit on the contact length should be increased; in this way, the area of the bonded region, and thus shear strength, is increased.

REFERENCES

1. Ratwani, Mohan M., “Composite Materials and Sandwich Structures - A Primer”, R-Tec Rolling Hills Estate CA, 2010.

2. Mazumdar, Sanjay., Composites Manufacturing: Materials, Product, and Process Engineering, CrC Press, 2001.

3. Campbell, Flake C., Structural Composite Materials, ASM International, 2010.

4. Williams, Richard R., William E. Howard, and Scott M. Martin., “Composite Sandwich Structures with Rapid Prototyped Cores”, Rapid Prototyping Journal, Vol17, pp. 92-97, 2011.

5. Petras, A., Design of Sandwich Structures, Ph.D. Thesis, Cambridge University, 1998.

6. Li, Tiantian, and Lifeng Wang, “Bending Behavior of Sandwich Composite Structures with Tunable 3D-Printed Core Materials”, Composite Structures, Vol. 175, pp. 46-57, 2017.

7. Carlsson, Leif A., and George A. Kardomateas, Structural and Failure Mechanics of Sandwich Composites, Vol. 121, Springer Science & Business Media, 2011.

8. Correia, J. R., *et al.*, “GFRP Sandwich Panels with PU Foam and PP Honeycomb Cores for Civil Engineering Structural Applications: Effects of Introducing Strengthening Ribs”, International Journal of Structural Integrity, Vol. 3, pp. 127-147, 2012.

9. Composites, Hexcel., *HexWeb*^{TM} *Honeycomb Sandwich Design Technology*, 2000.

10. Standard Test Method For Determining Poisson's Ratio Of Honeycomb Cores, ASTM International.

11. Evans, Anthony G., *et al.*, “The Topological Design of Multifunctional Cellular Metals”, Progress in Material Science, Vol. 46, pp. 309-327, 2001.

12. Ashby, Michael F., *et al.*, Metal Foams: A Design Guide, Elsevier, 2000.

13. Wadley, Haydn N.G., Norman A. Fleck, and Anthony G. Evans, “Fabrication and Structural Performance of Periodic Cellular Metal Sandwich Structures”, Composites Science and Technology, Vol. 63,pp. 2331-2343, 2003.

14. Liu, Jiagui, *et al.*, “Impact Strength Enhancement of Aluminum Tetrahedral Lattice Truss Core Structures”, International Journal of Impact Engineering, Vol. 79, pp. 3-13, 2015.

15. Liu, T., Z. C. Deng, and T. J. Lu, “Design Optimization of Truss-Cored Sandwiches with Homogenization”, International Journal of Solids and Structures, Vol. 43, pp. 7891-7918, 2006.

16. Qiao, Pizhong, *et al.*, “Optimization of Transverse Shear Moduli for Composite Honeycomb Cores”, Composite Structures, Vol. 85, pp. 265-274, 2008.

17. Sun, Guangyong, *et al.*, “A Two-Stage Multi-Fidelity Optimization Procedure for Honeycomb-Type Cellular Materials”, Computational Materials Science, Vol. 49, pp. 500-511, 2010.

18. Poirier, Jeffrey D., Senthil S. Vel, and Vincent Caccese, “Multi-Objective Optimization of Laser-Welded Steel Sandwich Panels for Static Loads Using a Genetic Algorithm”, Engineering Structures, Vol. 49, pp. 508-524, 2013.

19. Xie, Gongnan, *et al.*, “Thermomechanical Optimization of Lightweight Thermal Protection System Under Aerodynamic Heating”, Applied Thermal Engineering, Vol. 59, pp. 425-434, 2013.

20. Deshpande, V. S., and N. A. Fleck, “Energy Absorption of an Egg-box Material”, Journal of the Mechanics and Physics of Solids, Vol. 51, pp. 187-208, 2003.

21. Zupan, Marc, C. Chen, and N. A. Fleck, “The Plastic Collapse and Energy Absorption Capacity of Egg-Box Panels”, International Journal of Mechanical Sciences, Vol. 45, pp. 851-871, 2003.

22. Akisanya, Alfred Rotimi, and N. A. Fleck, “Plastic Collapse of Thin-Walled Frusta and Egg-Box Material Under Shear and Normal Loading”, International Journal of Mechanical Sciences, Vol. 48, pp. 799-808, 2006.

23. Chung, J. G., S. H. Chang, and M. P. F. Sutcliffe, “Deformation and Energy Absorption of Composite Egg-Box Panels”, Composites Science and Technology, Vol. 67, pp. 2342-2349, 2007.

24. Yoo, S. H., S. H. Chang, and M. P. F. Sutcliffe, “Compressive Characteristics of Foam-Filled Composite Egg-Box Sandwich Panels as Energy Absorbing Structures”, Composites Part A: Applied Science and Manufacturing, Vol. 41, pp. 427-434, 2010.

25. Nowpada, Sravanthi, *et al*., “Aluminum "Egg-Box" Panel as an Energy Absorber for Pedestrian Protection”, Advanced Engineering Materials, Vol. 12, pp. 591-595, 2010.

26. Nowpada, Sravanthi, *et al*., “‘Egg-Box’ Panel for Commercial Vehicle Front - Compressive Loading Tests”, International Journal of Crashworthiness, Vol. 15, pp. 59-70, 2010.

27. Haldar, A. K., *et al*., “The Compressive Properties of Sandwich Structures Based on an Egg-Box Core Design”, Composites Part B: Engineering, Vol. 144, pp. 143-152, 2018.

28. Cai, Zhong-Yi, Xi Zhang, and Xiao-Bo Liang, “Multi-Point Forming of Sandwich Panels with Egg-Box-Like Cores and Failure Behaviors in Forming Process: Analytical Models, Numerical and Experimental Investigations”, Materials & Design, Vol. 160, pp. 1029-1041, 2018.

29. Liang, Xiao-Bo, *et al.*, “Plastic Forming of the Doubly Curved Surfaces of Sandwich Plates with Bi-Directionally Trapezoidal Cores of Different Sizes”, Thin-Walled Structures, 2019.

30. Uzal, A., Failure Behavior of Undulated Sandwich Plates Under Out-of-Plane Loading, M.Sc. Thesis, Boğaziçi University, 2014.

31. Reifsnider, K. L., E. G. Henneke, W. W. Stinchcomb, and J. C. Duke, “Damage Mechanics and NDE of Composite Laminates”, Mechanics of Composite Materials: Recent Advances, pp. 399-420, 1983.

32. Aroush, D. Raz-Ben, *et al.*, “A Study of Fracture of Unidirectional Composites Using in itu High-Resolution Synchrotron X-Ray Microtomography”, Composites Science and Technology, Vol. 66, pp. 1348-1353, 2006.

33. Correa, E., *et al*. “Effects of The Presence of Compression in Transverse Cyclic Loading on Fibre-Matrix Debonding in Unidirectional Composite Plies”, Composites Part A: Applied Science and Manufacturing, Vol. 38, pp. 2260-2269, 2007.

34. Gamstedt, E. K., and B. A.Sjögren, “Micromechanisms in Tension-Compression Fatigue of Composite Laminates Containing Transverse Plies”, Composites Science and Technology, Vol. 59, pp. 167-178, 1999.

35. Greenhalgh, Emile, Failure Analysis and Fractography of Polymer Composites, Elsevier, 2009.

36. Kenane, M., and M. L. Benzeggagh, “Mixed-Mode Delamination Fracture Toughness of Unidirectional Glass/Epoxy Composites Under Fatigue Loading”, Composites Science and Technology, Vol. 57, pp. 597-605, 1997.

37. Center for Nondestructive Evaluation Iowa State University, *Modelling Cracks and Delaminations in Carbon Fiber Composites*, http://www3.cnde.iastate.edu/ultrasonics-and-composites/modeling-cracks-and-delaminations-carbon-fiber-composites-frank-margetan, accessed in March 2018.

38. Kyriakides, S., *et al*., "On the Compressive Failure of Fiber Reinforced Composites", International Journal of Solids and Structures, Vol. 32, pp. 689-738, 1995.

39. Feld, Nicolas, *et al*., "Micro-Mechanical Prediction of UD Laminates Behavior Under Combined Compression Up to Failure: Influence of Matrix Degradation", Journal of Composite Materials, Vol. 45, pp.2317-2333, 2011.

40. Jones, R.M., Mechanics of Composite Materials, Second Edition, Taylor & Francis, 1999.

41. Daniel, Isaac M., *et al*., Engineering Mechanics of Composite Materials, Second Edition, New York: Oxford University Press, 2006.

42. Tsai, S. W., D. Gay, and S. V. Hoa, Composite Materials Design and Applications, CrC Press, 2003.

43. Personal Homepage of Prof. Wim Van Paepegem, *Vacuum Infusion - The Equipment and Process of Resin Infusion*, http://www.composites.ugent.be/home_made_composites/documentation/FibreGlast_Vacuum_infusion_process.pdf, accessed in June 2018.

44. Composite Dimensions, *Resin Infusion*, http://www.compositedimensions.com/resin-infusion, accessed in June 2018.

45. Vacmobiles.com™ Limited, *What is Resin Infusion (or Vacuum Infusion)?*, http://www.vacmobiles.com/resin_infusion.html, accessed in June 2018.

46. Performance Composites Inc., *Vacuum Infusion Process (VIP) Guide*, http://www.performancecomposites.com/about-composites-technical-info/125-resin-vacuum-infusion.html, accessed in June 2018.

47. Vitrofiber & Chem S.L., *Technical Datasheet - METYX Composite Reinforcements*, http://www.vitrofiber.com/data/archivo/Q%20625E10C%20-%205200.004.084.pdf, accessed in November 2017.

48. Vitrofiber & Chem S.L., *Technical Datasheet - METYX Composite Reinforcements*, http://www.vitrofiber.com/data/archivo/LT%20300E10B%20-%205200.002.197.pdf, accessed in November 2017.

49. Çalışkan, S., *Mechanical Properties of Non-Crimp Fabric (NCF) Fiberglass Reinforced Composite Materials Manufactured by Using Vacuum Infusion Process*, M.Sc. Thesis, Boğaziçi University, 2009.

50. Hexion® Specialty Chemicals, *Resin MGS® L 285 Hardeners MGS® 285, 286, 287 Technical Information*, 2006, https://m.aircraftspruce.com/catalog/pdf/mgs285tech.pdf, accessed in September 2016.

51. Mistras Products & Systems Division, *PKWDI Sensor*, http://www.physicalacoustics.com/content/literature/sensors/Model_PKWDI.pdf, accessed in October 2017.

52. Öz, F. E., *Characterization of Failure in Composite Materials with Acoustic Emission and Correlation with Micromechanics*, Ph.D. Thesis, Boğaziçi University, 2018.

53. Standard Test Method for Tensile Properties of Polymer Matrix Composite Materials, ASTM International.

54. Standard Test Method for In-Plane Shear Response of Polymer Matrix Composite Materials by Tensile Test of a ±45° Laminate, ASTM International.

55. Arumugam, V., *et al.*, “Effect of Fiber Orientation in Unidirectional Glass Epoxy Laminate Using Acoustic Emission Monitoring”, Acta Metallurgica Sinica (English Letters), Vol. 24, pp. 351-364, 2011.

56. Fotouhi, Mohamad, Parinaz Belalpour Dastjerdi, and Mehdi Ahmadi, “Acoustic Emission Based Method to Characterize Glass/Epoxy Composite Damages During 3-Point Bending Test”, International Journal of Material Science, Vol. 4, pp. 2014, 2014.

57. Uzal, Anil, *et al*. “A Composite Sandwich Plate with a Novel Core Design”, Composite Structures, Vol. 193, pp. 198-211, 2018.

58. Bibo, G. A., P. J. Hogg, and M. Kemp., “Mechanical Characterisation of Glass-and Carbon-Fibre-Reinforced Composites Made with Non-Crimp Fabrics”, Composites Science and Technology, Vol. 57, pp. 1221-1241, 1997.

59. Laustsen, Steffen, *et al*., “Interfibre Failure Characterisation of Unidirectional and Triax Glass Fibre Non-Crimp Fabric Reinforced Epoxy Laminates”, Applied Composite Materials, Vol. 22, pp. 51-79, 2015.

60. Mashayekhi, M., “Element Selection Criteria”, Presentation.

61. Mathews, John H., and Kurtis D. Fink, Numerical Methods Using MATLAB, Upper Saddle River, NJ: Pearson Prentice Hall, 2004.

APPENDIX A: NELDER-MEAD ALGORITHM

Nelder-Mead methodology is followed for the shape optimization of the core structure of the composite sandwich plate. Nelder-Mead method is a simplex method which finds a local minimum of a function of several variables. For two variables, a simplex is a triangle, and the method is a pattern search that compares function values at the three vertices of a triangle. The worst vertex, where $k(x, y)$ is largest, is rejected and replaced with a new vertex. A new triangle is formed and the search continues. The process generates a sequence of triangles for which the function values at the vertices get smaller and smaller. The size of the triangles is reduced and the coordinates of the minimum point are found.

Let $k(x, y)$ be the function that is to be minimized. To start, there are given three vertices of a triangle; $V_k = (x_k, y_k)$, $k = 1, 2, 3$. The subscripts are then reordered so that $z_1 \leq z_2 \leq z_3$. The used notation is:

$$B = (x_1, y_1) \qquad G = (x_2, y_2) \qquad W = (x_3, y_3)$$

where B is the best vertex, G is good (next to best), and W is the worst vertex.

Midpoint of the good side:

The construction process uses the midpoint of the line segment joining B and G. It is found by averaging the coordinates;

$$M = \frac{B + G}{2} = \left(\frac{x_1 + x_2}{2}, \ \frac{y_1 + y_2}{2}\right)$$

Reflection using the point R:

The function decreases as moved along the side of the triangle from W to B, and it decreases as moved along the side from W to G. Therefore, it is feasible that $k(x, y)$ takes on smaller values at points that lie away from W on the opposite side of the line between B

and G. A test point R is chosen which is obtained by reflecting the triangle through the side BG. To determine R, the midpoint M on the side BG is found firstly. Then draw the line segment from W to M and call its length d. This last segment is extended a distance d through M to locate the point R (Figure A.1). The vector formula for R is:

$$R = M + (M - W) = 2M - W$$

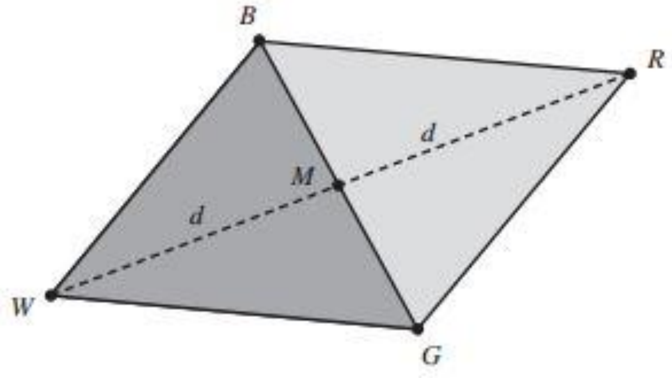

Figure A.1. Triangle $\boldsymbol{BGW}$, mid-points $\boldsymbol{M}$ and reflected point $\boldsymbol{R}$ for the Nelder-Mead method [61].

Expansion using the point E:

If the function value at R is smaller than the function value at W then it is moved in the correct direction toward the minimum. So, the line segment is extended through M and R to the point E. This forms an expanded triangle BGE. The point E is found by moving an additional distance d along the line joining M and R (Figure A.2). If the function value at E is less than the function value at R, then a better vertex than R is found. The vector formula for E is:

$$E = R + (R - M) = 2R - M$$

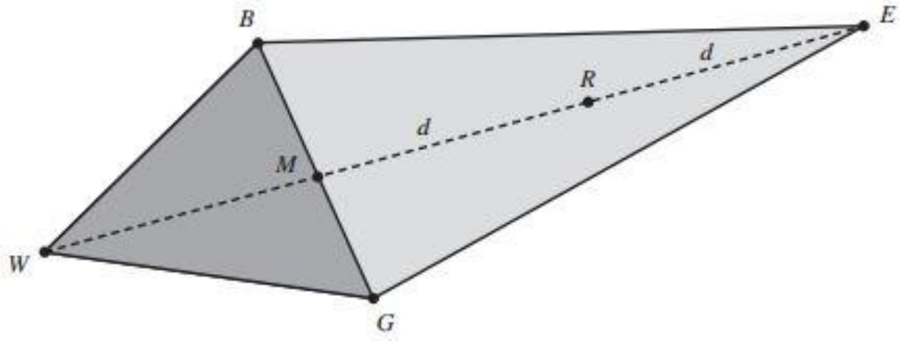

Figure A.2. Triangle $\boldsymbol{BGW}$ and point $\boldsymbol{R}$ and extended point $\boldsymbol{E}$ [61].

Contraction using the point C:

If the function values at R and W are the same, another point must be tested. Perhaps the function is smaller at M, but W cannot be replaced with M because a triangle should be obtained. Consider the two midpoints C_1 and C_2 of the line segments WM and MR, respectively (Figure A.3). The point with the smaller function value is called C, and the new triangle is BGC.

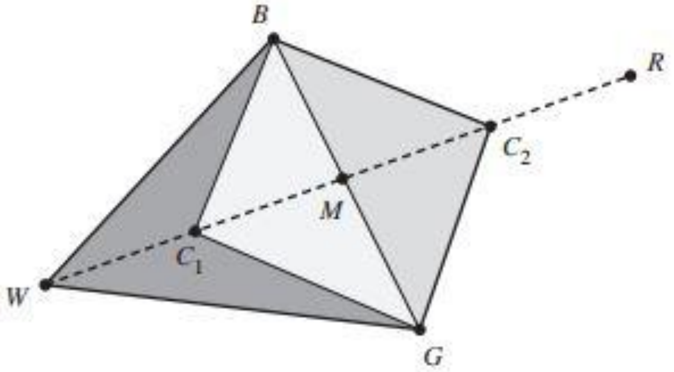

Figure A.3. Contraction point $\boldsymbol{C_1}$ or $\boldsymbol{C_2}$ for the Nelder-Mead method [61].

Shrink toward B:

If the function value at C is not less than the value at W, the points G and W must be shrunk toward B (Figure A.4). The point G is replaced with M, and W is replaced with S, which is the midpoint of the line segment joining B with W.

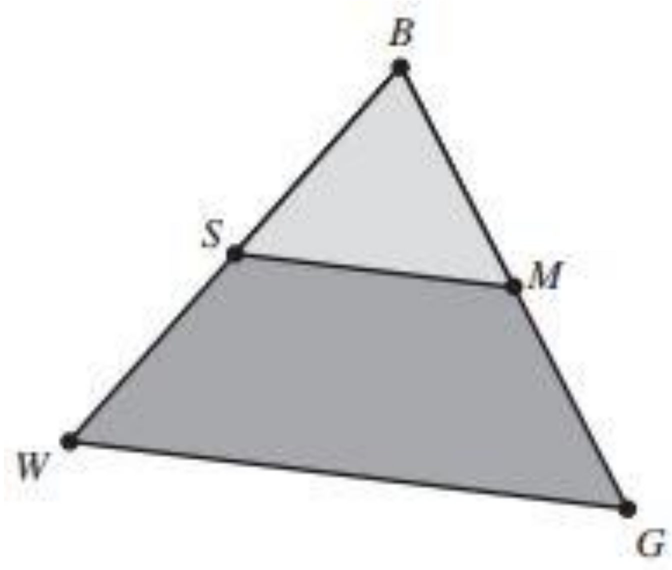

Figure A.4. Shrinking the triangle toward ***B*** [61].

Logical decisions for each step:

A computationally efficient algorithm should perform function evaluations only if needed. In each step, a new vertex is found which replaces W. As soon as it is found, further investigation is not needed, and the iteration step is completed.